MODELING AND MEASUREMENT OF SURFACE PRESSURE FLUCTUATION IN AN IMPINGING JET

By

Nasem A. Aukla

A THESIS

Submitted to
Michigan State University
in partial fulfillment of the requirements
for the degree of

Mechanical Engineering – Master of Science

2018

ABSTRACT

MODELING AND MEASUREMENT OF SURFACE PRESSURE FLUCTUATION IN AN IMPINGING JET

By

Nasem A. Aukla

Impinging jets are used in many engineering and industrial applications, including heating, cooling, drying, food processing, and surface cleaning, among others. The present thesis work is focused on modeling and studying the unsteady wall-pressure signature produced by a jet impinging normally on a flat surface. This study is divided into two main parts:

A theoretical part, to establish the *beginning step* towards building a physics-based, mathematical model to calculate the surface-pressure fluctuation on the impingement surface. The mathematical model is used to explore the effects of changing the flow and jet-vortices parameters, one at a time, on the characteristics of the surface-pressure fluctuation. Three main parameters are examined: vortex-passage frequency, jet Reynolds number, and vortex circulation.

An experimental part, to measure the unsteady surface pressure fluctuation on the impingement surface for an axisymmetric jet at normal incidence. Measurements are done, for Reynold numbers $Re_D = 8272$ and 24818 (based on the jet diameter (D) and jet exit velocity), using a microphone array extending radially from the stagnation point ($r/D = 0$) into the wall-jet zone ($r/D = 2.33$).

Comparison of the model and the experimental results shows that, despite of the model simplicity, certain qualitative features of the unsteady wall pressure are similar within the stagnation zone. This outcome establishes confidence to continue further development of the model in the future.

DEDICATED TO THE MEMORY OF MY FATHER AND MOTHER

ACKNOWLEDGMENTS

I would like to sincerely acknowledge my family, advisor, committee members, friends, and colleagues, because without their help and support this work could not have been done. Many people have helped me to come at this point, and I cannot go further before expressing my most profound gratitude to them.

Firstly, to Prof. Dr. Ahmed Naguib for giving me an opportunity to be one of his students and to work on an exciting and challenging topic. His advice, direction, and encouragement were much supportive of my thesis.

My profound gratitude to my committee members Prof. Dr. Farhad Jaberi and Prof. Dr. Ricardo Mejia-Alvarezwhose for being on my committee.

Many thanks to Dr. Ke Zhang who helped me with my experimental setup.

My profound gratitude to Dr. Sami Al-Araji, Mr. Dhia Al-Ashaqr, and Mr. Nazar Hussain who helped me to achieve my goal, without their support I would not have accomplished this work.

Finally, Many thanks to my colleague and best friend, Fady Hindo. The honest and purest gentleman who I met in my entire life. Thank you for your true friendship.

TABLE OF CONTENTS

LIST OF TABLES

LIST OF FIGURES

KEY TO SYMBOLS

A, B	Hot-wire calibration coefficients (King's law)
a	Constant in the potential stagnation-point flow equations
C	Volumetric constant related to the volume of the vortex ring
c	Sound speed
C_p	Mean-pressure coefficient
C_{prms}	Root-mean-square-pressure coefficient
D	Jet diameter
E	Hot-wire output voltage (King's law)
E_c	Temperature-corrected hot-wire output voltage
$E(k)$	Complete elliptic integral of the second kind
E_m	Measured hot-wire voltage
E_{ij}	Strain-rate tensor
f	Frequency
H	Distance between the impingement plate and the jet exit
$K(k)$	Complete elliptic integral of the first kind
l	Side length of the plane wave tube
N	Number of samples in a time series
P	Mean wall pressure
P_d	Dynamic pressure of the jet ($P_d = {}^1\!/_2\, \rho U_j^2$)
PSD	Power spectral density of the wall-pressure fluctuation
p	Wall pressure

p'	Wall-pressure fluctuation
p_{rms}	Root mean square of the wall pressure fluctuation
q	Flow source of pressure
Re_D	Jet Reynolds number based on the jet diameter and the jet exit velocity
R_c	Vortex core radius
R_{co}	Initial vortex core radius
r, θ	Impingement-plate polar coordinates
St_D	Strouhal number based on jet diameter
T_{cal}	Temperature of the flow during hot-wire calibration
T_m	Temperature of the flow during hot-wire measurements
T_w	Hot-wire temperature
u_{ri}	Radial component of velocity induced by the image on the real vortex ring
${u^*}_{ri}$	Dimensionless radial component of velocity induced by the image on the real vortex ring
u_{zi}	Normal component of velocity induced by the image on the real vortex ring
${u^*}_{zi}$	Dimensionless normal component of velocity induced by the image on the real vortex Ring
u_{rs}	Radial component of self-induced velocity
u_{zs}	Normal component of self-induced velocity
u^*_{zs}	Dimensionless normal component of self-induced velocity
U_j	Jet exit velocity
U_r	Radial velocity component (parallel to the plate)
U_y	Axial velocity component (normal to the plate)
U_θ	Azimuthal velocity component

R_o, Y_o	Initial coordinates of the vortex ring's core center in polar coordinates
$x_{o,}\ y_o$	Initial coordinates of the vortex ring's core center in Cartesian coordinate
x, y, z	Cartesian coordinate system with origin at the center of the impingement plate
x', y', z'	Cartesian coordinates of the pressure source
t	Time
ϕ	Velocity potential
γ_{ij}	Rotation rate tensor
Γ	Vortex Circulation
Γ_{sl}	Circulation around a contour that encompasses the shear layer
ω	Vorticity
λ	Wavelength
Θ	Momentum thickness of the jet shear layer
ρ	Fluid density
μ	Fluid dynamic viscosity
ν	Fluid kinematic viscosity
ΔU	Velocity difference across the shear layer
Ψ	Stream function
ψ^*	Dimensionless stream function

CHAPTER 1: Introduction

Experimental, computational and analytical research has been used to study impinging jets for the past decades because of their significance to many applications, including cooling, heating, drying, air conditioning, and ventilation. The present research is concerned with modeling, and understanding the physics of wall-pressure generation in impinging jets. This knowledge is significant for applications involving flow-induced noise and vibration. To motivate the current research, a summary of relevant previous literature is necessary. However, some understanding of the basic characteristics and flow features of free (non-impinging) jets is essential. Therefore, the present discussion starts with an overview of the latter. This is followed by a brief summary of the relevant work on impinging jets and their wall-pressure characteristics. Finally, the motivation and the specific objectives of this thesis are outlined at the end of the chapter.

1.1 Free Jets

1.1.1 Background

Jets can be classified into different categories according to: the nozzle exit shape (e.g. circular, square, triangular, lobed, etc.), the nozzle contour (e.g. smooth versus sharp-edged), the pipe length from which the jet emerges (long or short; if any), and the initial discharge condition (free, wall and surface jet). The most basic type of jets is the axisymmetric free jet, driven by pressure to emerge at the end of a contoured nozzle into a quiescent ambient. For a free jet, after exiting the nozzle, a free shear layer with uniform pressure surrounds the jet. As the flow develops farther downstream, mixing of the jet fluid with the ambient causes an increase in the mass flow rate in the jet stream (i.e. via flow entrainment), and, in conjunction with viscous and turbulence effects, leads to jet spreading and decreasing of the flow speed to conserve momentum.

Depending on the characteristics of the jet's centerline velocity decay, the jet development may be divided into three zones as depicted in Figure 1.1. see Shih-I Pai [1]

- Zone 1: in this zone, there is a potential core in the central part of the jet and a mixing zone is sandwiched between the potential core and the surrounding medium. The potential core has a centerline velocity equal to the jet exit velocity. This zone extends up to 4 – 6 jet diameters;
- Zone 2: represents the transition where the velocity profile gradually changes until self-similarity is established. This zone extends from the end of zone 1 to 20 jet diameters;
- Zone 3: represents the self-similarity zone where the transverse mean velocity profile is similar at different axial distances when normalized using the local centerline velocity and jet width.

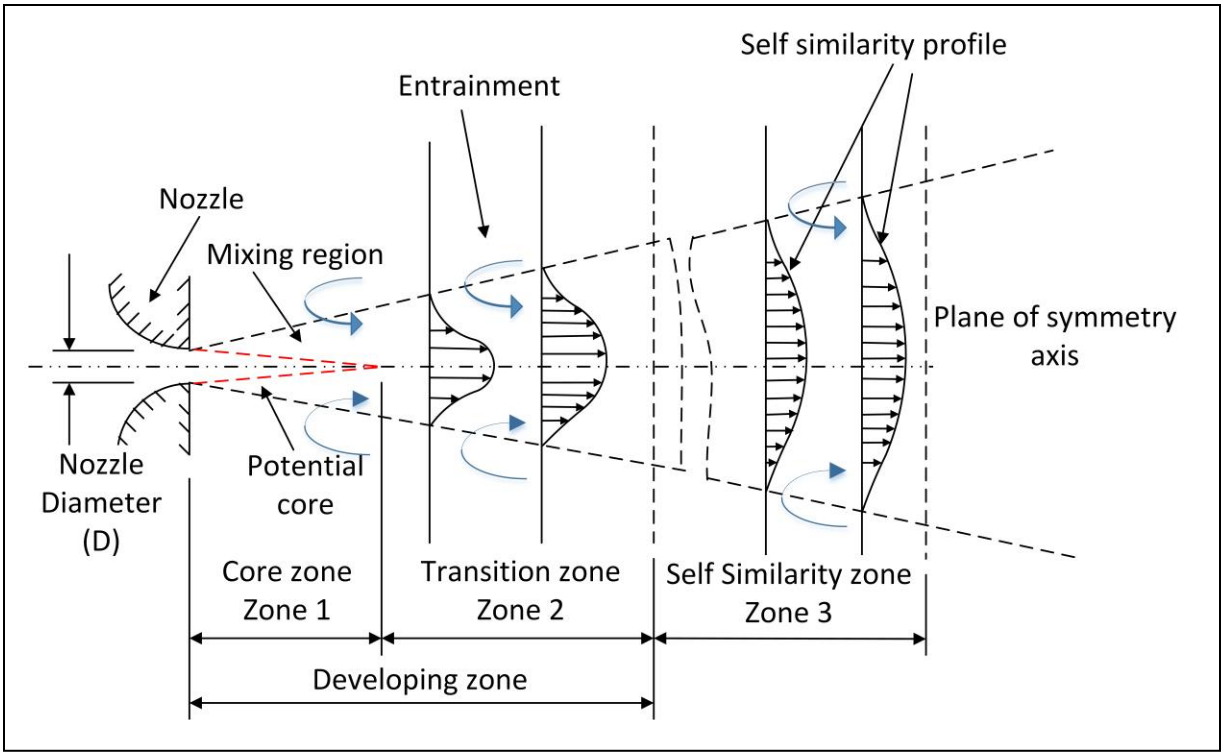

Figure 1.1 Schematic of a free-jet flow, depicting various flow development zones

1.1.2 Literature Review

The primary and fundamental interest in studying free jets has been focused on the instability of the shear layer downstream from the nozzle exit, and the turbulence development farther downstream. Grant [2] theoretically studied the shear layer instability in axisymmetric jets. This study shows the formation of vortex structures from an instability wave originating at the beginning of the jet's laminar axisymmetric shear layer. The initially weak instability wave amplifies with downstream distance, ultimately leading to creation of the eddies.

Popiel and Trass [3] visualized free and impinging round jets using a smoke wire. For the free jet, they showed the vortices to form in the potential-core region within the free shear layer. The downstream merging of these vortices causes the creation of larger eddies. These vortices increase mixing and enhance the entrainment rate. Also, the axial symmetry of the near field of the nozzle exit is found to be created by the generation of the toroidal vortices, because they cause a significant upstream interaction. Zaman and Hussain [4] studied the natural large-scale structures in the axisymmetric mixing layer surrounding the jet. They found the flow from the jet exit to the end of the potential core to be controlled by two characteristic length scales: the jet diameter and the initial shear layer thickness. Near the jet exit, the momentum thickness controls the flow structure. Initially, the momentum thickness is thin, and as the shear-layer rolls-up into vortical structures, the momentum thickness grows. The vortices resulting from the roll-up start to interact and create larger eddies. After a distance x, which is comparable to the jet diameter, the diameter length scale controls the flow structure. As the jet Reynolds number ($Re_D = U_j D/\nu$; where U_j is the jet exit velocity, D the jet diameter, and ν the fluid kinematic viscosity) increases, the ratio of the shear layer thickness at the nozzle lip to the diameter of the jet decreases, which leads to a smaller initial instability wavelength, relative to the jet diameter, and larger number of vortex pairings before the vortices size becomes comparable to the jet diameter, at the end of the potential core.

1.2 Impinging Jet

1.2.1 Background

In an impinging jet, the flow is incident on a, typically, flat wall at a distance H from the jet exit. Though the angle of incidence of the jet relative to the wall-normal direction may change, the present work is only concerned with normal incidence; i.e. where the jet symmetry axis is perpendicular to the wall. The flow field for an impinging jet may be divided into three zones (see Figure 1.2):

- Free- jet zone: which represents the domain stretching from the nozzle exit to the point where the existence of the plate does not influence the flow. Within this zone, the jet flow and associated flow features are as discussed in the previous section;
- Stagnation zone: which represents the domain where the mean flow direction changes from being normal to being parallel to the plate. This zone, which extends up to $r/D = 1$ in the radial direction, has the maximum mean pressure of the flow (at the stagnation point on the wall);
- Wall-jet zone: which corresponds to the domain $r/D > 1$. Unsteady separation of the boundary layer is known to occur in this region due to the interaction of the jet vortices with the wall; See Didden and Ho [5] and Landreth and Adrian [6].

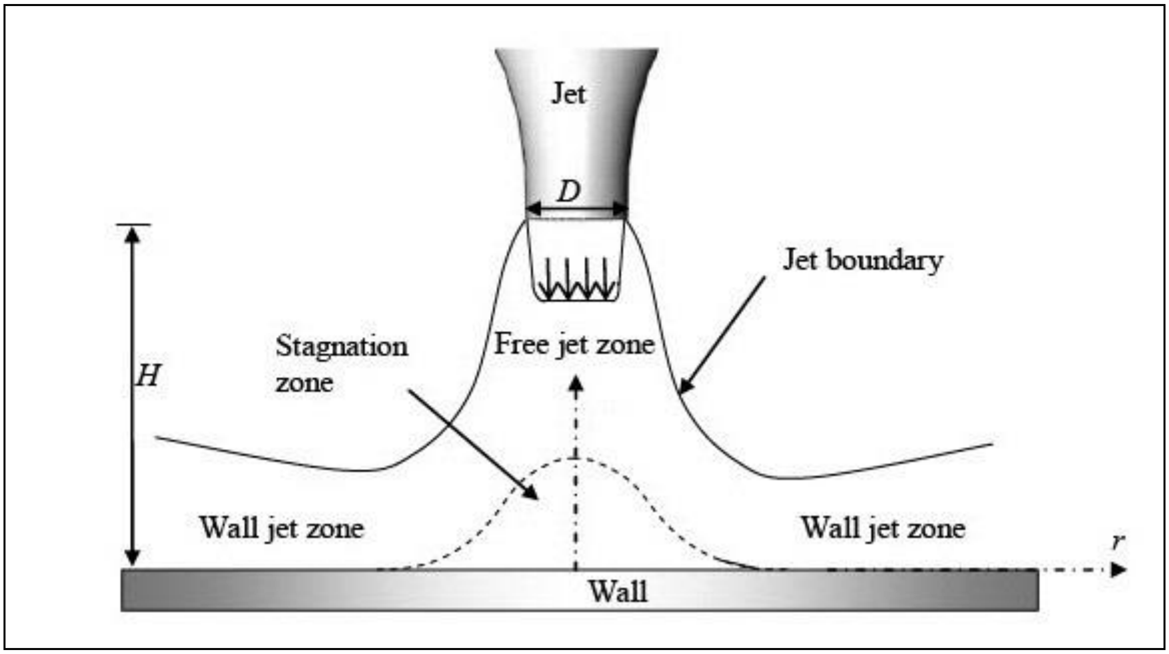

Figure 1.2 Schematic of the impinging jet at normal incidence (taken from Al-Aweni [7])

1.2.2 Literature Review

A brief review is provided here of the current knowledge on wall-pressure fluctuation in impinging jets. Similar to the current work, focus will be on *H/D* values extending to the end of the potential core ($H/D \approx 4$). To characterize the strength of the pressure fluctuation, typically the radial distribution of the root mean square of the fluctuation (p_{rms}) is examined. The recent work of Krishna [8] provides the most comprehensive p_{rms} data, covering the Reynolds number range $Re_D = 20{,}000 - 50{,}000$, and $H/D = 1 - 8$. Krishna showed that for $H/D \leq 3$, the largest pressure fluctuation are found in the wall-jet zone in the range $r/D = 1.3 - 1.5$ for all Reynolds numbers. A second peak within the stagnation zone emerged, near $r/D \approx 0.5$, when Re_D reached 25,000 and the impingement wall was sufficiently far from the jet ($H/D \geq 4$). When present, this secondary peak magnitude was higher than that in the wall-jet zone.

Consistent with the work of Krishna [8], several earlier studies have identified the wall-jet-zone peak of the pressure fluctuation. These include the work of Hall and Ewing [9] and [10], who found the peak at $r/D = 1.5$ for $Re_D = 23300\ and\ 50000$, and $H/D = 2\ and\ 4$, El-Anwar *et al.* [11], at $r/D = 1.7$ for $Re_D = 16500$ and $H/D = 4$, and Al-Aweni [7], $r/D \approx 1.33$ for $Re_D = 7334$ and $H/D \leq 4$. The variation in the exact location of the peak between the different studies might be due to Reynolds number, the jet initial condition, or the radial spacing between the measurements. The *RMS* level of the pressure fluctuation associated with this peak is quite large, reaching around 20% of the jet's dynamic pressure (based on jet exit velocity), but this level, along with the overall level of pressure fluctuation in the wall-jet zone, decrease with increasing both Re_D and H/D. This Reynolds number trend is seen in the data of Krishna [8], while the H/D dependence is reported in all aforementioned studies.

The p_{rms} peak in the stagnation zone is most clearly seen in the data of Krishna [8], which extend into a high-enough Re_D range for the peak to be observed. The presence of this peak is also implied in the data of Hall and Ewing [9,10] at $Re_D = 23000$, although there were not sufficient measurement points to ascertain the specific location of the peak inside the stagnation zone. Furthermore, Hall and Ewing employed a jet that exits at the end of a fully-developed turbulent pipe flow, which exhibits significant pressure fluctuations at the stagnation point (relative to jets exiting from a contoured nozzle) due to the absence of a potential core.

Within the stagnation zone, p_{rms} increases with increasing H/D; opposite to the trend in the wall-jet region. This behavior is generally associated in the literature with the growing influence of the vortical structures on the stagnation zone as the vortices grow to a size comparable to the jet diameter through successive pairings (e.g. see Al-Aweni [7]). On the other hand, the

Reynolds number influence is found to decrease the stagnation-zone pressure fluctuation (Krishna [8]). No specific explanation for this trend is known at this point.

Frequency spectra analysis of the wall-pressure time series measured in the studies referenced above show that the frequencies of the spectral peaks are consistent with the passage frequency of the jet vortices. In addition to depending on the initial conditions and Reynolds number of the jet, the latter frequency is predominantly affected by the distance between the jet exit and the impingement plate. As the distance increases from *H/D*=2 to the end of the potential core, the number of vortex ring parings ahead of impingement increases, decreasing the passage frequency of the vortices. Al-Aweni [7] used simultaneous time-resolved flow visualization and wall-pressure measurement, employing a microphone array, for a jet Reynolds number of 7970, and *H/D*=2,3, and 4. He showed that for *H/D*=2, the first vortex merging occurred within the wall-jet zone, as the vortices traveled parallel to the impingement wall. For $H/D = 3$, the first pairing was completed before reaching the impingement plate, while for *H/D=4*, the second merging took place ahead of the plate. When pairing happened ahead of reaching the wall, each merging resulted in halving the fundamental frequency in the pressure spectra. When merging happened while the vortices traveled past, and interacted with the wall ($H/D = 2$), the spectrum contained the original vortex formation frequency (or Strouhal number $St_D \approx 1.3$) and its sub-harmonic ($St_D \approx 0.64$). The lowest frequency observed, at $H/D = 4$ after two pairings, corresponded to $St_D \approx 0.32$. The drop of the dominant pressure-fluctuation Strouhal number with H/D and the overall order of magnitude of the Strouhal number values reported in Al-Aweni [7] is consistent with the findings of Hall and Ewing [9] and [10], El-Anwar *et al.* [11] and Krishna [8].

The earliest explanation for the large pressure fluctuation associated with the p_{rms} peak in the wall-jet zone came from the work of Didden and Ho [5]. These authors studied a normally impinging axisymmetric forced air jet at Reynolds number of 19000, and *H/D*=4. Using phase averaged pressure and hot-wire measurements, they showed that the high level of pressure fluctuation in the wall-jet region is associated with the unsteady boundary layer separation, and subsequent formation of an opposite-signed *secondary* vortex, when a jet (primary) vortex interacted with the wall. Such an unsteady boundary-layer separation process, and associated phenomena, was first noted by Harvey and Perry [12] in relation to trailing wing-tip vortices interacting with the ground. In impinging jets, formation of secondary vortices was also reported in the work of Landreth and Adrian [6], for Reynolds number of 6500 using particle image velocimetry, and the flow visualization of Popiel and Trass [3]. Didden and Ho [5] showed that the boundary layer separation was associated with the adverse pressure gradient imposed by the jet vortices on the boundary layer.

Naguib and Koochesfahani [13] used whole-field velocity data of an isolated axi-symmetric vortex ring interacting with a flat wall to understand the fundamental surface-pressure generation mechanism associated with vortex-wall interaction. They employed Green's function solution of Poisson's equation for pressure (see section 1.2.3) to calculate the wall-pressure generating sources and wall-pressure signature from the velocity-field data. In addition to connecting negative wall-pressure peaks with the primary and secondary vortices, they were able to identify an important source of positive pressure fluctuation, not known before then. Specifically, they showed that the high strain zone associated with the separation of the boundary layer (induced by the main vortex ring) was an important source of positive pressure fluctuation. The results, however, did not show a strong negative pressure peak, as was found in the work of Didden and Ho [10] beneath the separated zone. This may have been due to the limited spatial resolution of the experimental data within the separating boundary layer.

Al-Aweni [7] conducted a comprehensive study of the wall-pressure fluctuation and associated generation mechanisms in impinging jets. The work utilized both experimental data (from simultaneous time-resolved flow visualization and wall-pressure sensor-array data) and axi-symmetric laminar *CFD* calculation of isolated vortices interacting with a flat wall. An interesting and new finding from this study is that pressure fluctuation where the wall-jet p_{rms} peak is observed are especially strong when vortex-wall interaction happens while two vortices are in the process of pairing. He showed that during such pairing, which happened at $H/D = 2$, the resulting secondary vortex is much stronger than when a single vortex interacts with the wall. In particular, he saw that, occasionally, vortices may pass without pairing, in which case, the pressure spikes were not as strong. The switch between pairing/no-pairing seemed to happen randomly in time. The *near-wall pairing* produced strong negative pressure spikes that reached a magnitude comparable with the dynamic pressure, based on the jet exit velocity. Al-Aweni also found that the positive-pressure source identified earlier by Naguib and Koochesfahani [13], which is associated with the high strain rate within the separating boundary layer, has a significant influence on the shape and evolution of the strong negative spikes.

1.2.3 Governing Equations

To get better understanding of the physical mechanisms leading to wall-pressure fluctuation, it is insightful to connect the pressure fluctuation generation to the vortical structures. This may be done using Poisson's equation for the pressure (p) in incompressible turbulent flow:

$$-\frac{1}{\rho}\frac{\partial^2 p}{\partial x_i \partial x_i} = \frac{\partial u_i}{\partial x_j}\frac{\partial u_j}{\partial x_i} \tag{1.1}$$

Where, $\frac{\partial u_i}{\partial x_j}$ is the velocity gradient tensor and Einstein's tensor notation is used. The forcing term in equation (1.1) (right-hand side) can be divided into two parts: symmetric (in terms of the strain rate e_{ij}), and antisymmetric (in terms of the rotation tensor γ_{ij}); see Bradshaw and Koh [14]:

$$-\frac{1}{\rho}\frac{\partial^2 p}{\partial x_i \partial x_i} = e_{ij}e_{ij} - \gamma_{ij}\gamma_{ij} \tag{1.2}$$

Where,

$$e_{ij} = \frac{1}{2}\left(\frac{\partial u_i}{\partial x_j} + \frac{\partial u_j}{\partial x_i}\right) \tag{1.3}$$

$$\gamma_{ij} = \frac{1}{2}\left(\frac{\partial u_i}{\partial x_j} - \frac{\partial u_j}{\partial x_i}\right) \tag{1.4}$$

It is known that the rotation tensor is connected to the vorticity vector through:

$$\gamma_{ij}\gamma_{ij} = \frac{1}{2}(\omega_i\omega_i) \tag{1.5}$$

Thus, equation (1.2) can be written as

$$-\frac{1}{\rho}\frac{\partial^2 p}{\partial x_i \partial x_i} = e_{ij}e_{ji} - \frac{1}{2}(\omega_i\omega_i) \tag{1.6}$$

From equation (1.6), the pressure source strength (q) is given by:

$$q = e_{ij}e_{ji} - \frac{1}{2}(\omega_i\omega_i) \tag{1.7}$$

Equation (1.6) may be written in vector form as follows,

$$\frac{1}{\rho}\nabla^2 p(x, y, z, t) = -q(x, y, z, t) \tag{1.8}$$

Green's function can be used to solve equation (1.8) (e.g. Blake [15]) to get the pressure on a solid wall beneath an unsteady flow, where the wall-normal coordinate $y = 0$, for pressure source distribution $q(x', y', z')$ within the flow. More specifically,

$$p(x, y = 0, z) = \frac{\rho}{2\pi} \int \left[\frac{e_{ij} e_{ji}(\acute{x}, \acute{y}, \acute{z}) - \frac{1}{2}(\omega_i \omega_i)(\acute{x}, \acute{y}, \acute{z})}{\sqrt{(x - \acute{x})^2 + (\acute{y})^2 + (z - \acute{z})^2}} \right] d\acute{V} - \frac{1}{2\pi} \int \left[\frac{\mu \left[\frac{\partial^2 v}{\partial y^2}(x', z') \right]}{\sqrt{(x - \acute{x})^2 + (z - \acute{z})^2}} \right] d\acute{S} \tag{1.9}$$

The volume integral (first term) in equation (1.9) represents the contribution to the wall pressure by the flow structure within the body of the flow, while the surface integral is computed over the wall beneath the flow. For a flat wall, the second term is negligible (from boundary layer approximation perspective). The volume integrand shows that there are two wall-pressure generation mechanisms: one related to strain rate, and the other to vorticity. The former results in the generation of positive, and the latter in negative wall pressure. Thus, flow features where rotation dominates strain effects (e.g. in the core of vortices), generate negative pressure, while those associated with dominant strain (e.g. the zone in between interacting vortices) results in positive pressure generation; e.g. see Naguib and Koochesfahani [13]. Another important feature of the volume integrand in equation (1.9) is that the source term effect is inversely proportional to the distance between the point of wall-pressure observation and the pressure source location (as seen from the numerator of the integrand). Thus, as this distance increases, the observed wall pressure decreases. Therefore, the pressure observed at a point on the wall is a *global* quantity, related to all features within the flow with the net pressure being the result of the integrated effect of the strength and proximity of the different sources.

1.3 Motivation

The motivation for this research is to understand the physics of, and to predict the unsteady surface pressure generation in impinging jets due to their significance in flow-induced noise and vibration. As described earlier in this chapter, the basic connection between the dominant flow features in impinging jets and wall-pressure generation is fairly well understood. However, there is practically no effort that capitalizes on this understanding to develop physics-based (also known as structure-based) models to compute the wall pressure in impinging jets. Such models, if sufficiently accurate, could be valuable as engineering design tools for flow-induced noise and vibration applications, since the models are much more efficient to run than direct numerical simulations, and they are more robust than non-physics based turbulence models.

Additionally, physics-based models could be used to understand the underlying flow physics from a point of view that is not possible with experiments or numerical simulations. Specifically, in real flows, or their simulations, it is difficult to vary certain flow or structure parameters one at a time because of the interdependence of these parameters. With a mathematical model, such variations are possible, which could lead to a clearer understanding of the effect of individual parameters on quantities of interest; the wall-pressure fluctuation in the present work. An example of such model-based insights may be found in the work of Monnier *et al.* [16], where a Gaussian-core vortex array was used to model the wake of a harmonically pitching airfoil. The model helped to understand the connection between the parameters describing the wake-vortex configuration (vortex streamwise and cross-stream spacing, vortex circulation, and core radius) and the mean thrust acting on the airfoil.

1.4 Objectives

The objectives of this study may be summarized as follows:

1- Developing a *simple* mathematical model, which represents the *first step* towards a high-fidelity model, for predicting wall-pressure fluctuations in normally impinging jet flows. The model will be used to explore the effect of vortex passing frequency, vortex circulation, and Reynold number on the unsteady wall-pressure characteristics, while varying one parameter at a time. In addition, the model results, which are only applicable to the stagnation zone due to inherent simplicity/limitations of the model, will be compared to experimental data obtained in the present study.

2- To conduct measurements of the unsteady surface pressure in a normally impinging jet using a microphone array. The measurements are done for two Reynolds numbers: $Re_D =$ 8272 and 24818 for *H/D* values of 2, 3 and 4 (reaching to the end of the potential core). The measurements will be used to examine the influence of the Reynolds number on the characteristics of the wall pressure flucution (primarily the radial distribution of the root mean square pressure fluctuation, the probability density function of the pressure fluctuation and the power spectral density). The lower Reynolds number is selected to match this of the earlier study by Al-Aweni [7] in the same jet facility. Al-Aweni utilized time-resolved flow visualization and microphone-array measurements to connect the flow features to the wall-pressure characteristics. Thus, combining Al-Aweni's findings with those from the present work, it is possible to *infer* the effect of Reynolds number on the sources of wall-pressure generation.

The remainder of the thesis is organized to show the mathematical model details in Chapter 2, the mathematical model results in Chapter 3, the experimental apparatus and procedure in Chapter 4, the experiment results and their comparison with the model results in Chapter 5, and conclusions and recommendations for future work in Chapter 6.

CHAPTER 2: Mathematical Model

2.1. Modeling Background

Prior to describing the features of the physics-based model developed here, a recap of the flow details that should be captured by a good model is described. Near the jet exit, vortices are generated due to the instability of the shear layer and its subsequent roll-up into axisymmetric vortex rings. As the vortex rings travel downstream, the vortex size and strength increases by merging. Several such mergings may occur, with the number of successive pairings depending on Reynolds number and distance between the nozzle and the impingement plate. When the Reynolds number decreases, the coherence of the flow structure increases, and the number of successful pairings increases. Nearing impingement, within the stagnation zone, the flow changes its direction to be parallel to the plate. Further downstream as the flow advects through the wall-jet zone, boundary layer separation leads to secondary vortex formation and maximum wall-pressure fluctuation. Based on the literature review of Chapter 1, surface pressure fluctuation in impinging jets is caused by both inviscid phenomena (direct influence of vortices in stagnation and wall-jet zones) and viscous phenomena (vortex-wall and vortex-vortex-wall interaction in the wall-jet zone).

The above description highlights that a complex model is needed to capture the impinging jet flow features and associated wall-pressure fluctuation. More specifically, elements of a high-fidelity model should consist of

- A viscous vortex ring model;
- Ability to model vortex pairing;
- Advection velocity field consistent with the actual mean jet velocity field;

- An impingement-plate boundary layer model;
- A vortex-boundary layer interaction model;
- Poisson's equation solution to compute the wall-pressure from the velocity field.

However, developing such high-fidelity model is an ambitious goal that requires several stages of development. This work focuses on the starting step by considering only the simplest possible model. Table (2.1) shows a comparison of the features of a high-fidelity and the present model.

Feature	**High-Fidelity Model**	**Current Model**
Vortex ring model	Viscous-core vortex model	Potential vortex model
Vortex-vortex interaction	• Mutual induction • Pairing model	Not modeled
Advection field	Based on impinging-jet mean flow; e.g., from CFD or experiment	Potential stagnation-point flow
Impingement-plate boundary layer	Modeled	Not modeled
Vortex-boundary layer interaction	Modeled	Not modeled
Wall-pressure calculation	Poisson's equation solution	Unsteady Bernoulli's equation

Table 2.1 Comparison of high-fidelity and present model features

Table (2.1) demonstrates that the present model is very simple and ignores all viscous and vortex-vortex interactions effects. However, evidence suggests that within the stagnation-zone wall-pressure fluctuations are primarily generated via potential flow mechanisms for $H/D < \sim 4$. Therefore, the present model may be successful in at least reproducing the same qualitative features of stagnation-zone wall-pressure fluctuations. One of the main goals of this work is to assess the ability of the present simple model to do so.

2.2 Model Details

2.2.1. Vortex Rings

The full *inviscid* mathematical model for the impingement-jet problem is depicted schematically in figure (2.1). A cylindrical coordinate (r, θ, z) system is used to describe the problem mathematically. However, because of symmetry, the model equations have no dependence on (θ). Each of the jet vortices is modeled employing a potential vortex ring that has an axis of symmetry perpendicular to the impingement wall. Each ring has circulation (Γ), radius (R), zero core radius (R_c), and vertical core coordinate (Z). In the absence of the wall, the ring is in free space and translates downwards (for the sense of circulation depicted in figure 2.1) due to self-induction effects. The stream function for the ring is given by Helmholtz equation [17]

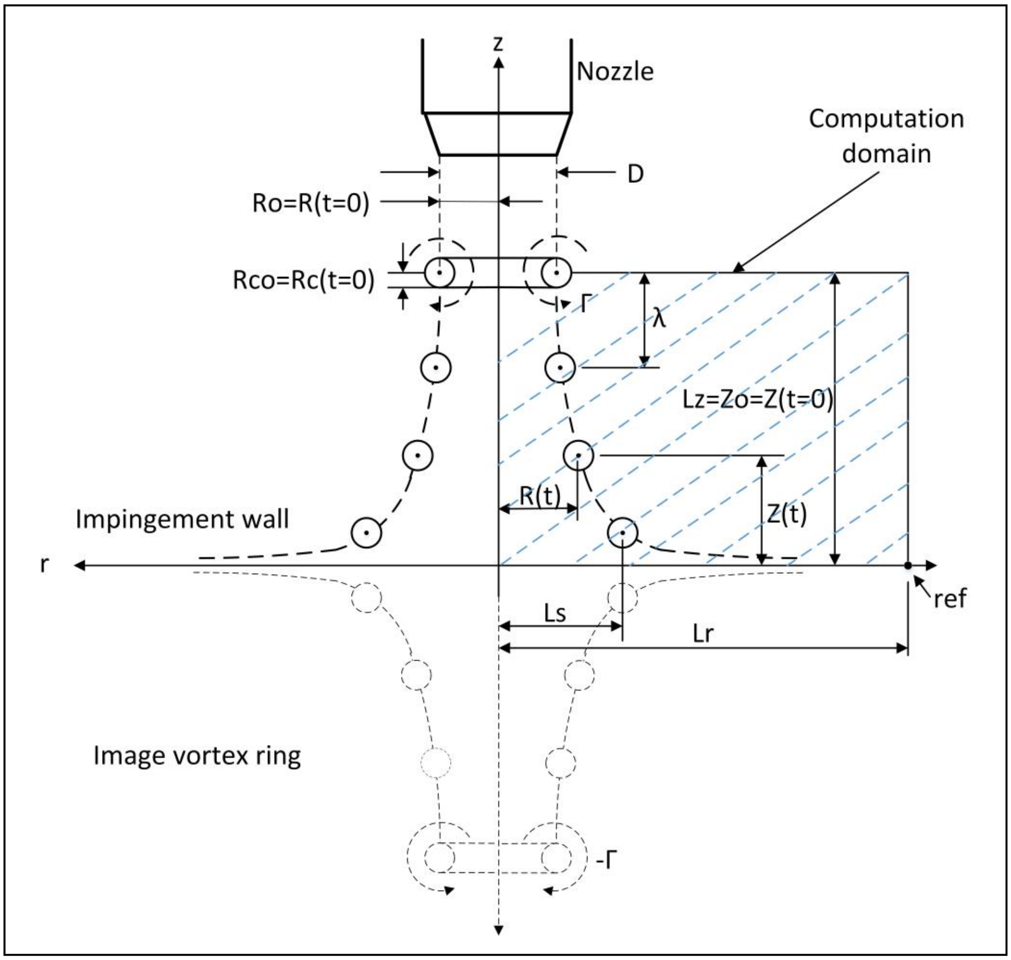

Figure 2.1 Schematic drawing of the full mathematical model of the impinging jet

$$\psi(r,z,t) = \Gamma\left[\frac{(Rr)^{1/2}}{2\pi k}\{(2-k^2)K(k) - 2E(k)\}\right] \tag{2.1}$$

where

$$k^2 = \frac{4Rr}{(z-Z)^2 + (r+R)^2} \tag{2.2}$$

$K(k)$ represents complete elliptic integral of the first kind, and $E(k)$ represents complete elliptic integral of the second kind:

$$K(k) = \int_0^{\pi/2} \sqrt{\frac{1}{(1 - k^2 \sin^2 x)}}\, dx \tag{2.3}$$

$$E(k) = \int_0^{\pi/2} \sqrt{(1 - k^2 \sin^2 x)}\, dx \tag{2.4}$$

To make equation 2.1 dimensionless, the initial vortex-ring radius R_o is used as a length scale. Since in jet flow, the jet vortices have a radius approximately equal to the jet opening radius, this length scale is equivalent to half the jet diameter, *D*/2. The velocity scale is taken as the velocity of the advection field (potential stagnation flow, at the top of the computational domain, $z = Z_o = 5R_o$), which is given by $10aR_o$ (see section 2.2.3). This velocity scale corresponds to the mean "exit jet velocity". The dimensionless form of the equation (2.1) is:

$$\psi^*(r, z, t) = \left[\frac{(R^* r^*)^{1/2}}{2\pi k}\left\{(2 - k^2)K(\bar{k}) - 2E(k)\right\}\right] \tag{2.5}$$

The above equations are for zero-core radius potential vortex ring. The infinitesimal core leads to an infinite induced velocity at the core, which makes it impossible to track the vortex movement. To overcome this problem, a finite, but small, vortex core radius is assumed ($R_c \ll R$). Following the work of Walker *et al*. [18], the velocity distribution inside the core is assumed to be uniform. This leads to the following self-induced velocity of the ring:

$$u_{zs} = -\frac{\Gamma}{4\pi R}\left[log\left(\frac{8R}{R_c}\right) - \frac{1}{4}\right] \tag{2.6}$$

2.2.2. Wall (Vortex Rings Images)

The equations discussed in section 2.2.1 are valid for a vortex in free space. These equations need to be modified for the presence of the impingement wall; i.e., by enforcing a zero wall-normal velocity, or no-penetration, condition at the wall. This is done by adding to the model an image vortex, relative to the wall ($z = 0$) with equal but opposite circulation ($-\Gamma$) to the real vortex (see figure 2.1). this velocity induced by the image on the real vortex ring has radial and wall-normal components ($u_{ri}\, and\, u_{zi}$). Thus, as the real vortex ring approaches the wall, the image vortex ring will affect the real ring in two ways: by stretching the ring radially outwards and reducing the approach velocity of the ring toward the wall. The radial stretching of the ring causes the ring radius to increase. According to Helmholtz, for inviscid incompressible flow, the vortex lines move with the fluid particles, and the vortex ring must have constant volume, i.e.

$$R(t) * R_c^2(t) = C \tag{2.7}$$

Where C is constant. Thus, in the presence of the wall, R increases and R_c decreases with time. Both of these quantities affect the self-induced velocity (see equation 2.6). The resulting self-induced velocity components ($u_{rs}\, and\, u_{zs}$), using equations (2.6 and 2.7) respectively are:

$$u_{rs} = 0 \tag{2.8}$$

$$\begin{aligned} u_{zs} &= -\frac{\Gamma}{8\pi R}\left[log\left(\frac{64R^3}{C}\right) - \frac{1}{2}\right] \\ u_{zs}^* &= -\frac{1}{8\pi R^*}\left[log\left(\frac{64(R^*)^3}{C^*}\right) - \frac{1}{4}\right] \end{aligned} \tag{2.9}$$

The stream function for the image vortex is given by

$$\begin{aligned} \psi(r,z,t) &= -\Gamma\left[\left[\frac{(Rr)^{1/2}}{2\pi\bar{k}}\left\{(2-\bar{k}^2)K(\bar{k}) - 2E(\bar{k})\right\}\right]\right] \\ \psi^*(r,z,t) &= -\left[\frac{(R^*r^*)^{1/2}}{2\pi\bar{k}}\left\{(2-\bar{k}^2)K(\bar{k}) - 2E(\bar{k})\right\}\right] \end{aligned} \tag{2.10}$$

where

$$\bar{k}^2 = \frac{4Rr}{(z+Z)^2 + (r+R)^2} \tag{2.11}$$

And as before, $K(\bar{k})$ and $E(\bar{k})$ represent the complete elliptic integrals of the first and the second kind respectively.

The velocity induced by the image on the real vortex is obtained from the stream function due to the image by applying equations (2.12 and 2.13) and setting $(r = R)$ and $(z = Z)$; i.e., the coordinates of the real vortex core.

$$u_r = \frac{1}{r}\frac{\partial\Psi}{\partial z}$$

$$u_r^* = \frac{1}{r^*}\left(\frac{\partial\Psi}{\partial z}\right)^* \tag{2.12}$$

$$u_z = -\frac{1}{r}\frac{\partial\Psi}{\partial r}$$

$$u_z^* = -\frac{1}{r^*}\left(\frac{\partial\Psi}{\partial r}\right)^* \tag{2.13}$$

This leads to the velocity components produced by the image vortex ring on the real vortex (see Walker *et al*. [18]):

$$u_{ri} = \frac{\Gamma\bar{k}}{4\pi Z}\left[\left[2\left\{\frac{E(\bar{k}) - [\{1-\bar{k}^2\}\{K(\bar{k})\}]}{\bar{k}^2}\right\}\right] - E(\bar{k})\right]$$

$$u^*{}_{ri} = \frac{\bar{k}}{4\pi Z^*}\left[\left[2\left\{\frac{E(\bar{k}) - [\{1-\bar{k}^2\}\{K(\bar{k})\}]}{\bar{k}^2}\right\}\right] - E(\bar{k})\right] \tag{2.14}$$

$$u_{zi} = \frac{\Gamma\bar{k}^3}{4\pi R}\left[\frac{K(\bar{k}) - E(\bar{k})}{\bar{k}^2}\right] \tag{2.15}$$

$$u^*{}_{zi} = \frac{\bar{k}^3}{4\pi R^*}\left[\frac{K(\bar{k}) - E(\bar{k})}{\bar{k}^2}\right]$$

2.2.3. Advection Field (Stagnation Point Potential Flow)

The next phase of the model involves adding steady flow to represent advection of the vortex rings by the jet mean flow. To this end, potential point-stagnation flow is selected. The stream function of the flow is given by [19] as

$$\psi = azr^2$$
$$\psi = a^* z^* r^{*2} \tag{2.16}$$

Applying equations (2.12 and 2.13) to (2.16) leads to (see Naguib *et al* [20]):

$$u_{ra} = ar$$
$$u^*_{ra} = a^* r^* \tag{2.17}$$
$$u_{za} = -2az$$
$$u^*_{za} = -2a^* z^* \tag{2.18}$$

where (a) is a constant with dimension $[Time^{-1}]$.

Equation 2.17 shows that the mean flow radial velocity increases linearly and unboundedly with r. In reality, this kind of variation is expected to hold only near the stagnation point with deviation from the model increasing with the radial distance. Therefore, we anticipate that this crude, yet very simple, model to be reasonable only within the stagnation zone.

2.2.4. Vortex Advection and Flow-Field Evolution in Time

For a single vortex convecting through the $Lr - wide \times Lz - high$ computational domain shown in figure 2.1, the velocity field at any time instance consists of three components due to:

1. the real vortex;

2. the image vortex;

3. the stagnation flow.

The stream function of the system is the sum of the three corresponding stream functions; specifically

$$\psi(r,z,t) = \Gamma\left[\left[\frac{(Rr)^{1/2}}{2\pi k}\{(2-k^2)K(k)-2E(k)\}\right]\right.$$
$$\left.-\left[\frac{(Rr)^{1/2}}{2\pi\bar{k}}\{(2-\bar{k}^2)K(\bar{k})-2E(\bar{k})\}\right]\right]+azr^2$$
$$\psi^*(r,z,t) = \left[\frac{(R^*r^*)^{1/2}}{2\pi k}\{(2-k^2)K(k)-2E(k)\}\right]$$
$$-\left[\frac{(R^*r^*)^{1/2}}{2\pi\bar{k}}\{(2-\bar{k}^2)K(\bar{k})-2E(\bar{k})\}\right]+a^*z^*{r^*}^2 \tag{2.19}$$

The velocity components of the resulting flow ($u_r\ and\ u_z$) are found using equations (2.12 and 2.13)

$$u_r = \frac{\Gamma}{2\pi}\sum_{i=1}^{N}\frac{R_i}{(rR_i)^{3/2}}\left[-\frac{\{r^2+{R_i}^2+(z-Z_i)^2\}*(z-Z_i)*M_i*E(k)_i}{(r-R_i)^2+(z-Z_i)^2}\right.$$
$$+\frac{\{r^2+{R_i}^2+(z+Z_i)^2\}*(z+Z_i)*\overline{M_i}*E(\bar{k})_i}{(r-R_i)^2+(z+Z_i)^2}+M_i*(z-Z_i) \tag{2.20}$$
$$\left.*K(k)_i-\bar{M}_i*(z+Z_i)*K(\bar{k})_i\right]+ar$$

$$u^*{}_r = \frac{1}{2\pi}\sum_{i=1}^{N}\frac{R^*}{(r^*R_i{}^*)^{3/2}}\left[-\frac{\left\{r^{*2}+R_i{}^{*2}+(z^*-Z_i{}^*)^2\right\}*(z^*-Z_i{}^*)*M_i*E(k)_i}{(r^*-R_i{}^*)^2+(z^*-Z_i{}^*)^2}\right.$$

$$+\frac{\left\{r^{*2}+R_i{}^{*2}+(z^*+Z_i{}^*)^2\right\}*(z^*+Z_i{}^*)*\overline{M_\iota}*E\left(\bar{k}\right)_i}{(r-R_i)^2+(z+Z_i)^2}+M_i$$

$$\left.*(z^*-Z_i{}^*)*K(k)_i-\overline{M_\iota}*(z^*+Z_i{}^*)*K\left(\bar{k}\right)_i\right]+a^*r^*$$

$$u_z = \frac{\Gamma}{2\pi}\sum_{i=1}^{N}\frac{1}{\sqrt{rR_i}}\left[\frac{M_i*\{r^2-(R_i+z-Z_i)(R_i-z+Z_i)\}*E(k)_i}{(r-R_i)^2+(z-Z_i)^2}-M_i*K(k)_i\right.$$

$$+\frac{\overline{M}_i*\left\{-(r^2-R_i{}^2+z^2+2zZ_i+Z_i{}^2\right\}*E\left(\bar{k}\right)}{(r-R_i)^2+(z-Z_i)^2}$$

$$\left.+\{(r-R_i)^2+(z-Z_i)^2\}*K(\bar{k})_i\right]-2az$$

$$u^*{}_z = \frac{1}{2\pi}\sum_{i=1}^{N}\frac{1}{\sqrt{r^*R_i{}^*}}\left[\frac{M_i*\left\{r^{*2}-(R_i{}^*+z^*-Z_i{}^*)(R_i{}^*-z^*+Z_i{}^*)\right\}*E(k)_i}{(r^*-R_i{}^*)^2+(z^*-Z_i{}^*)^2}-M_i\right.$$

$$*K(k)_i+\frac{\overline{M_\iota}*\left\{-(r^{*2}-R_i{}^{*2}+z^{*2}+2z^*Z_i{}^*+Z_i{}^{*2}\right\}*E\left(\bar{k}\right)_i}{(r^*-R^*)^2+(z^*-Z^*)^2}$$

$$\left.+\{(r^*-R_i{}^*)^2+(z^*-Z_i{}^*)^2\}*K(\bar{k})_i\right]-2a^*z^* \tag{2.21}$$

where

$$M = \sqrt{\frac{rR}{(r+R)^2+(z-Z)^2}} \tag{2.22}$$

$$\bar{M} = \sqrt{\frac{rR}{(r+R)^2 + (z+Z)^2}} \tag{2.23}$$

The summation in (2.20) and (2.21) is over the number of vortices N present in the domain at any given time instant. At the start of the computation, a vortex ring is placed at the top of the domain at $R(0) = R_o \; and \; Z(0) = Z_o$. as time progresses, the ring core coordinates $R \; and \; Z$ change with time according to

$$\frac{dR}{dt} = u_{ri} + u_{ra} \quad (r = R, z = Z)$$

$$\frac{dR}{dt} = \frac{\Gamma\bar{k}}{4\pi Z}\left[\left[2\left\{\frac{E(\bar{k}) - [\{1-\bar{k}^2\}\{K(\bar{k})\}]}{\bar{k}^2}\right\}\right] - E(\bar{k})\right] + aR$$

$$\frac{dR^*}{dt} = \frac{\bar{k}}{4\pi Z^*}\left[\left[2\left\{\frac{E(\bar{k}) - [\{1-\bar{k}^2\}\{K(\bar{k})\}]}{\bar{k}^2}\right\}\right] - E(\bar{k})\right] + aR^* \tag{2.24}$$

$$\frac{dZ}{dt} = u_{zi} + u_{zs} + u_{za} \; (r = R, z = Z)$$

$$\frac{dZ}{dt} = \frac{\bar{\Gamma}k^3}{4\pi R}\left[\frac{K(\bar{k}) - E(\bar{k})}{\bar{k}^2}\right] - \frac{1}{8\pi R}\left[log\left(\frac{64(R)^3}{C}\right) - \frac{1}{4}\right] - 2aZ \tag{2.25}$$

$$\frac{dZ^*}{dt} = \frac{\bar{k}^3}{4\pi R^*}\left[\frac{K(\bar{k}) - E(\bar{k})}{\bar{k}^2}\right] - \frac{1}{8\pi R^*}\left[log\left(\frac{64(R^*)^3}{C^*}\right) - \frac{1}{4}\right] - 2aZ^*$$

To model the periodic formation of vortices in a jet, as the leading vortex moves toward the impingement plate, subsequent vortices are added at the top of the domain at a selected frequency. All vortices approach the wall, gradually changing their dominant travel to be radially outwards. The computation is continued until the first vortex passes the end of the domain (i.e., $R = Lr$).

2.2.5. Wall-Pressure Calculation and Evolution in Time

The unsteady pressure on the impingement plate is found using unsteady Bernoulli's equation.

$$\frac{d\phi}{dt} + \frac{u^2}{2} + \frac{p}{\rho} + gz = F(t) \tag{2.26}$$

Where, ϕ is the velocity potential, g is gravity acceleration, and $F(t)$ is a function of time. Evaluating the LHS on the wall and $F(t)$ at a suitable reference point, and ignoring gravity effect, equation (2.26) becomes

$$\frac{d\phi_w}{dt} + \frac{{u_w}^2}{2} + \frac{p_w}{\rho} = (\frac{d\phi}{dt} + \frac{u^2}{2} + \frac{p}{\rho})_{ref} \tag{2.27}$$

Or

$$\frac{p_w - p_{ref}}{\rho} = \frac{d}{dt}\left(\phi_{ref} - \phi_w\right) + (\frac{u_{ref}^2 - u_w^2}{2}) \tag{2.28}$$

Equation (2.28) shows that to obtain the wall pressure at a given point at any instant in time requires:

1- Knowledge of the radial velocity component at the wall u_w. This information is readily available from the velocity field equations (2.20) and (2.21);

2- Selection of a reference point where: the velocity magnitude u_{ref} is known and the pressure p_{ref} is fixed so it can be used as a reference pressure. The first of these conditions is easily satisfied using equations (2.20) and (2.21). The second condition is more difficult to satisfy and, as will be seen below, meeting this condition sets a lower limit on the radial computational domain size Lr and an upper limit on the computational time.

3- Calculation of the time rate of change of the velocity potential difference between the point of interest and the reference point. At every time instant, the velocity potential can be computed by integrating the velocity field. This leads to two potential issues. First, the integration yields the potential with an unknown additive integration function of time. This issue is not problematic since the time function is subtracted out when computing the potential *difference*. Second, though the velocity field is known analytically, its form is not easy to integrate. Therefore, integration is done numerically to get the potential difference at each time instant. The resulting fields are subsequently differentiated numerically in time to arrive at the first term on the *RHS* of equation (2.28). Further details follow.

As depicted in figure (2.1), the reference point is selected on the wall at the end of the computational domain $r_{ref} = L_r$. This point remains unaffected by the vortex rings until the first vortex ring convects through the entire domain, reaching near $r = L_r$. Thus, the pressure p_{ref} is steady up to the point of arrival of the first vortex ring, at which point the computation is stopped. This imposes a limit on the computational time, leading to a tradeoff process. Given the periodic influence of the vortices, the computation must be run until at least two vortices pass by a given point on the wall in order to obtain a full period of pressure fluctuations. Thus, L_r must be large enough for the computation time to be larger than the lowest period of vortex passage of interest. On the other hand, L_r cannot be made arbitrarily large since the radial domain must be discretized finely for the integration leading to the calculation of the velocity potential difference, which could lead to a prohibitively long integration time. Therefore, L_r is set only as large as necessary by allowing enough running time for the core of at least the second vortex injected into the domain to reach the largest radial location of interest. As discussed previously, it is expected that the applicability of the present model is limited to the stagnation zone. Accordingly, the extent of the radial domain of interest L_s (see figure 2.1) is $L_s/D = 1$, where $D = 2R_o$ is the equivalent of the jet diameter. The unsteady potential function difference $\frac{d(\phi_{ref}-\phi_w)}{dt}$, is calculated using:

$$u_w(r) = u_{rw}(r) = \frac{d\phi_w(r)}{dr} \tag{2.29}$$

which leads to

$$\phi_{ref} - \phi_w(r) = \int_{ref}^{r} u_{rw}(\alpha)d\alpha, \tag{2.30}$$

Where, α is a dummy variable for integration along the radial coordinate. The integral (2.30) is evaluated numerically, where the integrand is obtained by setting $z = 0$ in equation (2.20). Notably, since it is the time derivative of (2.30) that is required for evaluating the wall pressure, the stagnation flow component, which is steady, does not affect the unsteady potential difference term.

2.3. Numerical Details

The model was implemented numerically using Matlab. The implementation consisted of two main tasks. The first one involved periodically seeding vortices at the entrance of the domain and tracking the core centers of these vortices as they advect through the computational domain. Knowledge of the core centers locations at each time instant enabled computation of the instantaneous stream function and velocity field. This information is used to visualize the flow field concurrently with the wall pressure. The second task employed the distribution of the radial velocity component at the wall to compute the distribution of the wall-pressure at each time instant. The specifics of the numerical implementation of these two tasks are given in the two following sub-sections.

2.3.1. Computation of the Time-Dependent Stream Function and Velocity Field

Given the initial core coordinates (R_o, Z_o) of a vortex at the top of the computational domain, subsequent locations of the core (R, Z) at each time step was determined by solving equations (2.24 and 2.25) using fourth-order Runge-Kutta method for the two variables $R(t)$ and $Z(t)$. Once (R, Z) was determined, the stream function was calculated by evaluating equation (2.19) on 100 × 100-point grid using symbolic math tools in Matlab. The solution was independent of the time step and grid resolution, as demonstrated in Section 2.4.

2.3.2. Calculation of the Wall Pressure

As given by the unsteady Bernoulli's equation (2.28), the calculation of the wall pressure at any radial location relative to the pressure at the reference point requires knowledge of the radial velocity at the same radial location and at the reference point, as well as the rate of change of the velocity potential difference between the pressure observation and the reference point. The velocity information was straightforward to obtain. Specifically, once the vortex core locations were determined at every time instant in the first task, the radial velocity distribution on the wall could be determined by setting $z = 0$ in the analytical equation (2.20). The reference velocity u_{ref} was further determined by setting $r = r_{ref}$ in the resulting equation. The radial velocity distribution, and subsequently the wall pressure, was evaluated at 600 points on the wall spanning from the axis of symmetry of the domain to the reference point. This number of points was sufficiently large for the calculated wall pressure to be independent of the number of grid points (see Section 2.4 for details).

On the other hand, to find the unsteady term $\left(\frac{d(\phi_{ref}(r)-\phi_w)}{dt}\right)$ on the wall in Bernoulli's equation (2.28), $\phi_{ref}(r) - \phi_w$ was determined by numerically computing the integral (2.30).

Specifically, the integral was discretized on the 600-point wall grid using the method of rectangles, leading to:

$$\int_{\phi_{ref}}^{\phi(r)} d\phi = \int_{r_{ref}}^{r} u_r \, dr$$
$$\phi(r_{ref} - i\,\Delta r) - \phi_{ref} = -\Delta r \sum_{i=1}^{n-1} u_{ri} \tag{2.31}$$

Where *i* is an index of the wall grid points starting from the point next to the reference point and increasing towards the axis of symmetry, *n* is the number of grid points (600), and Δr is the radial resolution of the grid. The negative sign on the right-hand side reflects the fact that the integration is in the direction of decreasing *r* coordinate.

To evaluate the summation in (2.31), the radial velocity u_{ri} was evaluated by substituting for $z = 0$ and $r = r_i$ in equation (2.20). This enabled evaluation of $\phi_{ref}(r) - \phi_w$ using (2.31) for all time instants. Subsequently, the time derivative of the potential difference was computed using forward finite differencing. The solution was independent of the time step and grid resolution, as demonstrated in Section 2.4.

2.4 Validation of the Computational Approach

Validation tests were done to ensure that the model results are independent of:

- Radial computational domain size;
- Wall-pressure resolution (number of points on the wall to calculate the pressure);
- Time step.

In addition, the outcomes of these validation tests, in terms of the domain size, radial wall-grid resolution and time step, were employed to numerically compute the unsteady surface pressure associated with a line vortex advecting parallel to a flat wall. This was done since: (1) the advecting line vortex problem has certain similarities with the current vortex-rings problem; and

(2) the wall-pressure is known analytically for the line vortex problem, enabling further verification of the numerical solution approach and implementation.

2.4.1 Impinging-Jet Model

2.4.1.1 Validation of the Computational Domain Size

As described in Section 2.2, the main influence of the radial domain size is related to the basic assumption that the pressure at the reference point, which is placed at the radial end of the domain, remains steady throughout the computation. Thus, a larger domain allows longer computation time since it takes the first vortex injected into the domain longer to reach the end and affect the pressure at the reference point. To ensure that the selected domain size is appropriate, three different computational domains having a radial extent of 10, 15, and 20 cm are compared. These values correspond to approximately 20, 30 and 40 times the initial vortex radius. For each of these domains, the wall pressure is computed and the resulting radial distribution at a time instant when the negative "pressure spike" produced by the vortex passage is located at r = 5 cm is considered (Figure 2.2). The selected location $r = 5\ cm$ is 10 times the initial vortex radius; well beyond what would be considered the stagnation zone of the jet (r = one jet diameter ≈ twice the initial vortex ring radius), which is the main focus of the present work. The three pressure distributions from the different domains are compared in pairs at the selected time instant using a Normalized Root Mean Square error (*NRMSE*), defined as follows:

$$NRMSE = \frac{\sqrt{\frac{\sum_{i=1}^{n}(p_{\mathrm{domain\ 1,i}} - p_{domain\ 2,i})^2}{n}}}{|p_{min}|} \tag{2.32}$$

where subscripts domain 1 and domain 2 denote the two domains under comparison, $|p_{min}|$ is the magnitude of the negative pressure spike (minimum pressure) produced by the vortex, and the summation is over all wall grid points; n = 600. Other than the domain radial extent, other model parameters are the same as used for the results presented in Chapter 3. It is noteworthy that the computational time for the three different cases varied from about 10 to 45 minutes for the smallest and the largest domains respectively for the reference case which is define in table 3.1.

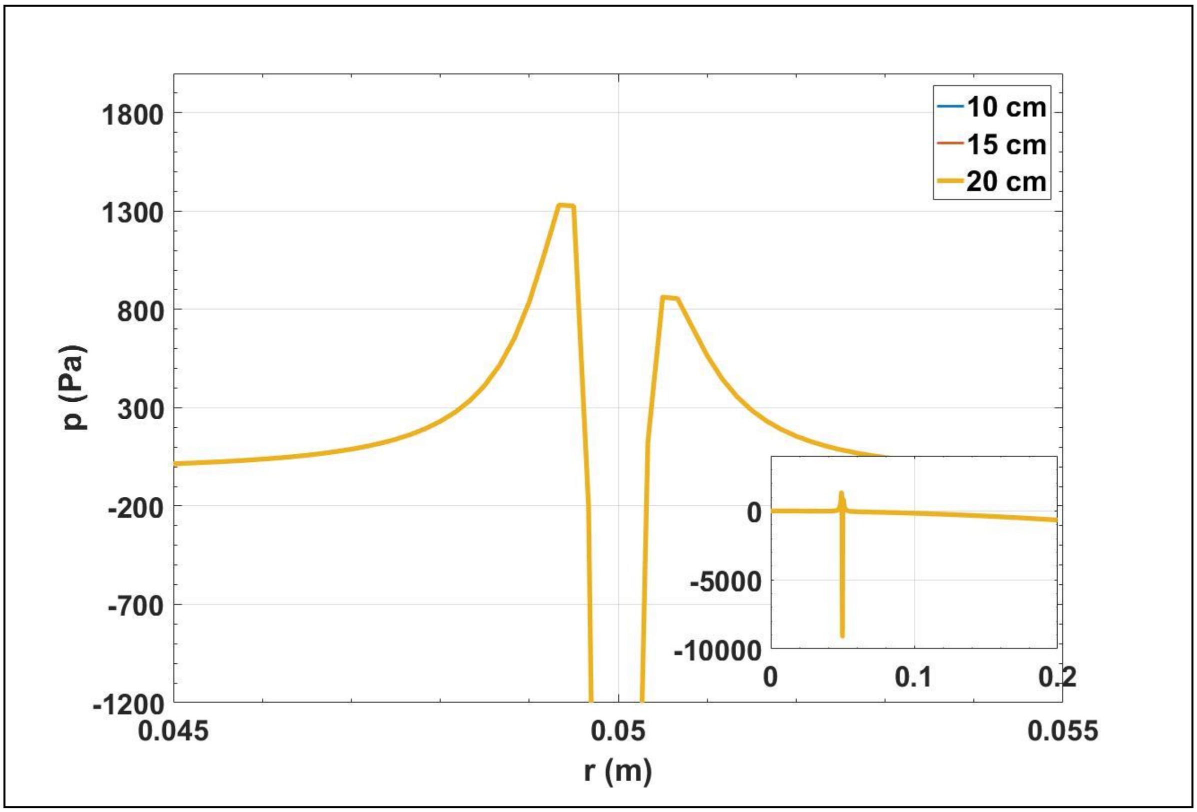

Figure 2.2 Radial wall-pressure distribution at the time instant when the negative pressure spike (minimum pressure) associated with vortex passing is located at $r=5$ cm location. Different color lines represent different radial domain sizes used for computing the wall pressure (as given by the legend). The inset shows the overall distribution, while the main plot depicts a magnified view to show the change between the different cases.

Figure 2.3 depicts the *NRMSE* % as a function of time up to the time corresponding to Figure 2.2. The maximum pressure magnitude $|p_{min}|$ at each time step is used in calculating *NRMSE*. As seen from the figure, the effect of increasing the domain size beyond 10 cm is practically zero (well below 0.1%). Therefore, a 10-cm wide domain was utilized for all the computations conducted here.

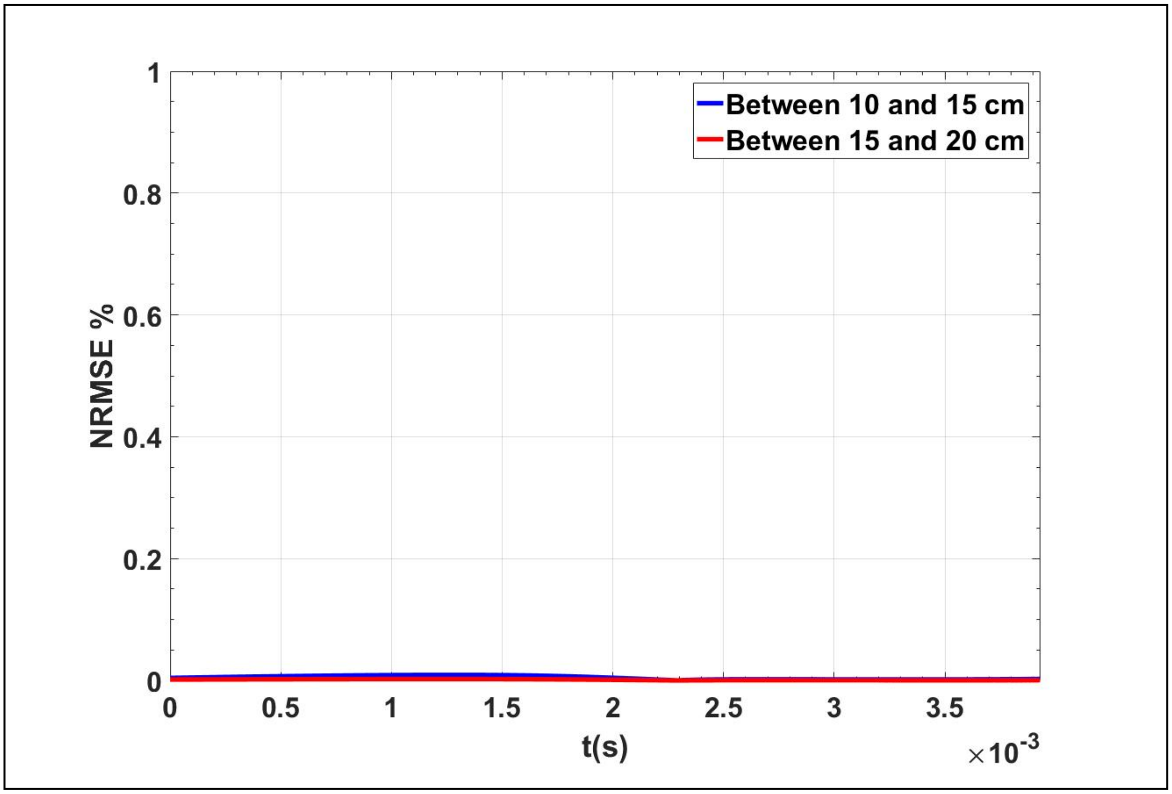

Figure 2.3 Normalized Root Mean Square Error (*NRMSE*) resulting from comparing the results of domain sizes 10 and 15 cm (blue) and 15 and 20 cm (red). The results are shown up to the computation time corresponding to the time instant where the negative pressure spike appears at r = 5 cm.

2.4.1.2 Validation of the Wall-Pressure-Grid Resolution

This step targets the validation of the resolution of the wall grid used to find the wall-pressure fluctuations. The higher the resolution, the better the accuracy. However, increasing the resolution is expensive, consuming more computer resources and time. To validate the selected wall resolution, three wall resolutions were examined for a radial domain extent of 10 cm: 0.33*mm* (300 points on the wall), 0.16*mm* (600 points on the wall), and 0.0833*mm* (1200 points on the wall). These resolutions correspond to approximately 0.07, 0.034 and 0.017 of the initial vortex ring radius R_o. All other model parameters are as described in Chapter 3. It is noteworthy that the computational time for the three different cases varied from about 10 to 40 minutes for the resolution 0.33mm and 0.0833mm respectively for the reference case which is define in table 3.1.

The pressure distributions for the three cases considered are shown in figure 2.4 for the time instant when the pressure spike is located at $r \approx 5$ cm (t = 0.0039 s). The difference between the different cases is quantified using *NRMSE*, which is shown in figure 2.5 up to the time when the negative pressure spike appears at ≈ 5 cm . Noticable from the plot, the maximum error decreased from approximately 10% for the case between 300 and 600 points to less than 1% for the case between 600 and 1200 points. Therefore, 600 grid points on the wall were used for all wall-pressure results reported in Chapter 3.

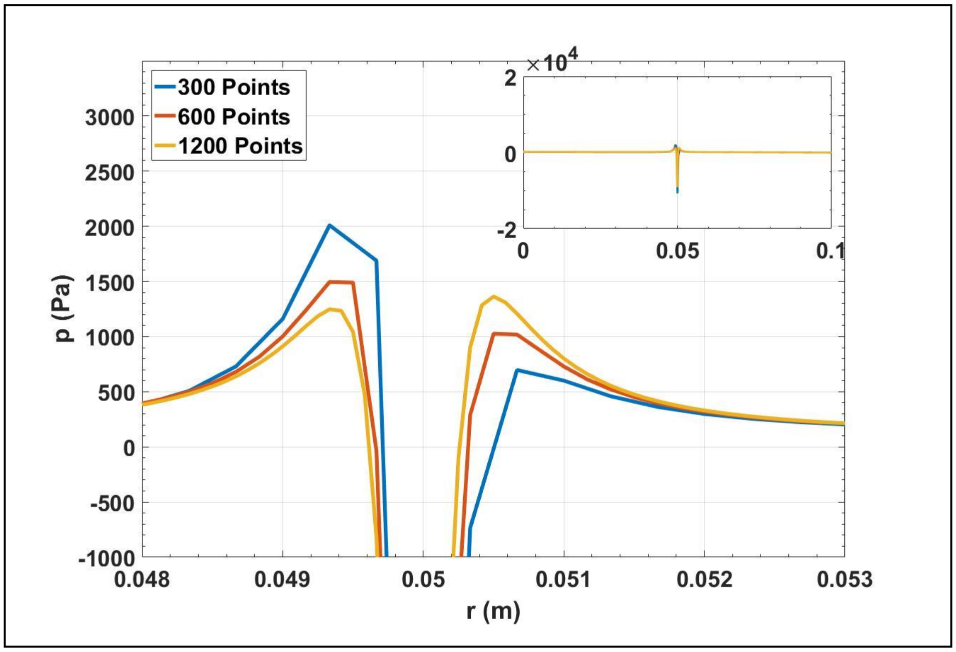

Figure 2.4 Radial wall-pressure distribution at the time instant when the negative pressure spike (minimum pressure) associated with vortex passing is located at $r \approx 5$cm. Different color lines represent a different number of wall grid points used for computing the wall pressure (as given by the legend). The inset shows the overall distribution, while the main plot depicts a magnified view to show the change between the different cases.

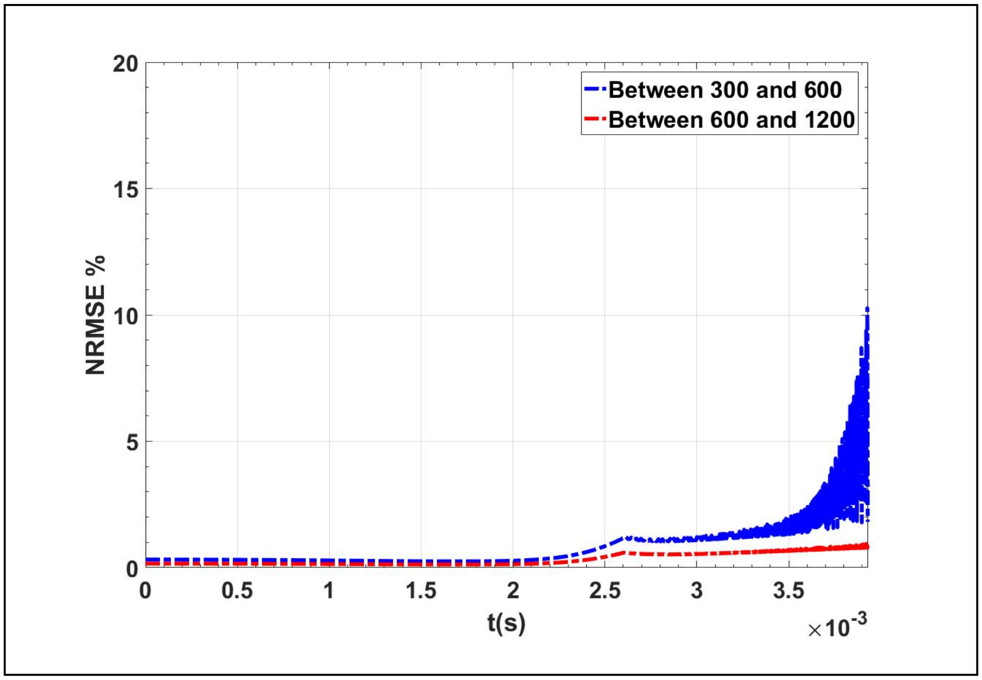

Figure 2.5 Normalized Root Mean Square Error (*NRMSE*) resulting from comparing the results of grid resolution 300 and 600 points (blue) and 600 and 1200 points (red). The results are shown up to the computation time corresponding to the time instant when the negative pressure spike appears at $r \approx 5$ cm.

2.4.1.3 Validation of the Time Step Size

The final validation step is to verify the size of the time step to produce results with an acceptable accuracy while minimizing time and computer resources. For this evaluation, three-time steps are used corresponding to 1000, 2000 and 4000-time steps during the period between injecting two successive vortices in the domain. The corresponding time step is 4.06, 2.03, and 1.016 μs, respectively, for the vortex passage frequency considered (details of how the physical value of frequency is determined will be given in Chapter 3). All other model parameters are as described in Chapter 3. The computational time for the three different cases varied from approximately 10 minutes for 1000 points/cycle to 40 minutes for 4000 points/cycle for $f \approx 245$ Hz.

Pressure distributions for the three-time steps utilized are shown in figure 2.6 at the instant when the pressure spike is located at $r \approx 5$ cm (t = 0.0039 s). As before, the difference between the different cases is quantified using *NRMSE* in figure 2.7. As seen from the plot, the maximum error decreased from 3% when comparing between 1000 and 2000 point per cycle (*PPC*) to 1.65% between 2000 and 4000 point per cycle (*PPC*). All computations done here utilized 2000 *PPC*.

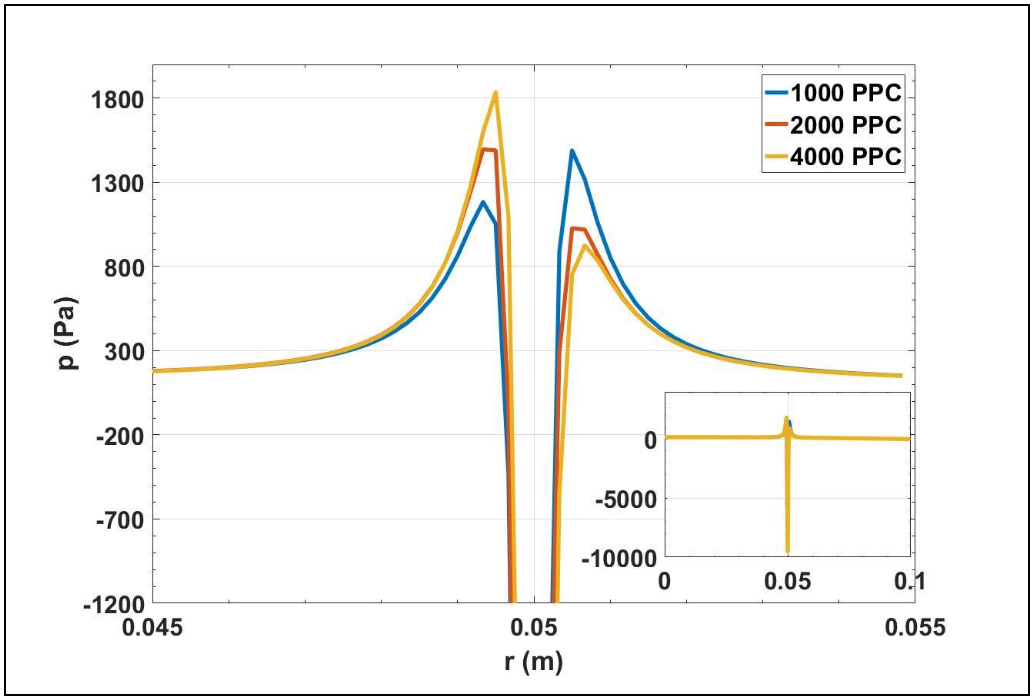

Figure 2.6 Radial wall-pressure distribution at the instant when the negative pressure spike (minimum pressure) associated with vortex passing is located at $r \approx 5$cm. Different color lines represent a different number of computational time steps in the period between injecting two successive vortices (as given by the legend). The inset shows the overall distribution, while the main plot depicts a magnified view to show the change between the different cases.

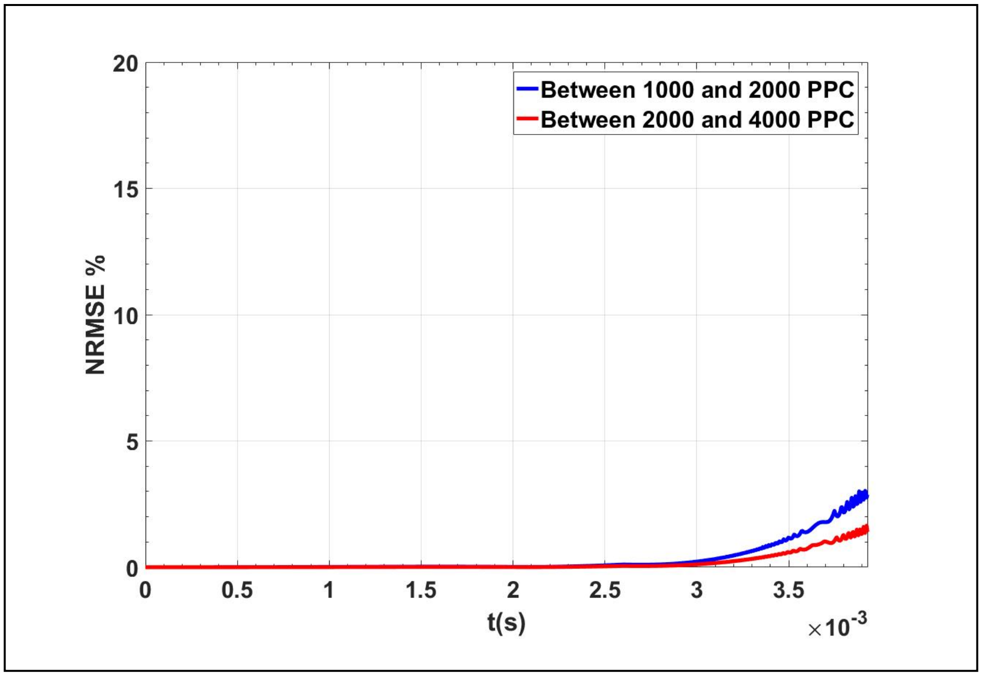

Figure 2.7 Normalized Root Mean Square Error (*NRMSE*) resulting from comparing the results of time step 4.066e-06 s (1000 *PPC*) and 2.033e-06 s (2000 *PPC*) (blue) and 2.033e-06 s (2000 *PPC*) and 1.0161e-06 s (4000 *PPC*) (red). The results are shown up to the computation time corresponding to the time instant when the negative pressure spike appears at $r \approx 5$cm.

2.4.2 Application to a Line Vortex Above a Flat Wall

To validate the overall unsteady-wall-pressure computational approach and the implemented algorithms, it was desired to apply the method/algorithms to a closely related problem, where an analytical solution for the unsteady wall pressure is known. The problem of a line vortex above a wall seemed to be appropriate. Similar to the vortex-ring problem, the presence of the line vortex above a flat wall, as depicted schematically in figure 2.8, is modeled using an imaginary image vortex placed symmetrically relative to the wall. The presence of this image vortex causes advection of the vortex pair in the positive streamwise direction (for the given sense of circulation), producing an unsteady wall-pressure imprint on the wall. Physically, this scenario is similar to that of the vortex ring once it changes its advection direction from being predominantly towards, to being approximately parallel to the wall. In both the line and ring vortex cases, the unsteady pressure field at a given point on the wall is caused by the passage of vortices above the point. Therefore, the ability to reproduce the unsteady wall-pressure field of the line vortex accurately using the tools developed for the impinging jet problem provides further confidence in the implementation of the model developed in the present work.

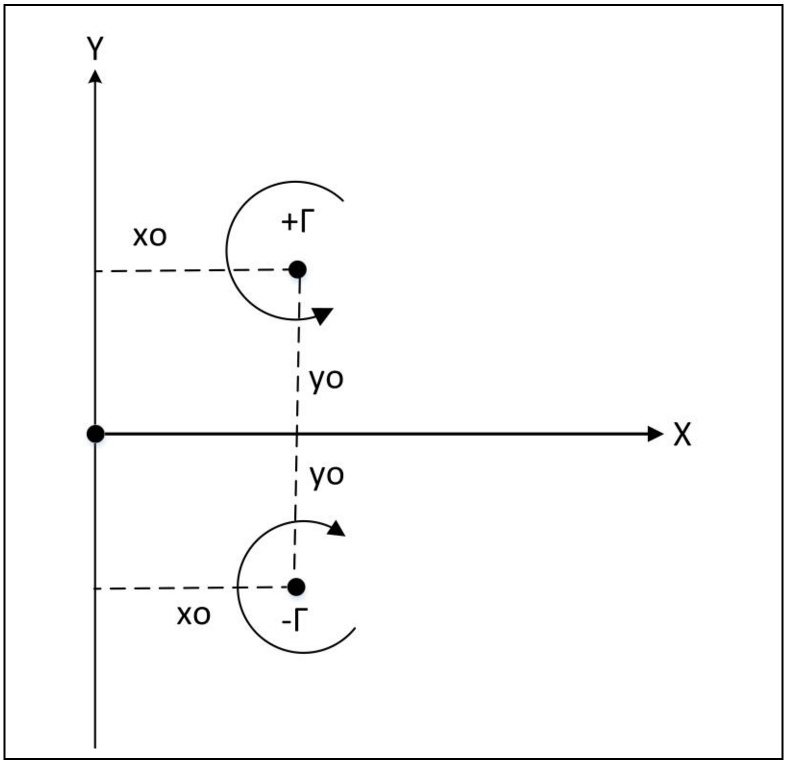

Figure 2.8 Schematic of a line vortex centered at (x_o, y_o) above an infinite flat wall at y = 0. An image vortex centered at (x_o ,-y_o) models the presence of the wall.

The velocity, and velocity potential for the line vortex problem are given by [21]:

$$u = \frac{\Gamma}{2\pi}\left[\frac{2y_o}{(x - x_o)^2 + (y_o)^2}\right] \tag{2.31}$$

$$\frac{d\phi}{dt} = -\frac{4\Gamma^2 y_o^2}{\Gamma^2 t^2 - 8\Gamma\pi t x y_o + 16\pi^2 y_o^2 (x^2 + y_o^2)} \tag{2.32}$$

The corresponding wall-pressure distribution at a given time instant is computed using equations (2.31) and (2.32) in conjunction with equation (2.28). The numerical implementation is the same as described in Section 2.3. For this calculation, the vortex and computational parameters are kept the same as for the vortex ring case (without the inclusion of the stagnation flow). Specifically, the parameters values are:

- Domain size: $10\mathrm{cm}$
- Time step: $2.0331\ \mu\mathrm{s}, or\ 2000\ \ \mathrm{Points/cycle}$
- Circulation: $\Gamma = 0.1798\ \ \mathrm{m^2/s}$
- Wall resolution: $0.16\ \mathrm{mm}, or\ 600\ grid\ points\ across\ the\ domain$
- Vortex location above the plate $y_o = 5$ mm

Figure 2.9 depicts the wall-pressure signature obtained analytically and computationally, concurrently with the streamlines at selected time steps. The streamlines are depicted in a frame of reference convecting with the vortex but placed at the appropriate *x* location as the vortex travels in the positive x-direction. Beneath the center of the “circular” streamline pattern a negative pressure peak is found; as expected. Two additional positive, but substantially weaker, peaks are found ahead and behind the vortex center. Overall, excellent agreement is found between the computed and analytical wall pressure distribution even up to the time when the vortex is fairly close to the reference point (subplot f in figure 2.9). This agreement is quantified by calculating the *NRMSE*, which is displayed in figure 2.10 versus time. For this plot, the time shown is only up to the point when the vortex center reaches *x* = 5 cm. As seen from the figure, the *NRMSE* does not exceed 0.3% over the entire duration depicted.

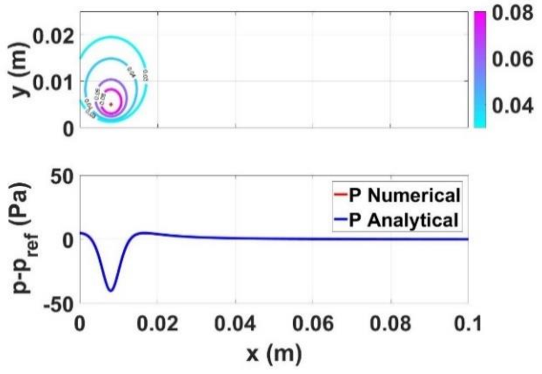

(a) Time=0.00278 s

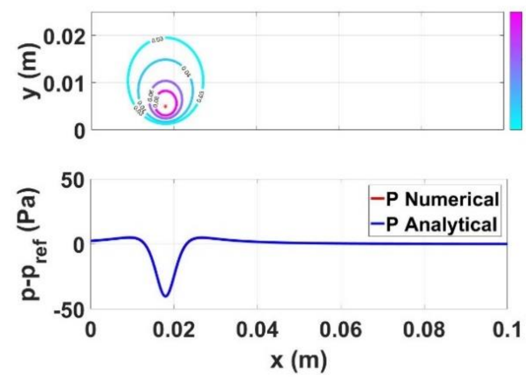

(b) 0.00627 s

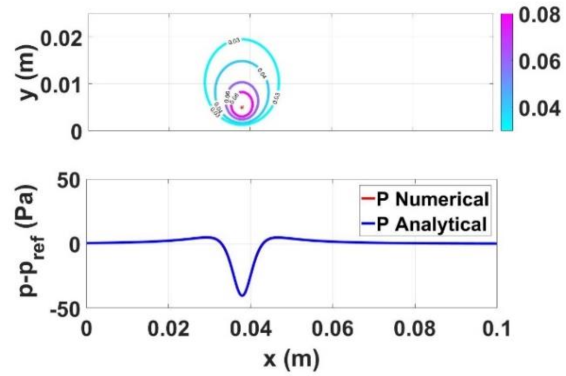

(c) 0.01324 s

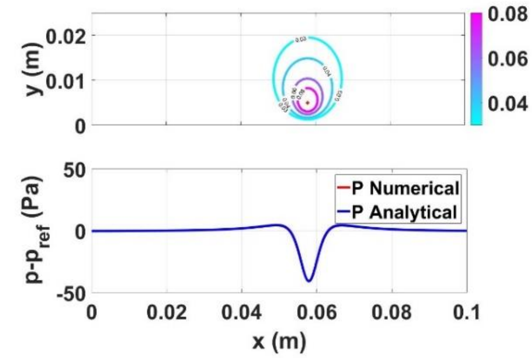

(d) 0.02022 s

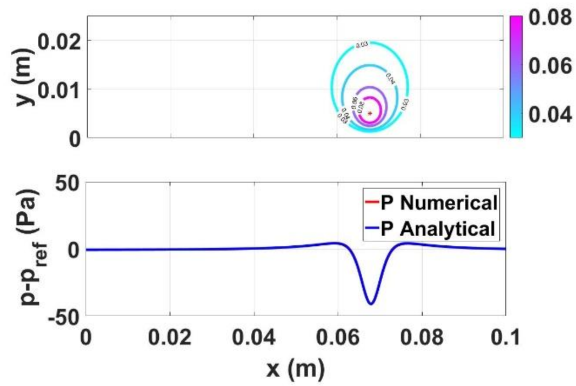

(e) 0.0237 s

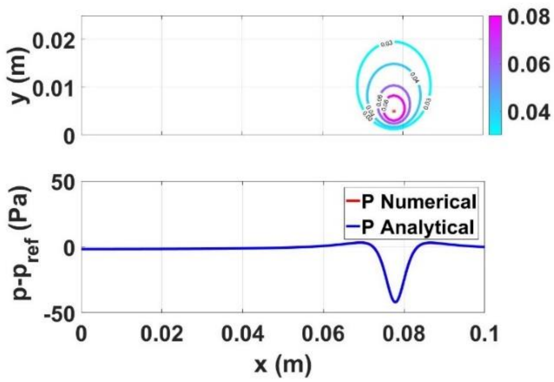

(f) 0.02719 s

Figure 2.9 Computational and analytical results of the wall pressure and associated streamlines for a line vortex above a wall. Different subplots represent different times (as indicated beneath the plots). The streamlines are shown in a frame of reference convecting with the vortex.

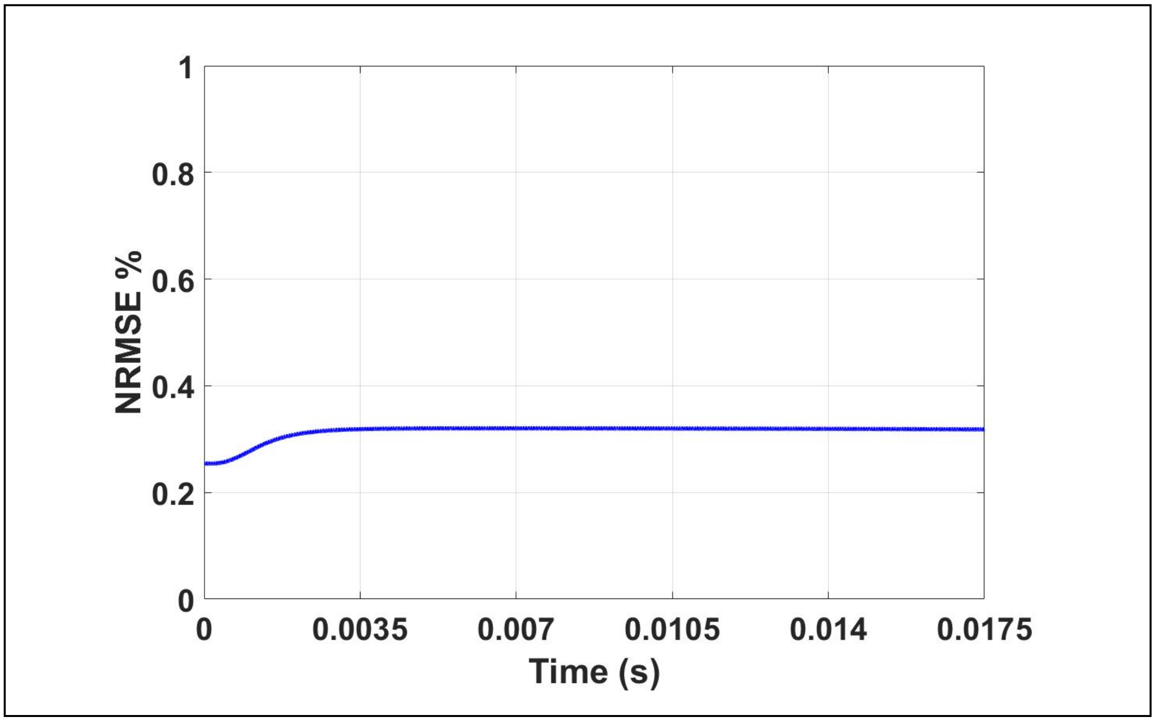

Figure 2.10 Normalized Root Mean Square Error (NRMSE) between analytical and numerical values of the wall-pressure distribution beneath a line vortex above a flat wall. The time duration shown is from the start of the vortex motion until the vortex center is located at r = 5 cm.

CHAPTER 3: Mathematical Model Results

This chapter will focus on the interpretation of the mathematical model results including the mean and Root Mean Square (RMS) of the fluctuating pressure. The analysis was done for three main cases. For each case, the solution was obtained when changing only one parameter while the other parameters remained unchanged. This facilitates understanding the effect of changing each of these parameters on the wall-pressure characteristics. In fact, varying one parameter at a time is one advantage of the model because in the actual flow it is generally not possible to change these parameters independent of one another. The three parameters examined are: vortex passage frequency (f), jet Reynolds number Re_D, and vortex circulation (Γ). Though the model is inviscid, a "Reynolds number" may still be defined in relation to the jet diameter (vortex ring diameter) and initial jet velocity (stagnation flow velocity at top of the computation domain) in order to facilitate comparison with actual jet flow results.

The nominal values of the model parameters were selected to be representative of an actual jet flow at the end of the potential core. The details of determining these values follow. Crow and Champagen [14] showed that the jet unsteadiness at the end of the potential core is dominated by the preferred, or column, mode with a Strouhal number of $St \approx 0.3$. Thus,

$$\frac{fD}{U_j} = 0.3 \tag{3.1}$$

In the model, the jet diameter D is reasonably equivalent to twice the vortex ring radius; i.e. $D = 2R_o$, and the jet velocity U_j to the centerline velocity of the stagnation (advection) flow at the top of the computational domain; i.e. $U_j = 2aZ_o$. Making these substitutions in equation (3.1):

$$f = \frac{0.3aZ_o}{R_o} \tag{3.2}$$

In equation (3.2), both Z_o and R_o are known a priori. Z_o is the height of the computational domain, and R_o is the initial vortex ring radius (equivalent to the jet exit radius), which is arbitrarily selected without loss of generality since it is also chosen as the length scale for making quantities non-dimensional. To determine a, and hence the vortex passing frequency via equation (3.2), use is made of Re_D:

$$Re_D = \frac{U_j D}{\nu} = \frac{(2aZ_o)(2R_o)}{\nu} \tag{3.3}$$

where, ν is the kinematic viscosity. Equation (3.3) leads to:

$$a = \frac{\nu * Re_D}{4 * R_o * Z_o} \tag{3.4}$$

Hence, by specifying the ring radius, jet Reynolds number and knowing the computational domain height it is possible to compute the nominal vortex passage frequency (corresponding to the jet column, or preferred mode). Because the jet preferred mode frequency corresponds to the vortex passage frequency at the end of the potential core, the frequency calculated as outlined above represents vortices near the end of the potential core (approximately $4D$ downstream of the jet exit). To model vortex passage at locations closer to the exit of the jet, use is made of the fact that the terminal vortex passage frequency of the preferred mode is the result of successive pairings of vortices, which initially form as an instability of the jet shear layer, rather than the jet column. With each pairing, the vortex passage frequency drops by a factor of 2. Hence, to represent vortex passage at distances closer to the jet, the nominal frequency is increased by a factor of 2, 4, etc.

To connect the nominal vortex circulation (Γ) value to the jet flow, use is made of the approximation of the circulation for a shear layer (Koochesfahani and Dimotakis [22]):

$$\Delta U \approx \frac{\Gamma_{sl}}{\lambda} \tag{3.5}$$

where, ΔU is the velocity difference across the shear layer, λ is the wavelength between vortices, and Γ_{sl} is the circulation around a contour that encompasses the shear layer and extends a length λ in the streamwise direction. Equation (3.5) assumes all vorticity is concentrated in the shear layer vortices and is equivalent to computing the velocity jump across a zero-thickness potential vortex-sheet from the circulation density (circulation per unit length) along the sheet. For the jet flow $\Delta U = U_j$ and $\lambda/D = 2.38$ [23], thus:

$$\Gamma = \lambda * U_j = 2.38(2R_o)(2aZ_o) = 9.52aR_oZ_o \tag{3.6}$$

For all cases studied, parameters-maintained constant are

- Computational domain's radial extent: $L_r = 0.1$ m (see figure 2.1 for definition). L_r is selected to be much larger than R_o and to ensure invariance of the results with further increase in L_r, as discussed in Chapter 2;
- Initial vortex ring radius: $R_o = 0.0048$ m;
- Initial wall-normal distance between the vortex ring and the impingement plate (also wall-normal extent of the computational domain L_z): $Z_o = 5R_o = 0.024$ m. This value was not critical. If Z_o is increased, the vortices will travel a longer distance towards the wall before they have any effect on the wall. Since the focus of the model is on the wall-pressure, Z_o needs to be larger than or equal to the height at which the vortex presence affects the wall pressure. The choice of five times the ring radius fulfills this requirement for all cases examined here;
- Volumetric constant (C) in equation (2.7): $C = 0.033 \times 10^{-6}$ m^3. This value was taken to be the same as used by Walker *et al* [18]. The specific value of C is not critical since it only

affects the self-induced velocity of the vortex, which in turn only affects how quickly the vortex ring lineally approaches the wall.

- Air kinematic viscosity (at 20°C): $\nu = 15.11 \times 10^{-6}$ m^2/sec. Air is selected as the fluid since the results of the model are compared to the measurements in an air jet in Chapter 5.

With R_o and Z_o values fixed, the selection of Re_D, sets a (equation 3.4), which in turn sets f and Γ (equations 3.2 and 3.6, respectively). A *reference* case was arbitrarily selected to correspond to $Re_D = 5{,}000$, resulting in $f = 245.9$ Hz and $\Gamma = 0.1798$ m^2/s. This reference case was repeated in three series of parametric investigations aimed at examining the influence of f, Re_D and Γ on the wall pressure. Each series contained three cases, including the reference and involved varying only one parameter, while all other parameters remained fixed in order to isolate the influence of each parameter. This one parameter at a time variation is only possible using a mathematical model since in the real jet f, Re_D and Γ are generally interdependent. Indeed, this independence is even reflected in equations (3.2), (3.4) and (3.6), which attempt to mimic the real jet flow in a simplistic way.

The parameter values for all cases investigated are summarized in table 3.1. For the frequency series, two other frequencies representing doubling and quadrupling the reference-case frequency are examined. As discussed earlier these higher frequencies represent vortex passage prior to the second and first vortex pairing, respectively, in the real jet (which corresponds to shorter jet to impingement plate distance). For the Reynolds number cases, the three values utilized are $5000, 15000, and\ 25000$. Finally, the three cases in the circulation (Γ) series are those from the reference case (0.1798 m^2/s), and the others taken to be half and double of the reference circulation. For each series, the reference case is highlighted in table 3.1 using green color.

case	Reynolds number (Re)	Frequency (f)Hz	Jet velocity (U_j) m/s	Circulation (Γ) m^2/s	Constant (a) 1/s
Frequency (f)	5000	245.9	7.8698	0.1798	163.954
	5000	491.8	7.8698	0.1798	163.954
	5000	983.6	7.8698	0.1798	163.954
Reynolds number (Re_D)	5000	245.9	7.8698	0.1798	163.954
	15000	245.9	23.6094	0.1798	491.862
	25000	245.9	39.3490	0.1798	819.77
Circulation (Γ)	5000	245.9	7.8698	0.0899	163.954
	5000	245.9	7.8698	0.1798	163.954
	5000	245.9	7.8698	0.3596	163.954

Table 3.1 Model parameters for frequency (f), Reynold number (Re_D), and circulation (Γ) cases. Rows highlighted in green depict the parameters for the reference case

3.1 Frequency Effect

Figure 3.1 and 3.2 show snapshots of the streamlines of the computed flow and associated wall-pressure for the lowest and highest frequency respectively. In each figure, the point-vortex location is indicated with an asterisk. In both figures, a given vortex approaches the wall moving vertically downwards without much change in the radial location, until the vortex is very close to the wall where the main travel direction switches from towards to parallel to the wall. The main difference between the two frequency cases is that multiple vortices are seen within the computational domain in the high-frequency case (figure 3.2). The spacing between the vortices initially decreases, as they approach the wall, resulting in packing them rather densely within the stagnation zone. Subsequently, as the vortices travel parallel to the wall, their spacing increases substantially. The change in the vortex spacing is related to their convection velocity. Initially, as they move towards the wall, their convection velocity decreases (due to the decrease in the stagnation flow wall-normal velocity and the opposing influence of the image vortex). Once they "turn the corner", radial velocity acceleration of the stagnation flow and the induced radial velocity by the image vortex both combine to "shoot" the vortex away from the stagnation zone. As a result, within the wall-jet zone the spacing of the vortices is increased substantially.

In the wall-jet zone, because the vortices are spaced far apart, regardless of their frequency, their wall-pressure signature is similar in character in both the low- and high-frequency cases. This signature takes the form of a negative pressure spike immediately beneath the vortex (where the induced velocity by the vortex is highest on the wall) surrounded by two small positive peaks up and downstream of the negative peak. This signature, which is consistent with the expected "focusing" of the stream lines beneath a vortex (see figure 2.9), can be observed best at the last time instant (largest r/D_o vortex location) in figures 3.1 and 3.2. The negative spike first appears when the vortex gets close enough to the wall (as will be seen later, this takes place within the stagnation zone, between $r/D = 0.5$ and 1), then it monotonically increases in magnitude as the vortex travels radially outwards. This monotonic increase is caused by the continuous decrease in the vortex distance to the wall with increasing time. Since potential vortices are employed in the present model, as the wall nears the vortex center, the induced velocity on the wall becomes higher and higher, and therefore the corresponding pressure is expected to become lower and lower.

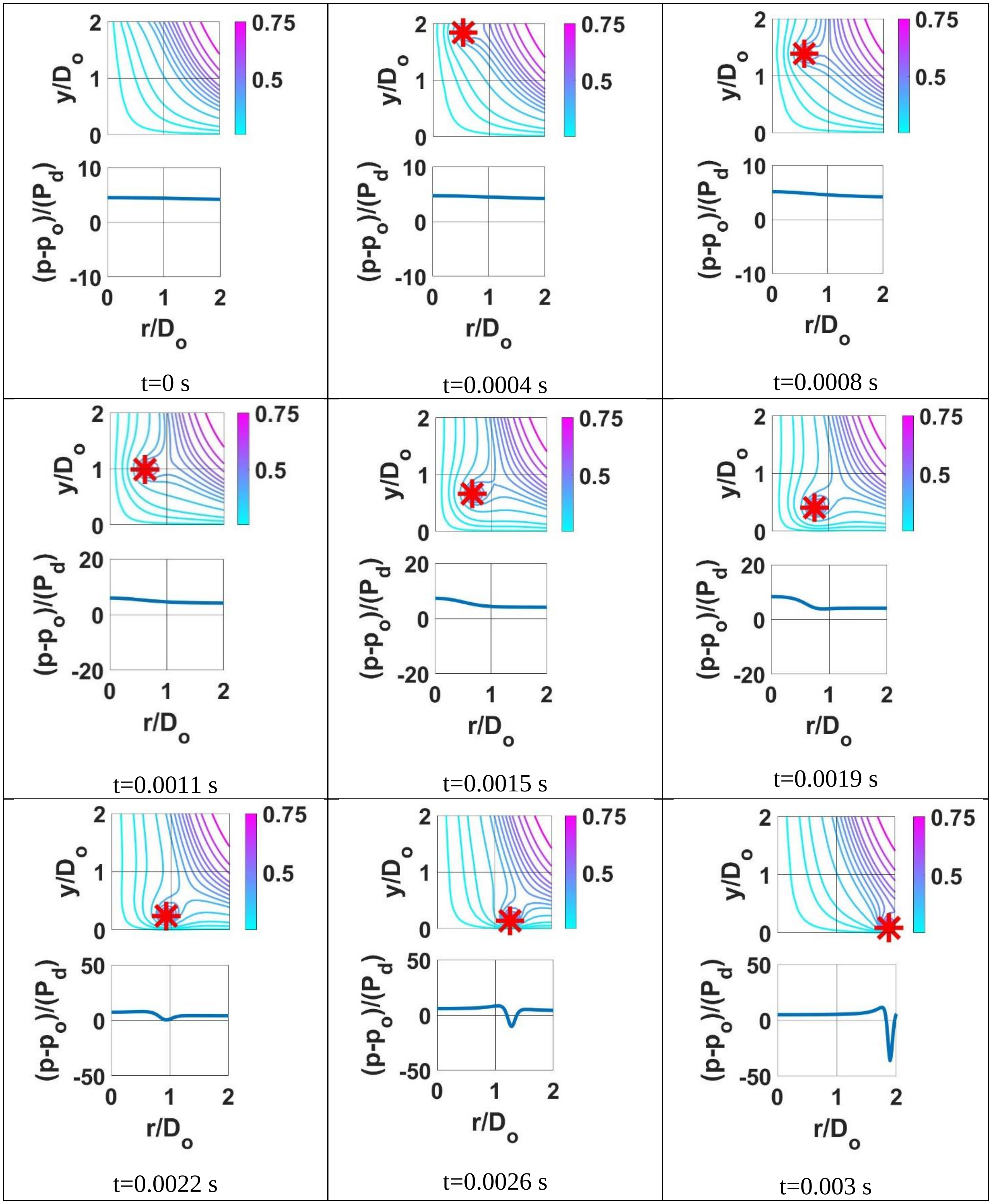

Figure 3.1 Streamlines and normalized pressure at different time steps for frequency $f \approx 245\ Hz$, *Re*=5000, and circulation $\Gamma = 0.1798\,\mathrm{m^2/s}$

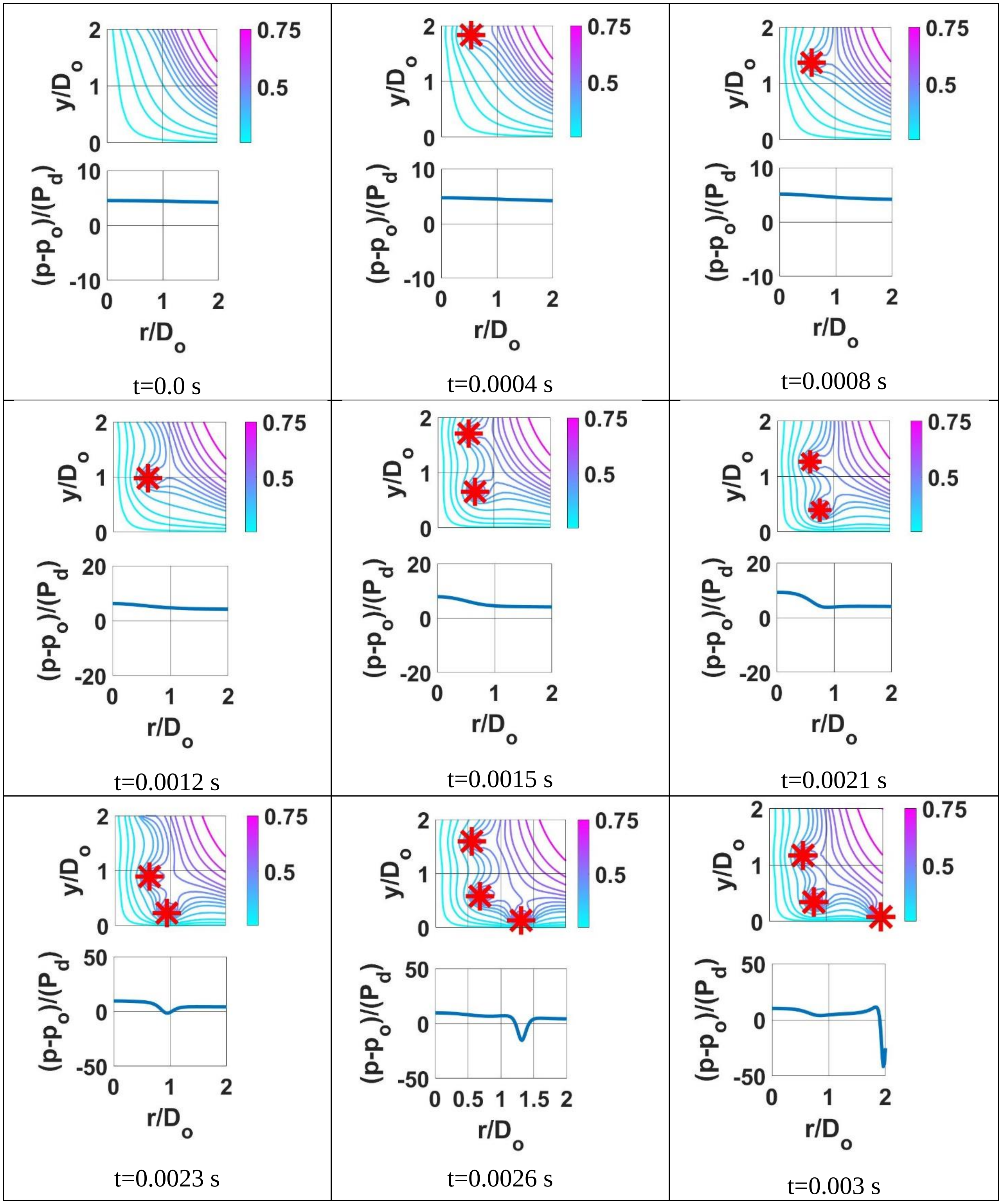

Figure 3.2 Stremlines and normalized pressure at different time step for frequency *f*= 980 Hz, *Re*=5000, and circulation $\Gamma = 0.1798\,\mathrm{m^2/s}$

To examine the wall-pressure characteristics quantitatively, radial profiles of the mean and *RMS* pressure are computed. Both of these quantities are calculated over one period of oscillation $(1/f)$ after the initial transients of starting the calculation have passed. The mean pressure distribution is shown in figure 3.3 in the form of a mean-pressure coefficient $C_p = (p - p_o)/P_d$; where P_d is the dynamic pressure based on U_j, for a truncated radial domain that focuses on the stagnation zone. The latter is delineated in these figures, as well as similar ones later in the chapter, using broken green lines. As seen in figure 3.3, the mean pressure has its maximum at the stagnation point (as expected). It should be clarified that the stagnation point pressure coefficient exceeds unity because of three reasons. First, the dynamic pressure used for normalization is computed using a velocity scale that is representative of the stagnation (advection) flow only. Therefore, any added mean streaming velocity towards the wall due to the presence of the vortices does not affect the velocity scale. The added velocity would increase the stagnation pressure beyond that of the stagnation flow alone, causing the pressure coefficient to go beyond unity. The difference between the overall pressure and that due to the stagnation flow alone can be seen in figure 3.3, where C_p of the stagnation flow alone is also plotted (indicated with *SP* in the legend). As expected, this distribution does not vary with frequency. Second, the reference pressure P_o used in defining C_p is taken from a different spatial location $(z = 0, r = L_r)$ than that where U_j, and hence P_d, is calculated $(z = L_z, r = 0)$. Third, the flow is unsteady, and therefore, generally speaking, the stagnation pressure coefficient need not be unity.

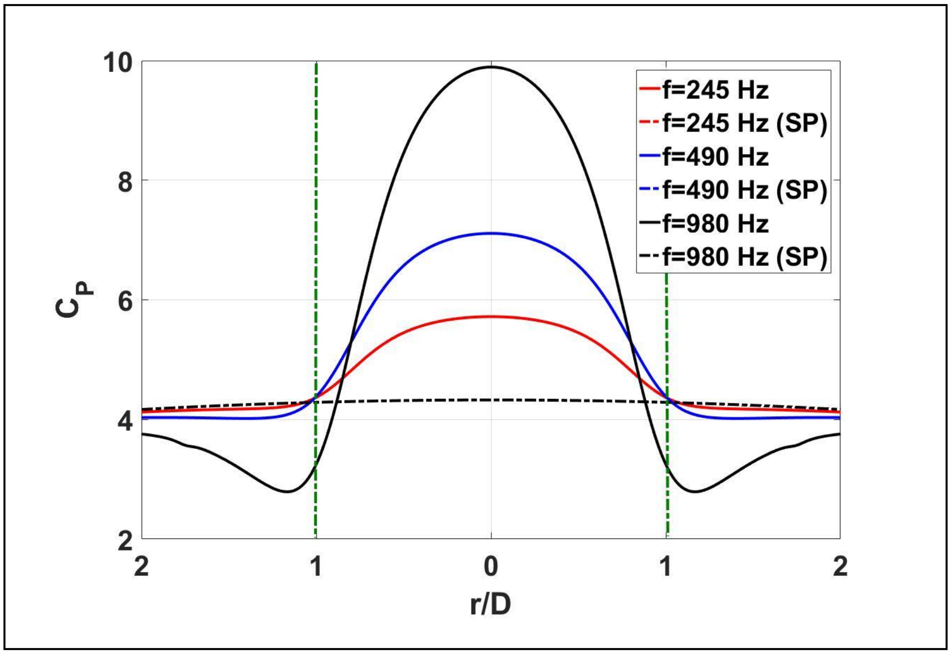

Figure 3.3 Effect of vortex passage frequency on the radial distribution of the mean pressure coefficient. The green broken lines outline the boundary of the stagnation zone

Figure 3.3 shows that C_p at the stagnation point increases with increasing frequency. This effect can be understood as being caused by the net streaming velocity induced by the vortices towards the wall. As the frequency increases, more vortices are present simultaneously within the stagnation zone (e.g. compare figures 3.1 and 3.2), and the superposition of their induced velocity increases with the number of vortices, leading to larger stagnation pressure. Another interesting effect is the development of a local negative peak just outside the stagnation zone, which is seen clearly for the highest frequency. This effect is also understood to be caused by the net streaming velocity induced on the wall by the collective effect of the vortices, which becomes stronger with increasing frequency. Unlike the streaming effect towards the wall at $r/D = 0$, which understandably produces a positive pressure peak on the wall at the stagnation point, when the flow velocity is forced to zero, the stronger the wall-parallel velocity induced by the vortices, the lower the pressure. The presence of a localized peak at a given radial location, for large enough frequency, is indicative of the location where the collective influence of the vortices is highest. As discussed in figure 3.2, as the vortices approach the wall, they get packed densely resulting in maximum collective effect. However, subsequently the vortex spacing increases substantially reducing this effect. The negative peak in the mean pressure distribution is believed to be a manifestation of this behavior when enough vortices are present in the simulation (i.e. when the vortex passing frequency is high enough). The negative peakon figure 3.3 can be explained alternatively based on figures 3.1. and 3.2. More tightly packed vortices means a larger "induced" flow. Since this flow cannot bypass the streamlines, the velocity is increased in regions where the spacing between streamlines is reduced. That is the place where the vortices first approach the wall. Since vortex injection frequency is higher, streamlines tend to stay closer to each other almost permanently at that point.

The radial distribution of $C_{prms} = p_{rms}/P_d$ is depicted in figure 3.4. Two different trends are observed with increasing frequency. In the first “half” of the stagnation zone (below $r/D \approx 0.5$), the level of pressure fluctuation decreases with increasing frequency, while the opposite takes place for larger r/D values. For all frequencies, the distribution is “flat” depicting insensitivity to r/D near the stagnation point. As r/D increases beyond this flat zone, two different behaviors are seen, depending on frequency. At low frequency, a decrease in the *RMS* level is observed with the increase in r/D, before a monotonic increase is observed. The initial decrease with r/D becomes smaller with increasing frequency, eventually disappearing at the highest frequency, where the *RMS* level increases monotonically with r/D beyond the initial flat distribution near the stagnation point.

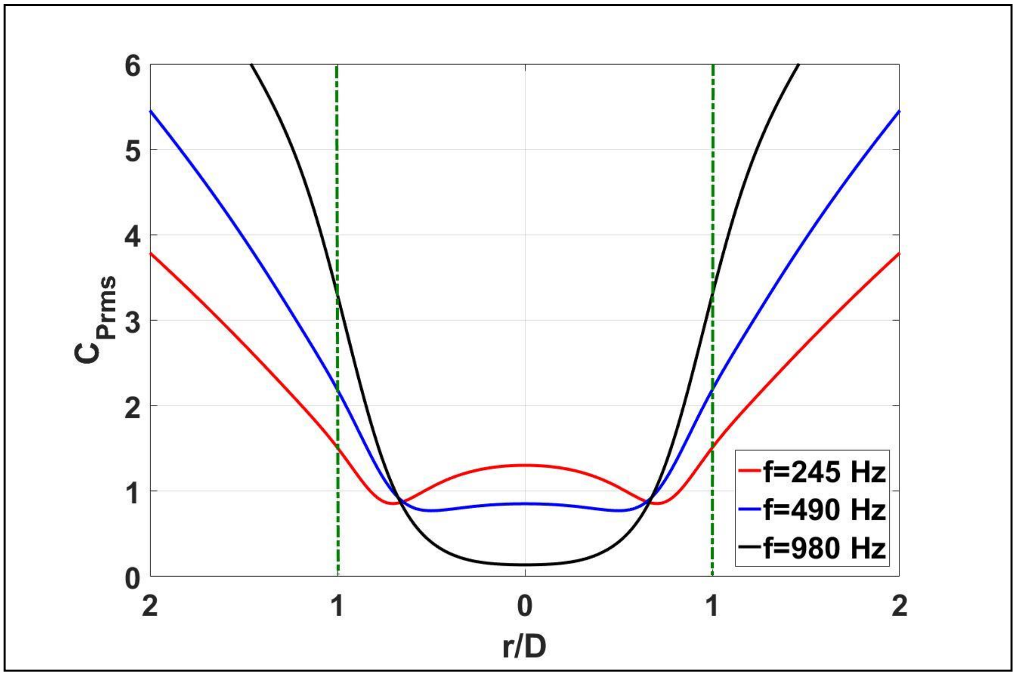

Figure 3.4 Effect of vortex passage frequency on the radial distribution of the *RMS* pressure coefficient. The green broken lines outline the boundary of the stagnation zone

Possible physical reasoning for the trends observed in the C_{prms} distributions could be developed via inspection of sample pressure times series. Figure 3.5 depicts pressure signals for one cycle of vortex passage at various *r/D* locations within the stagnation zone. Two plots are included in the figure for the lowest and highest frequencies; $f \approx 245$ Hz (top) and $f \approx 980$ Hz (bottom), respectively. For both cases, the general features of the signals are qualitatively similar, depicting a fundamental difference in the signal shape between radial locations that are below approximately $r/D \approx 0.5$ and those that at larger radial locations. For r/D locations larger than 0.5, an energetic pressure signature that is characterized by a strong negative peak is observed. As discussed in figures 3.1 and 3.2, the strong/narrow negative pressure peak is found directly beneath the vortex closest to the wall, and is produced by vortex passage. Once seen at the wall, this peak continuously increases in magnitude with r/D since the vortex's distance to the wall continuously decreases as the vortex convects radially outwards. This increase in negative-peak strength is seen in figure 3.5 between $r/D = 0.75\ and\ 1$, for both frequencies.

Below $r/D \approx 0.5$, the pressure signal has lower magnitude, it looks more “sinusoidal” and it does not exhibit the strong negative peak characteristic of vortex passage. Since the only unsteadiness in the model originate from vortex passage, there is no doubt that the unsteady pressure is still connected to the vortices; it is just that the unsteadiness does not reflect the strong local effect, near the vortex core. Therefore, hereafter the pressure unsteadiness is characterized as *remote* for $r/D < 0.5$, and *local* for $r/D > 0.5$. The remote effects are more harmonic and weak in nature, and the local effect are strong and only felt at the wall for sufficiently large r/D. For real (viscous core) vortices, the distinction between local and remote is expected to depend on how far is the point of observation from the vortex-core center relative to the vortex core radius. Since the vortex core size increases with each merging, one would expect that local effects would extend farther and farther with merging. This physical hypothesis cannot be tested with the present model, which is based on zero-core-size potential point vortices.

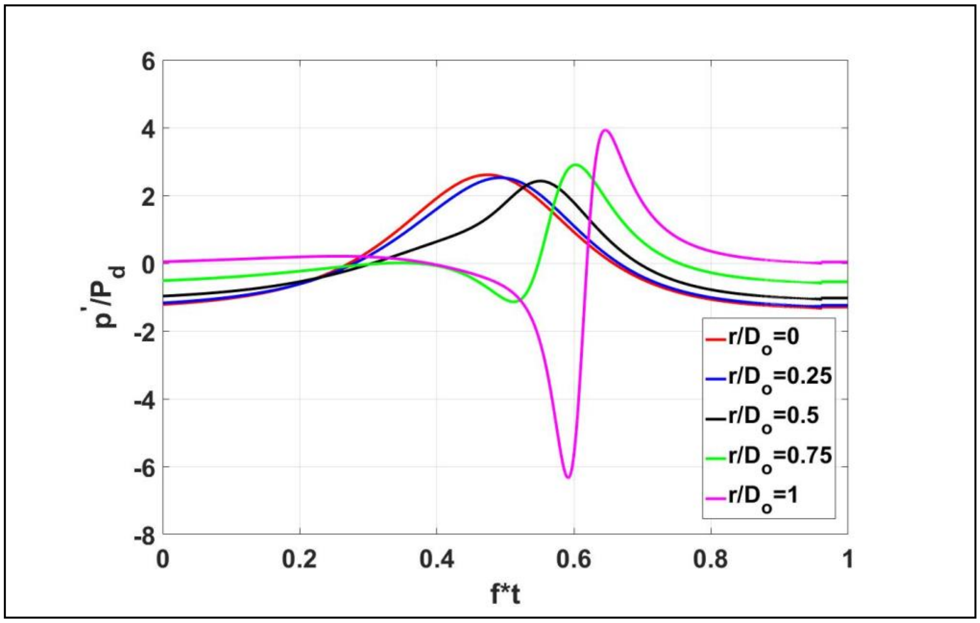

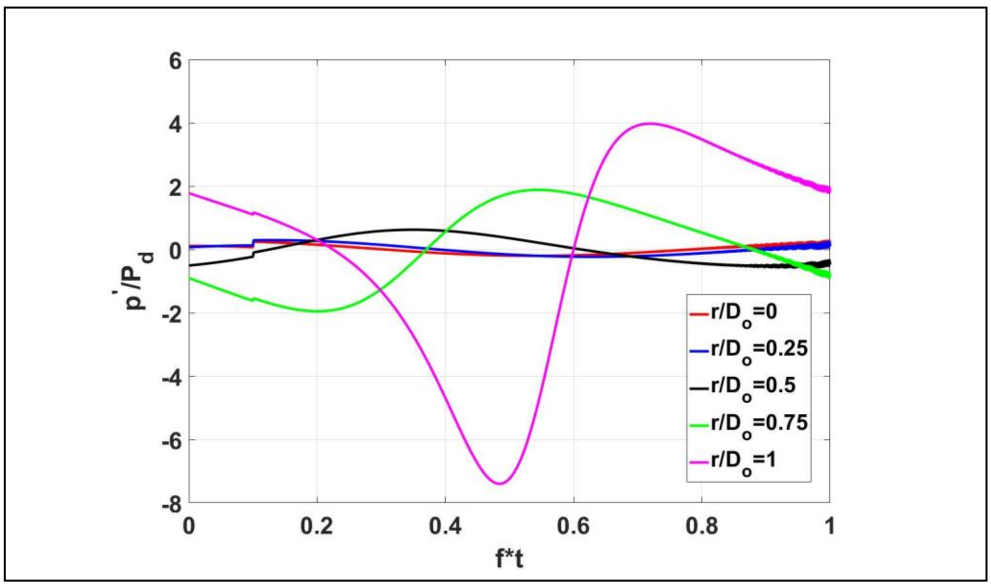

Figure 3.5 Pressure time series at various *r/D* locations within the stagnation zone, *Re*=5000, $\Gamma = 0.1798\,\mathrm{m}^2/s$, and $f \approx 245$ Hz(top) and $f \approx 980$ Hz $(Bottom)$. The small discontinuities in the time series for $f \approx 980\ Hz$ correspond to the time instant when a new vortex is injected at the top of the computational domain. Because the discontinuities are small, no attempt was made to get rid of them by using a larger wall-normal extent for the computational domain.

The discussion of figure 3.5 provides insight regarding the effect of r/D on C_{prms} in the stagnation zone. To analyze the influence of frequency, pressure time series at the same radial location but different frequencies are shown in figure 3.6. Two radial locations are chosen, at the start and end of the stagnation zone: $r/D = 0$ (top) and $r/D = 1$ (bottom), respectively. These two locations are chosen because one of them exhibits decrease in pressure fluctuation level with frequency ($r/D = 0$), and the other, the opposite. Focusing first at the stagnation point, the decrease in the amplitude of the sinusoidal-like pressure variation with increasing frequency is obvious. This trend may be clarified as follows: per earlier discussion of figures 3.1 and 3.2, as the frequency increases, the vortices become packed densely near the wall within the stagnation zone. As a result, the induced velocity on the stagnation streamline (i.e. the flow approaching the stagnation point) by the individual vortices become increasingly overlapping. This reduces the vortex-to-vortex velocity fluctuation, and leads to more of a steady streaming flow with increasing frequency.

To substantiate this physical picture just described, figure 3.7 shows the induced velocity along a line that is parallel to an array of line vortices with varying inter-vortex spacing: 10 mm, *50 mm*, and *500 mm*. This simple situation is intended to emulate the influence of the "packing density" of the vortices on a line parallel to the array (similar to how the vortices approaching the wall are parallel to the stagnation streamline in the present model). The results in figure 3.7 are plotted for only one wavelength (i.e. for a length equal to the spacing between the vortices), since outside the shown range, the induced velocity would repeat periodically for an infinite array. For all vortices in the array, the circulation is the same. As seen from figure 3.7, for the largest wavelength (smallest packing of vortices), the vortices are spaced so far away that the induced velocity from the neighboring vortices has no influence within the wavelength shown (as seen from the velocity practically decaying to zero at the ends of the wavelength). As the vortices become more packed ($\lambda = 50$mm), the effect of neighboring vortices overlaps more, causing an overall rise in the mean velocity (i.e. increasing streaming effect), and a reduction in the velocity fluctuation (since the induced velocity amplitude does not fall too much before the influence of a neighboring vortex is felt). This trend is particularly evident for the highest vortex packing ($\lambda = 10mm$), where the induced velocity is practically steady, having the strongest streaming component and no fluctuation.

On the other hand, within the zone where the local vortex effects are felt (bottom plot in figure 3.6), the pressure amplitude increases only slightly with increasing frequency, suggesting that this increase is not responsible for the strong increase in *RMS* with frequency seen in figure 3.4. Instead, a substantial broadening of the pressure peaks is found to take place with increasing frequency. This shows that the monotonic increase in C_{prms} with frequency for $r/D > 0.5$ is a result of an increase in the “duty-cycle” of the pressure signal, rather than in its magnitude. This broadening is again a result of the increase in the number of packed vortices affecting the pressure as the frequency increases. However, unlike $r/D < 0.5$, the effect of vortex packing relates to the induced velocity along a line that is practically normal, rather than parallel, to the vortex array, which leads to a different influence of vortex packing.

To further clarify the effect of vortex spacing on the induced velocity on the wall, a simple situation is considered where three line vortices are placed at the same positions relative to a wall as the vortices in the model when the leading vortex center is at $r/D = 1$ (i.e. the same location for which the time series are shown in figure 3.6). The induced velocity on the wall by each of these vortices is plotted in figure 3.8 versus distance along the wall, together with the velocity induced by all of them. If the vortex spacing is so large such that only one vortex passes through the domain at a time (as in the low-frequency case of the present model), the induced velocity signature at the time when the vortex is located at $r/D = 1$, would be the same as given by the red line in figure 3.8. On the other hand, if the vortex spacing is so small such that when the leading vortex passes $r/D = 1$, two other vortices are trailing in close proximity (with relative spacing similar to the high-frequency case of the model), substantial broadening of the induced velocity is seen due to the effect of the trailing vortices. This should influence the wall pressure in the same way, clarifying the influence of frequency on the time series in figure 3.6.

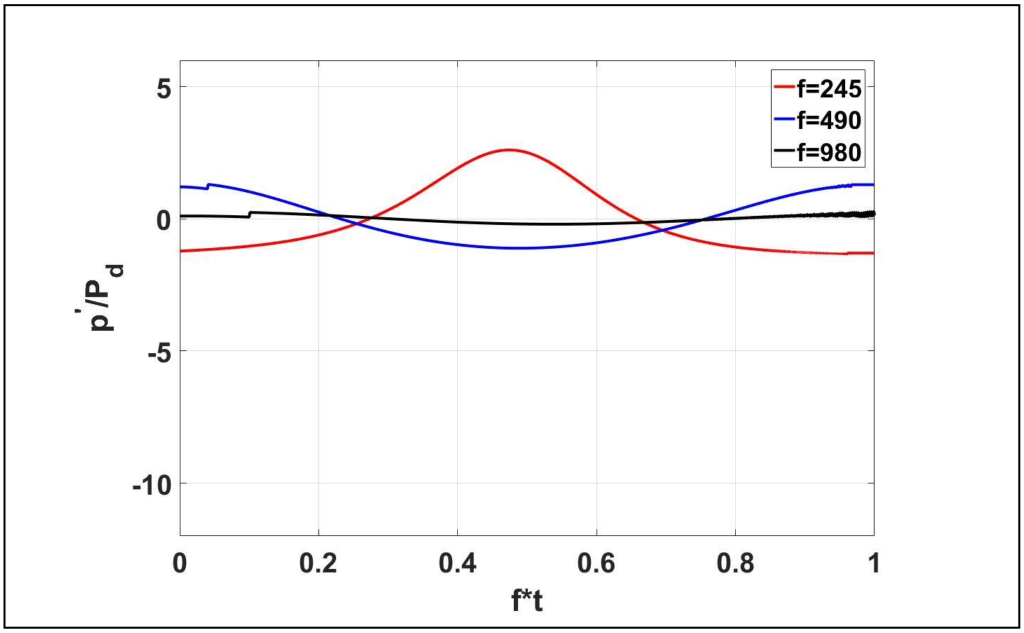

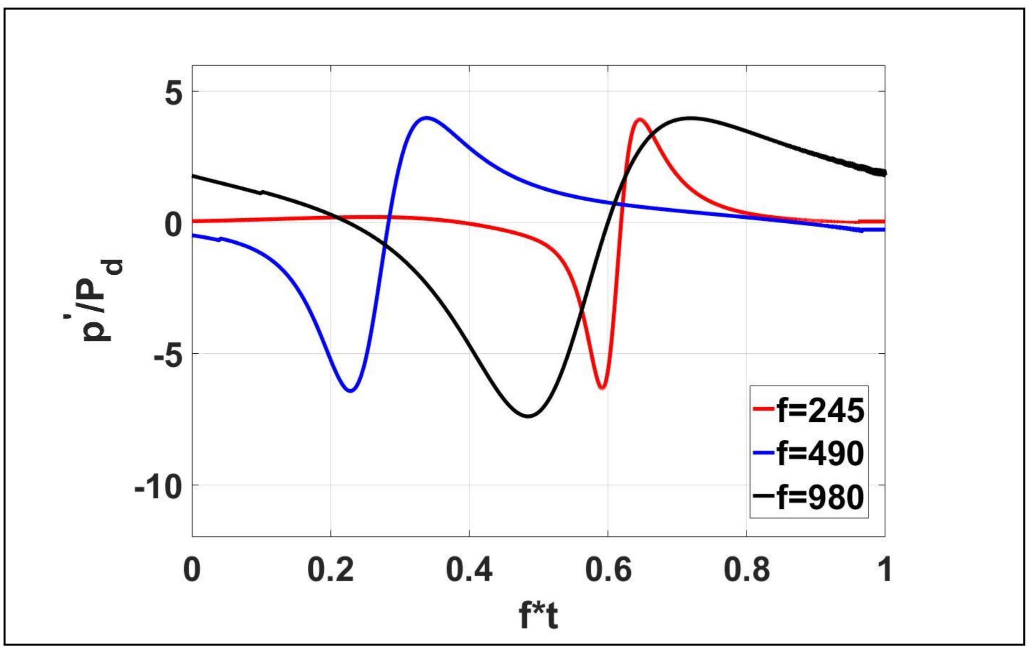

Figure 3.6 Pressure time series at various frequencies, Re=5000, $\Gamma = 0.1798\,\mathrm{m}^2/s$, and $r/D_o = 0(top)\ and\ r/D_o = 1\ (Bottom)$. The small discontinuities in the time series for the two larger frequencies correspond to the time instant when a new vortex is injected at the top of the computational domain. Because the discontinuities are small, no attempt was made to get rid of them by using a larger wall-normal extent for the computational domain.

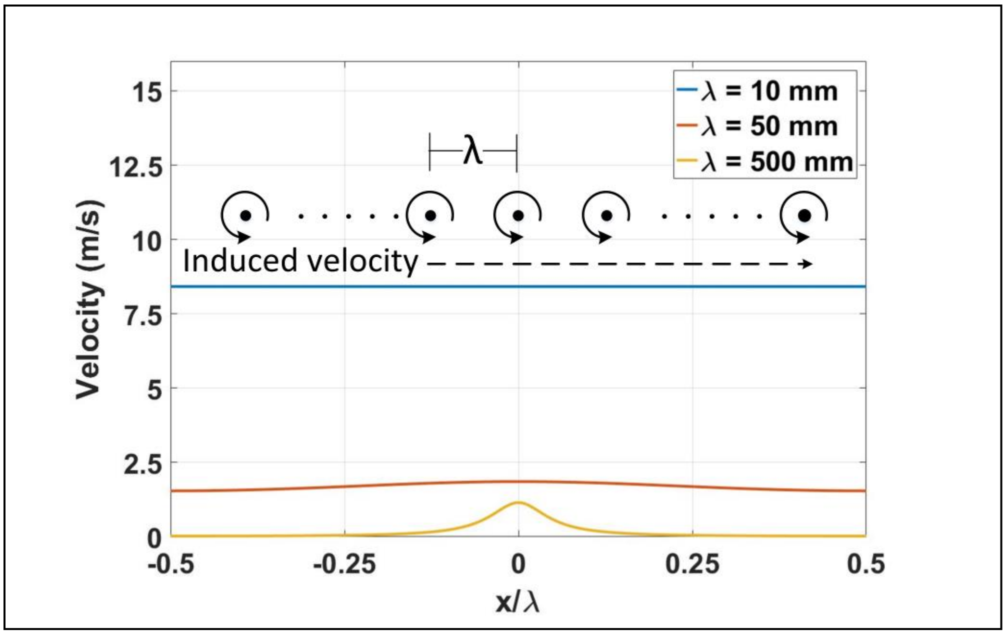

Figure 3.7 Induced velocity by an infinite line-vortex array along a line parallel to the array. Results are shown over one vortex spacing (λ) with the vortex located at the center ($x = 0$). Different colors indicate different spacing (i.e. different vortex packing density).

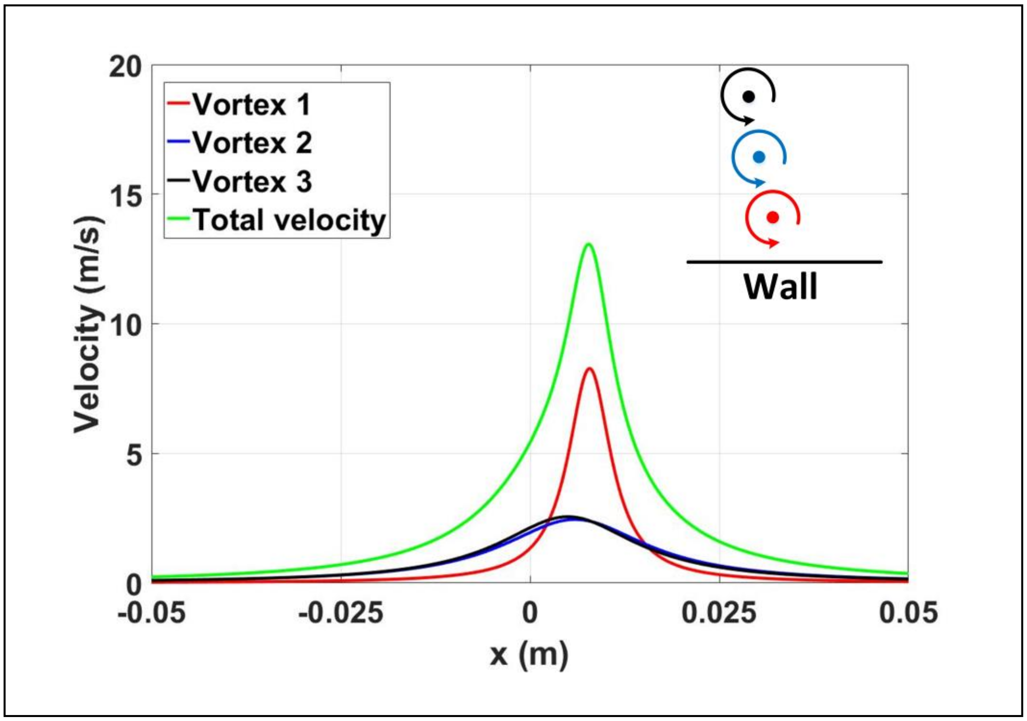

Figure 3.8 Individual and collective induced wall velocity by three-line vortices placed relative to a wall at the same locations as those from the present model's high-frequency case when the leading vortex is located at $r/D = 1$.

3.2 Reynolds Number Effect

Figure 3.9 and 3.10 show the radial distribution for the *mean* and *RMS* wall pressure when the jet Reynolds number is varied. Since the velocity scale is defined as that based on the stagnation (advection) flow at the top of the computational domain, increasing Re_D corresponds to increasing the strength/velocity of the stagnation flow. In addition, because the model is inviscid, essentially the interpretation of "Reynolds number" in this case is increasing the characteristic velocity of the jet relative to that induced by the vortices since all vortex parameters remain unvaried.

Figure 3.9 shows that the stagnation-point (*SP*) flow C_p does not vary with Reynolds number. This is expected given the normalization by a velocity scale based on the stagnation flow. In contrast, the overall C_p exhibits a deviation from C_p of *SP* flow that decreases with increasing

Re_D. This should not be too surprising given that the deviation is produced by the streaming flow induced by the vortices, which should remain invariant since the vortex characteristics are unchanged between Reynolds numbers. This invariance when normalized with an increasing dynamic pressure causes the deviation from *SP* mean pressure to decrease with increasing Re_D. Similarly, the decrease of the *RMS* pressure coefficient with Reynolds number (figure 3.10) can be attributed to an invariance in the unsteady pressure from vortex passage that produces smaller coefficient of pressure when normalized by the increasing dynamic pressure of the "jet".

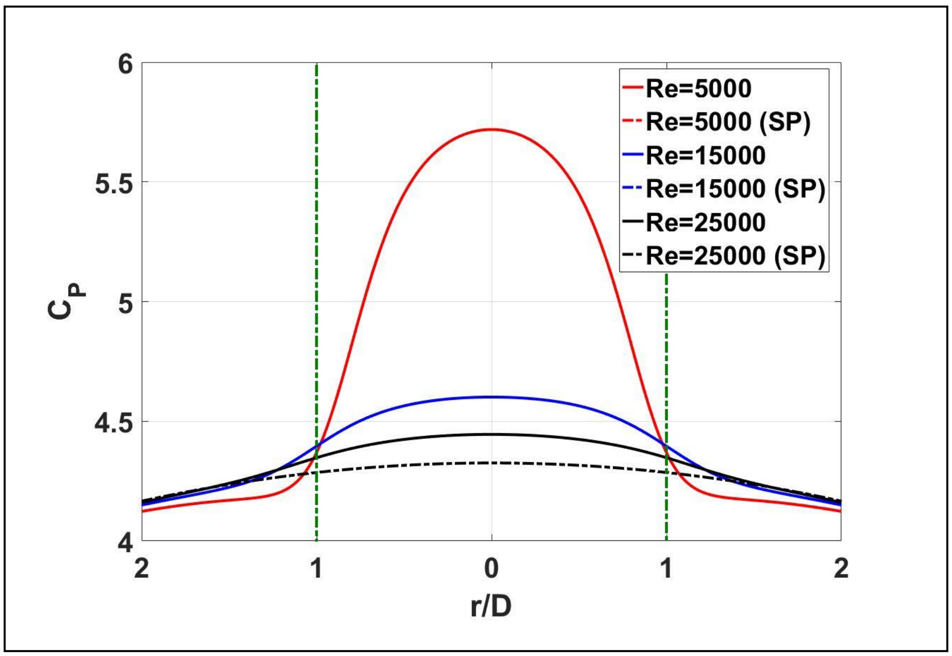

Figure 3.9 Effect of Reynolds number on the radial distribution of the mean pressure coefficient

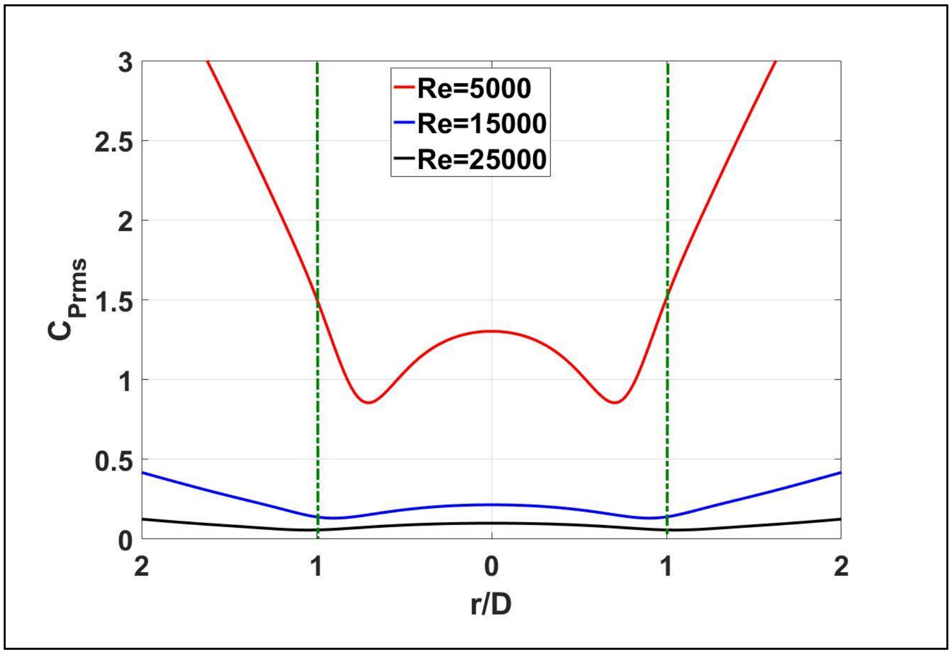

Figure 3.10 Effect of Reynolds number on the radial distribution of the *RMS* pressure coefficient

3.3 Circulation Effect

Figures 3.11 and 3.12 depict the *mean* and *RMS* pressure distributions for various vortex circulation magnitudes (i.e. vortex strengths). The case with the intermediate circulation value is the reference case (the same as the $f \approx 245\text{Hz}$ in section 3.1), where one vortex at a time is affecting the wall pressure. The other two cases are similar with the exception of the vortex strength, which is weaker in one case and stronger in the other.

The overall features of the mean pressure profile stay the same with varying circulation strength. Quantitatively, the stagnation pressure increases, and a local minimum develops with increasing circulation. The same trends were observed to take place with increasing frequency in section 3.1. In that case, these changes were attributed to the increase in induced velocity due to the increasing number of vortices with increasing frequency. Here, the effect is similar but since the number of vortices does not change (the frequency is the same for all three cases), the induced velocity increases due to circulation.

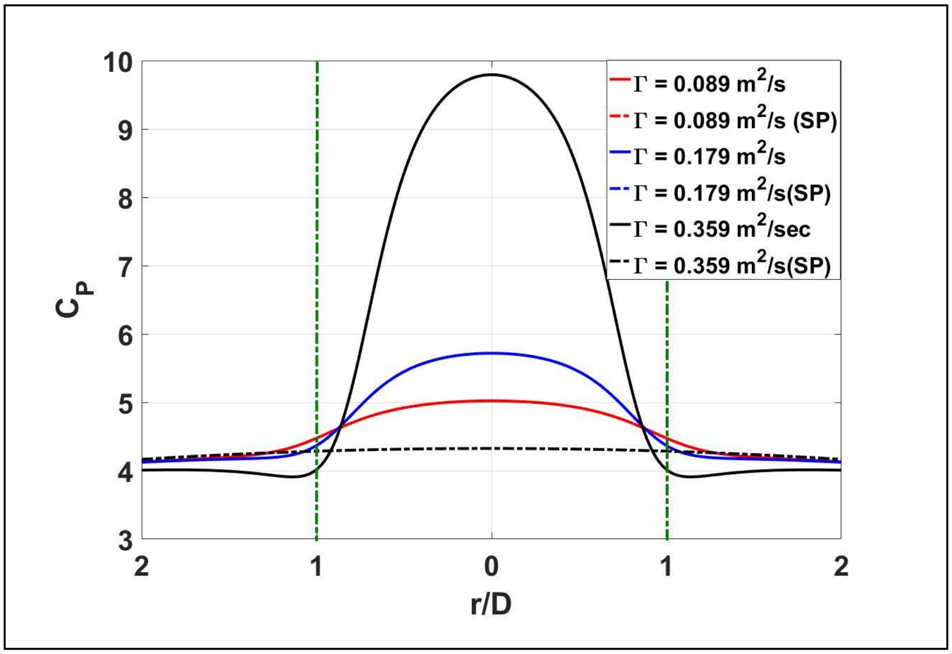

Figure 3.11 Effect of vortex circulation on the radial distribution of the mean pressure coefficient

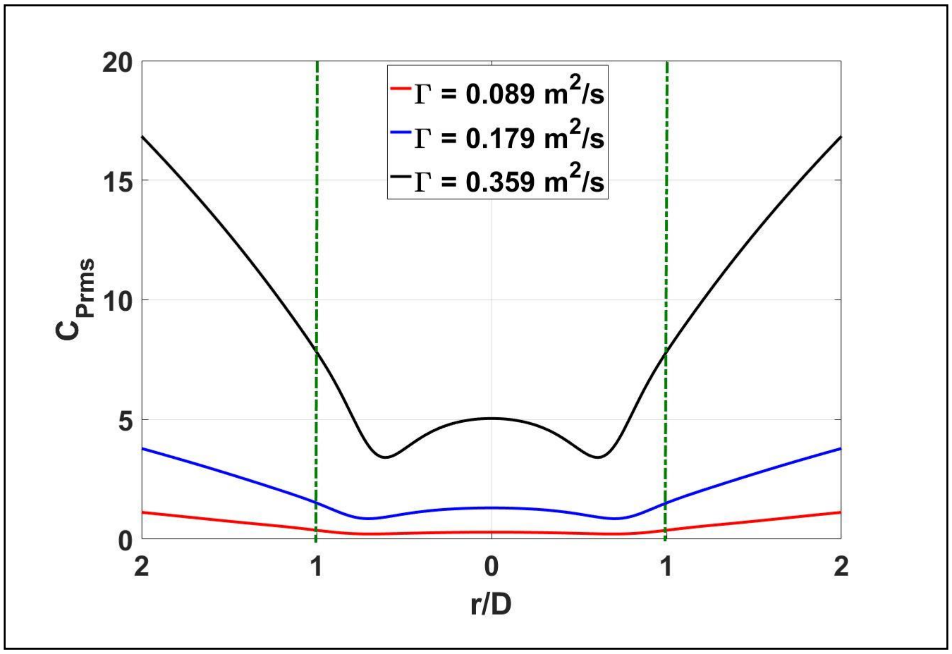

Figure 3.12 Effect of vortex circulation on the radial distribution of the *RMS* pressure coefficient

In regard to the *RMS* distribution (figure 3.12), the overall shape remains invariant with changing circulation (consult figure 3.4 to see the details of the reference case/intermediate circulation more clearly) but the *RMS* level increases monotonically with increasing circulation (consistent with the stronger vortices). Overall, the pressure signal shapes within the stagnation zone remain similar with increasing circulation, while the magnitude of the pressure peaks increases (leading to the larger *RMS* level). This may be seen by comparing figure 3.13 for the highest-circulation case to the top plot in figure 3.5 for the reference case. A more direct comparison between the time series shapes of the lowest and highest circulation cases at the stagnation point and end of the stagnation zone is given in figure 3.14. The results clearly demonstrate the increasing strength of the pressure fluctuations without change in the pressure signal shapes.

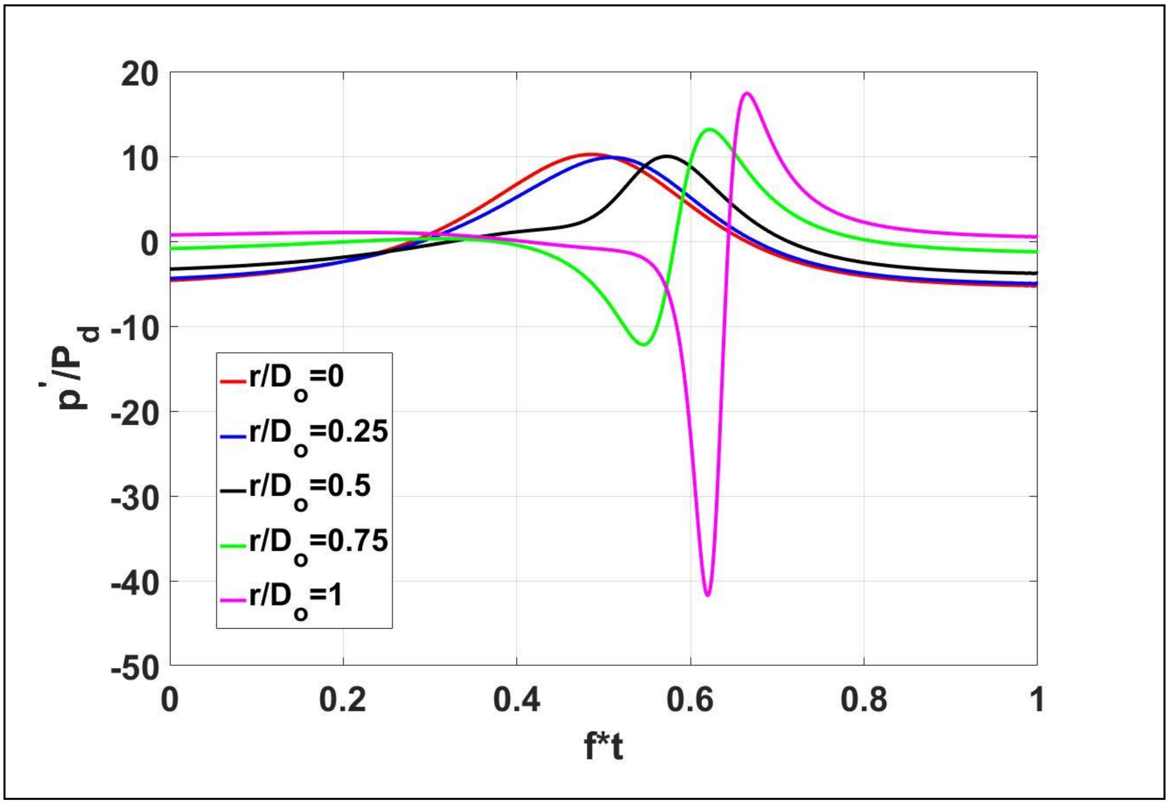

Figure 3.13 Pressure time series at various *r/D* locations within the stagnation zone, *Re*=5000,

$\Gamma = 0.359\ \mathrm{m^2}/s$, and $f \approx 245$ Hz

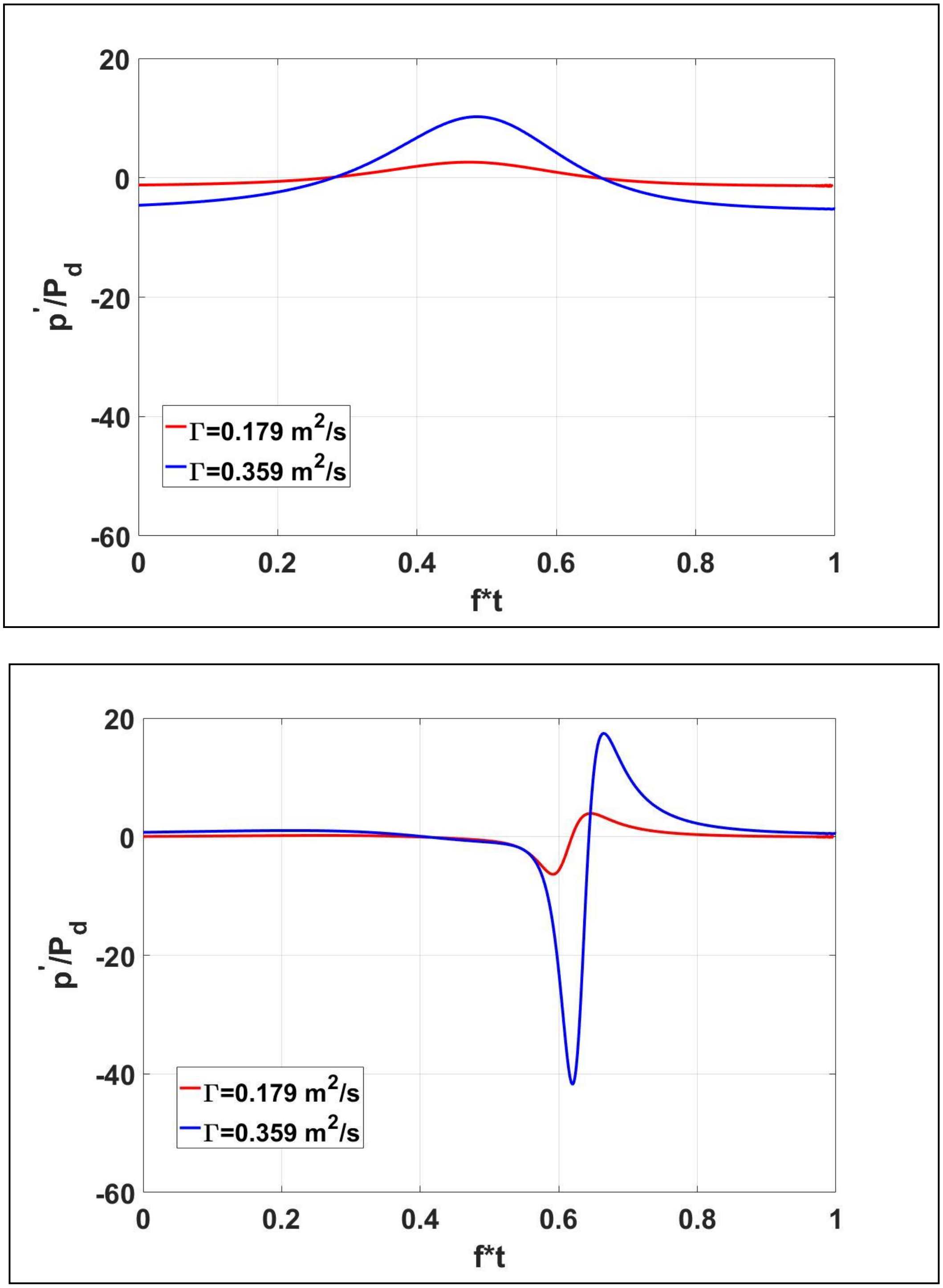

Figure 3.14 Pressure time series for various vortex circulations, *Re*=5000, $f \approx 245$ Hz, and $r/D_o = 0 (top)\ and\ r/D_o = 1\ (Bottom)$.

CHAPTER 4: Experiment Setup and Apparatus

This chapter exhibits the experimental setup that was used to measure the unsteady wall pressure and the initial jet velocity profiles. The coordinate system and the configuration of the flow utilized in the experiment will be described. The measurement techniques and procedures used to measure the velocity and the fluctuating pressure will be demonstrated. Moreover, the stepper motor and 2D traversing system used to traverse the hot-wire velocity probe over the measurement domain, the hardware and software used to collect experimental data, and the assembly of the experimental components will be explained.

4.1 Coordinate System and Flow Configuration

This research is focused on the normal incidence impinging jet flow. The flow configuration is depicted in figure 4.1. Two coordinate systems are used. The first system is (X, Y, Z) cartesian system with origin at the jet exit centerline, and the second is a polar system (r, θ, z) originating at the center of the impingement plate and at (shown in figure 4.1 for the plane $\theta = 0$).

The impinging jet facility used in the current experiments resides in the Flow Physics and Control Laboratory at Michigan State University. The facility underwent a major renovation and subsequent characterization by Al-Aweni [7]. The jet discharges through a round exit with diameter $D = 25\text{mm}$, at the end of a contoured nozzle, resulting in an initial condition of a top-hat velocity profile. The flow from the jet impinges on a circular flat plate with diameter $12D$. The disc diameter is greater than the jet diameter by an order of magnitude to reduce the effect of the edge of the disc on the flow. The mean flow does not change in the θ direction and it is assumed to be axisymmetric (as verified in Al-Aweni [7]), and the distance between the jet exit and the impingement plate H is adjustable.

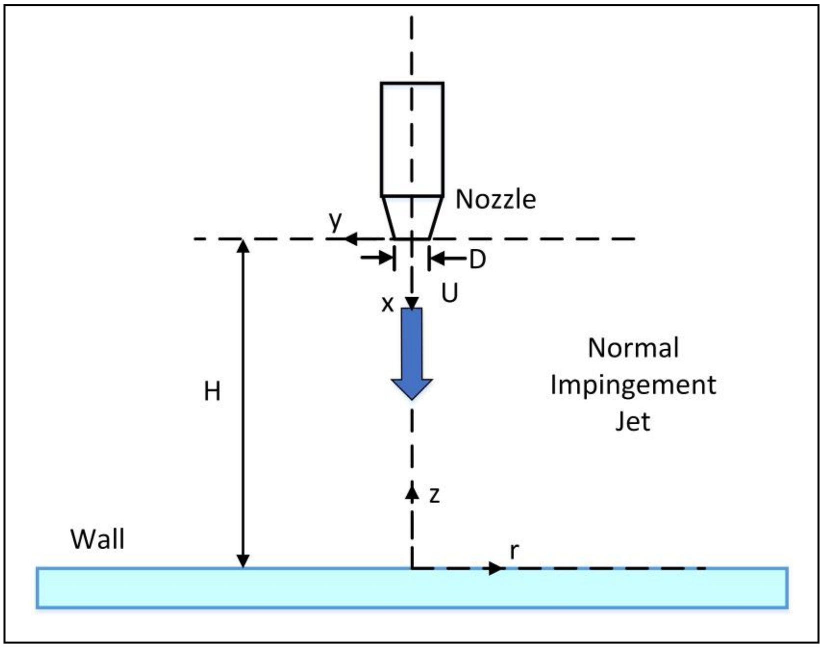

Figure 4.1 Flow configuration for normal-incidence impingement jet

4.2 Experiment General Assembly

The experimental facility is presented in figure 4.2, and it consists of a centrifugal blower, type Dayton 4C108, driven by $^3/_4$ HP *DC* motor. The flow rate through the facility is adjusted by changing the speed of the motor. The blower provides provide air to the jet through a *PVC* pipe with a of diameter 7.7 cm. The exit pipe diameter of the blower is smaller than, and it does not touch the inner diameter of the *PVC* pipe to reduce the vibration effect from the blower.

The air passes into a flow conditioning chamber with dimensions $30.5 \text{ cm} \times 30.5 \text{ cm} \times 76.2 \text{ cm}$, before entering a nozzle with an area contraction ratio of 80, to decrease the turbulence intensity. The turbulence intensity was measured at the nozzle exit using a hot-wire anemometer, and was found to be less than 1% for the jet velocity of 5 m/s (based on the streamwise velocity fluctuations)

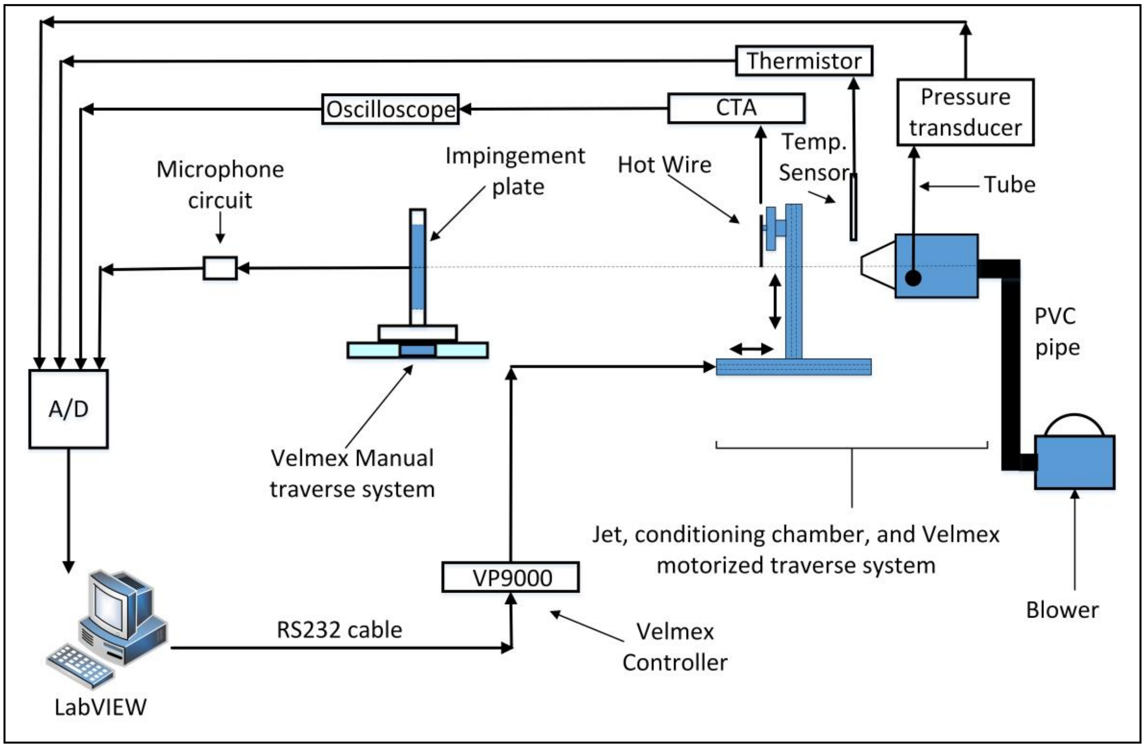

Figure 4.2 Experimental facility

Referring to figure 4.3, the impingement disc is embedded flush in a vertical square plate with dimensions of $45.8 \text{ cm} \times 45.8 \text{ cm}$. The circular disc is fitted with 30 microphones for measuring the unsteady wall pressure, including eight microphones, employed in the current work, that are arranged as a line array along the radial direction (see section 4.4 for more details). The square plate is placed on a sliding table that can be moved in the *x*-direction using a manual traverse system (as shown in figure 4.3), model Velmex A1506P40-S1.5-TL, which allows to change the distance between the impingement plate and the nozzle exit (*H*). The Velmex traverse system can move total distance of 115 mm with an accuracy of 0.0254 mm.

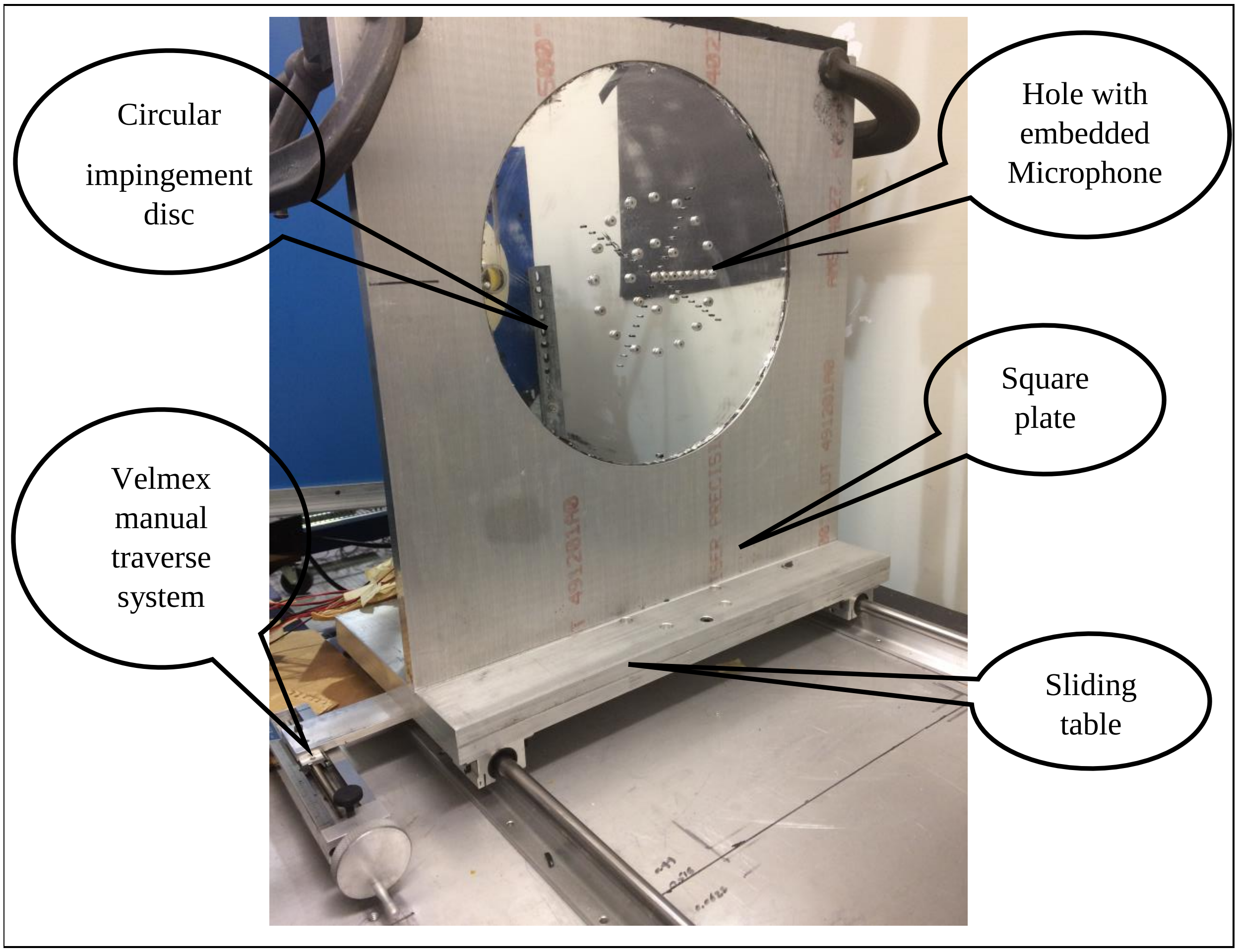

Figure 4.3 An image of the impingement plate and the sliding table attached to the Velmex manual traverse system

A steel frame is used to hold the conditioning chamber, the nozzle, and the impingement plate. The frame is mounted on a table different from the one utilized to support the blower to isolate the facility from the vibration generated by the blower.

In the course of this study, a stepper-motor-driven Velmex traversing system was added to the facility. The system was used to traverse a single hot-wire probe to characterize the jet velocity profiles near the nozzle exit (i.e. the initial condition). The hot-wire was attached to the carriage of the Velmex system via a custom-made arm (see figure 4.4 and 4.5). The traverse system has three-degrees of freedom (*DOF*): two-linear and one rotational (models MB4027K2J-56 and

B4872TS respectively). Only the linear *DOF* are used in the present work to move the velocity probe in *X* and *Y* directions. The traverse system is controlled by Velmex controller, type *VP9000*, with the ability to control the system manually through a joystick, or programmatically through an *RS-232* interface with a desktop *PC* computer.

The jet mean exit velocity was determined from measurement of the difference between the stagnation pressure in the setting chamber and the ambient pressure (further details are given in section 4.3). Data acquisition was accomplished using National Instruments NI PCI-6024E *PC*-based analog to digital (*A/D*) converter card. The *A/D* card was coupled with National Instruments BNC2080 analog breakout board to facilitate signal connections via coaxial BNC cables. The card has 12-*bit* resolution and input range that is changeable between $\pm 50\ mV$ to $\pm 10\ V$, and it can sample up to 16 single-ended multiplexed channels at a maximum rate of $200\mathrm{kHz}$ using LabVIEW version 8.2.

4.3 Hot-wire Setup and Calibration

A single hot-wire probe was used to measure the streamwise velocity profile of the jet near the exit of the nozzle. Figures 4.4 and 4.5 depict a schematic of the hot-wire setup used during calibration and measurements, and an image showing the motorized traverse system respectively.

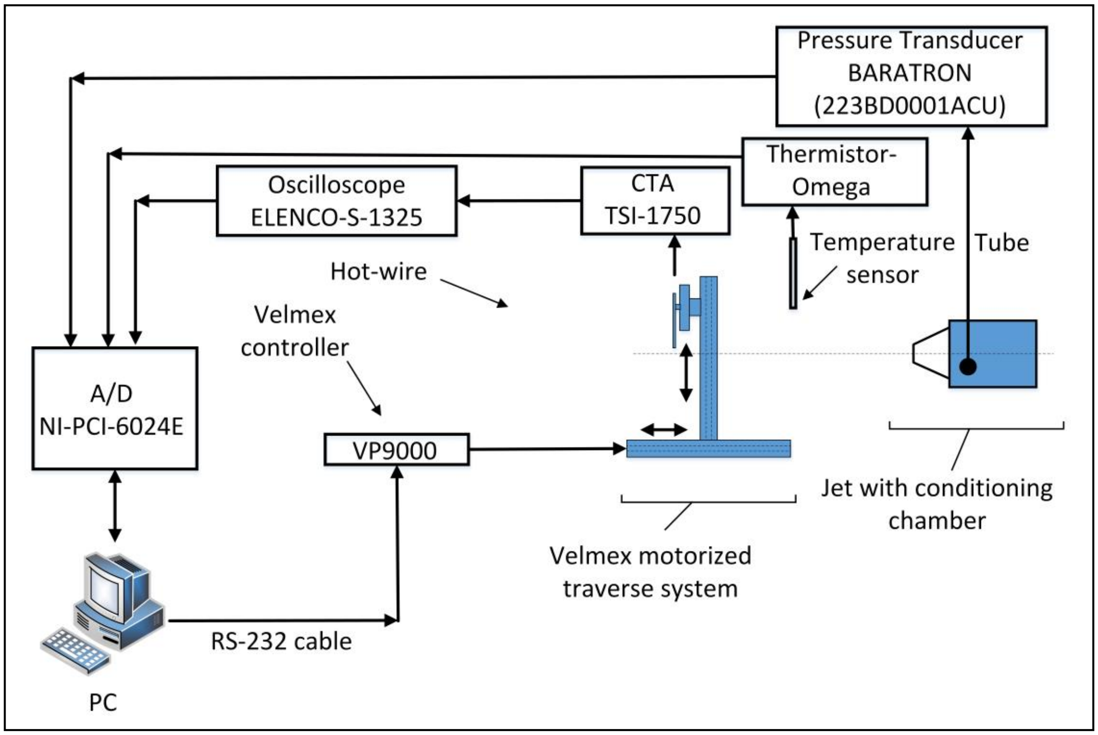

Figure 4.4 Block diagram of the setup used for calibration and measurements of the hot-wire

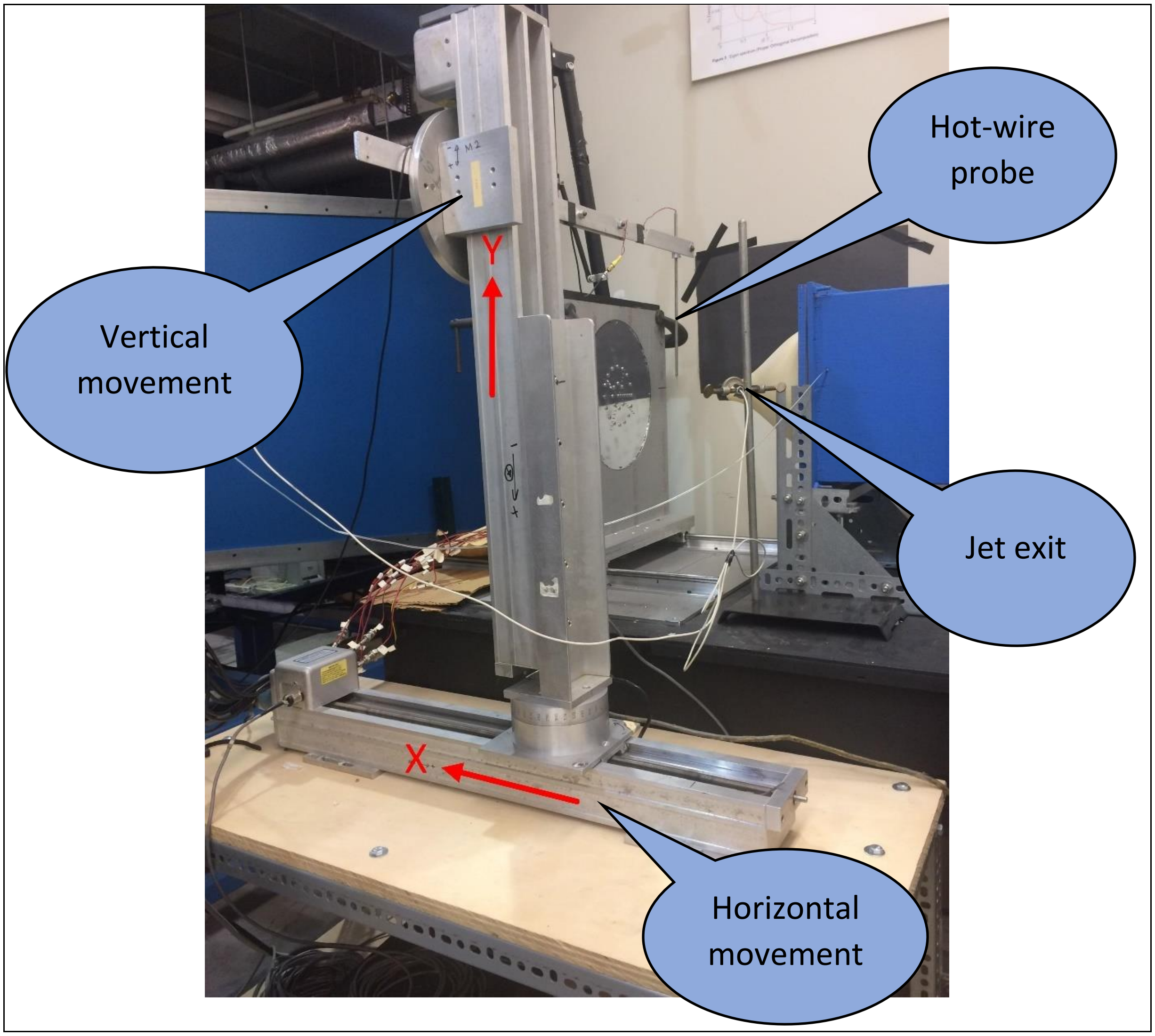

Figure 4.5 An image of the motorized system for traversing the hot wire

The hot wire was built using tungsten with a sensing length and diameter of 1 mm and 5μm respectively, which provide a length to dimeter ratio of 200. The wire was used to measure the mean and the fluctuating streamwise velocity while operated using a Constant Temperature Anemometer (CTA), model TSI 1750, at an overheat ratio $r_h = 0.6$, defined as:

$$r_h = \frac{R_w}{R_a} - 1 \tag{4.1}$$

Where, R_w represents the operating (heated) hot-wire resistance, and R_a the hot-wire resistance at room temperature. The overheat ratio can be as high as 1 but it is generally kept between 0.6-0.8. The higher the value, the better the velocity sensitivity and the smaller the temperature sensitivity. Too high of a value, however, could cause oxidation, and hence drift in the response of the wire.

The bandwidth cut-off frequency f_c of the hot-wire was found using the following equation

$$f_c = \frac{1}{1.3\tau} \tag{4.2}$$

Where, τ represents a response time, which was obtained from a square wave test. Figures 4.6 and 4.7 depict the diagram for the square wave test and the result respectively. During the test, $0 - 10$ mV square wave with frequency of 5 kHz was fed from Agilent WAVETEK function generator to the square wave input of the *CTA*. The output of the *CTA* was captured on a Tektronix TDS 1002B digital oscilloscope, as shown in figure 4.7. the figure also demonstrates how τ was determined to be 25µs yielding a bandwidth of 30.7kHz.

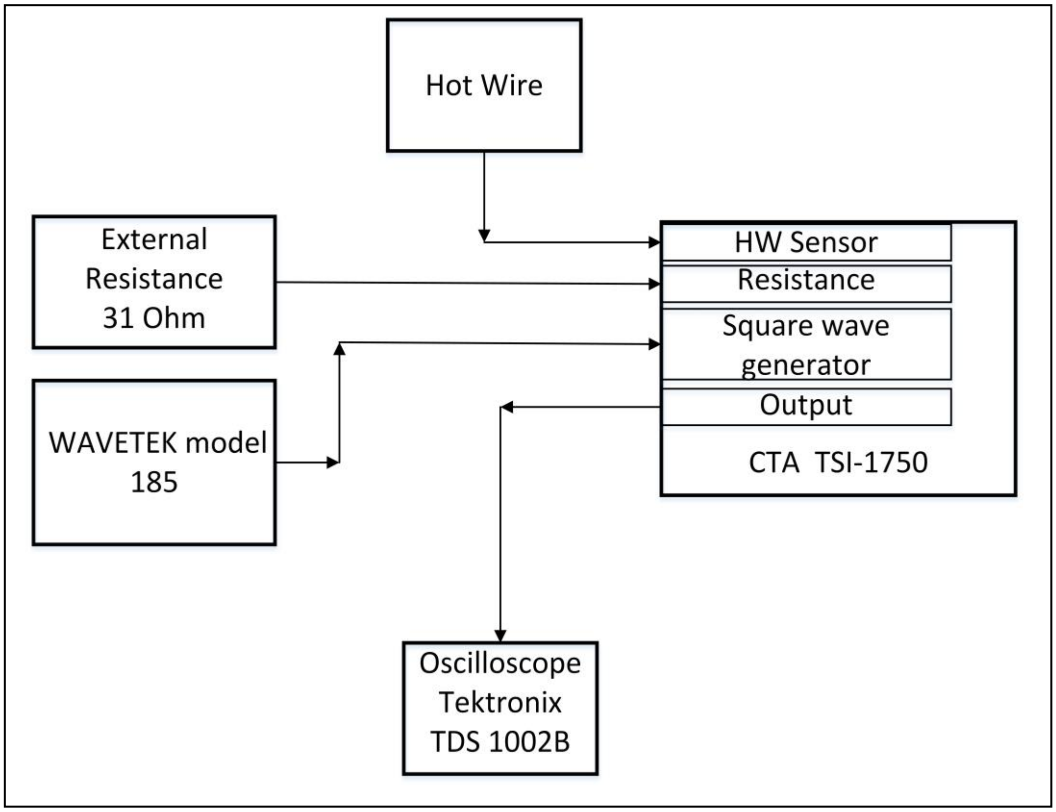

Figure 4.6 Block diagram of the setup for the square wave test

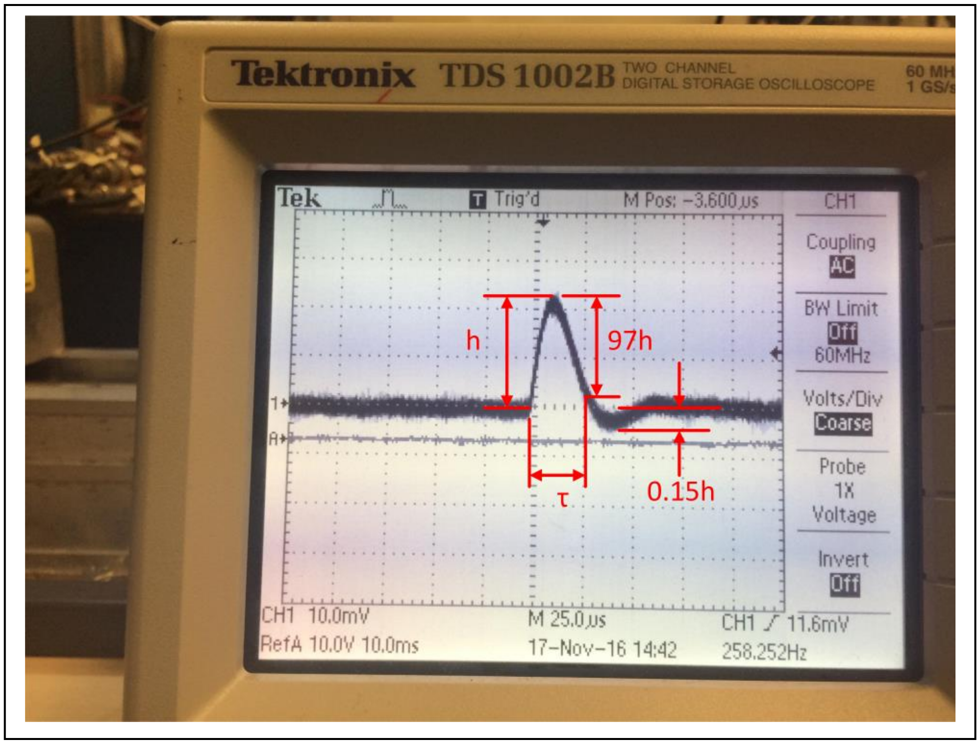

Figure 4.7 An image of the oscilloscope screen showing a typical square wave test result

The hot-wire was calibrated in-situ by placing the wire near the center of the jet within the potential core where the jet velocity can be obtained from the difference between the stagnation and the ambient pressure. This pressure difference was measured using either high a (10 torr) or a low (1 torr) pressure transducer Baratron model 223BD-00010ACU or 223BD-00001ACU respectively. The pressure transducers have sensitivity of 0.75 mV/Pa and 7.5 mV/Pa respectively. The positive-input side of the pressure transducer was connected via Tygon tubing to a pressure tap in the wall of the setting chamber, just upstream of the nozzle. The other, low pressure, side of the pressure transducer was left open to ambient pressure. Temperature of the air flow was measured sing a thermistor, type Omega DP-25-TH, with a sensitivity of $100\,\mathrm{mV/C^{\circ}}$. The measured temperature was used to correct the hot-wire output for the variation of the flow temperature from that of the calibration. Figure 4.8 depicts an image of the hot-wire, temperature sensor, stagnation pressure tap, nozzle, impingement plate, and the setting chamber.

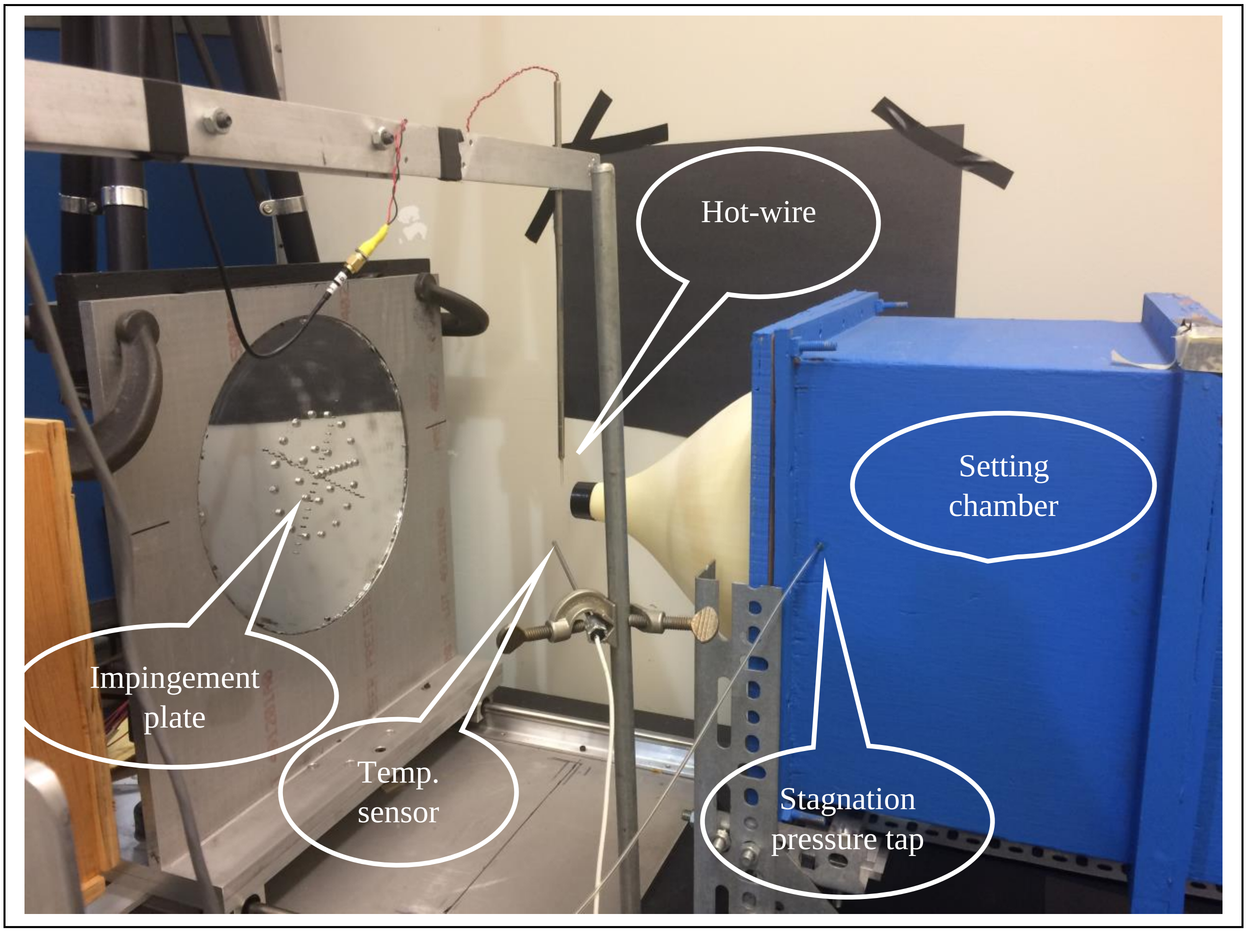

Figure 4.8 An image of the hot-wire, temperature sensor, nozzle, impingement plate, and the conditioning box

To acquire the pressure, the temperature, and the hot-wire signal, a LabVIEW program was developed for this purpose. Typically, the signals were acquired for eight different velocities depending on the velocity range in the experiments which varied between 5 to 15 m/s. All hot-wire voltages were corrected for the variation of the temperature during the period of calibration using

$$E_c = E_m \left[\frac{T_w - T_{cal}}{T_w - T_m}\right]^{1/2} \tag{4.3}$$

Where, E_c represents the corrected hot-wire voltage, E_m the measured hot-wire voltage, T_w The hot-wire temperature calculated using equation (4.4) below, T_m the flow temperature measured during the acquisition of data, T_{cal} the average temperature during the calibration process. The hot-wire temperature (T_w) was found using

$$r_h = \alpha(T_w - T_a) \tag{4.4}$$

Where, α represents the resistance-temperature coefficient (for tungsten 0.0045 $°C^{-1}$), and T_a is the ambient temperature.

For the calibration, the jet velocity U_j was found using Bernoulli's equation

$$\rho = \frac{p_{atm}}{RT_a} \tag{4.5}$$

$$U_j = \frac{1}{\sqrt{1 - \left(\frac{A_j}{A_s}\right)^2}} * \sqrt{\frac{2\Delta p}{\rho}} \approx \sqrt{\frac{2\Delta p}{\rho}} = \sqrt{\frac{2(p_o - p_{atm})}{\rho}} \tag{4.6}$$

Where, ρ is the air density, p_{atm} the atmospheric pressure, R the ideal gas constant for air ($0.287 \, \frac{\text{kj}}{\text{kg.k}}$), T_a the ambient air temperature, measured using the temperature sensor, and p_o is the stagnation pressure in the settling chamber, measured using the pressure transducer. Note that A_j/A_s is one over the contraction area ratio (1/80), which is neglected in the above calculation.

The data pairs of the jet velocity and the corrected voltage of the hot-wire sensor were fitted with equation (4.7), which represents King's Law, by using the method of least-squares:

$$E^2 = A + B * U^n \tag{4.7}$$

Where, E represents the corrected voltage of the hot-wire, U the measured velocity using the pressure transducer, and n (typically in the range n = 0.4 to 0.45), $A \; and \; B$ are the equation constants found using the least-squares method.

The calibration was done before and after the experiments. Figure 4.9 depicts a sample of typical calibrations after and before the experiments, which agree within a maximum difference of 0.8 %.

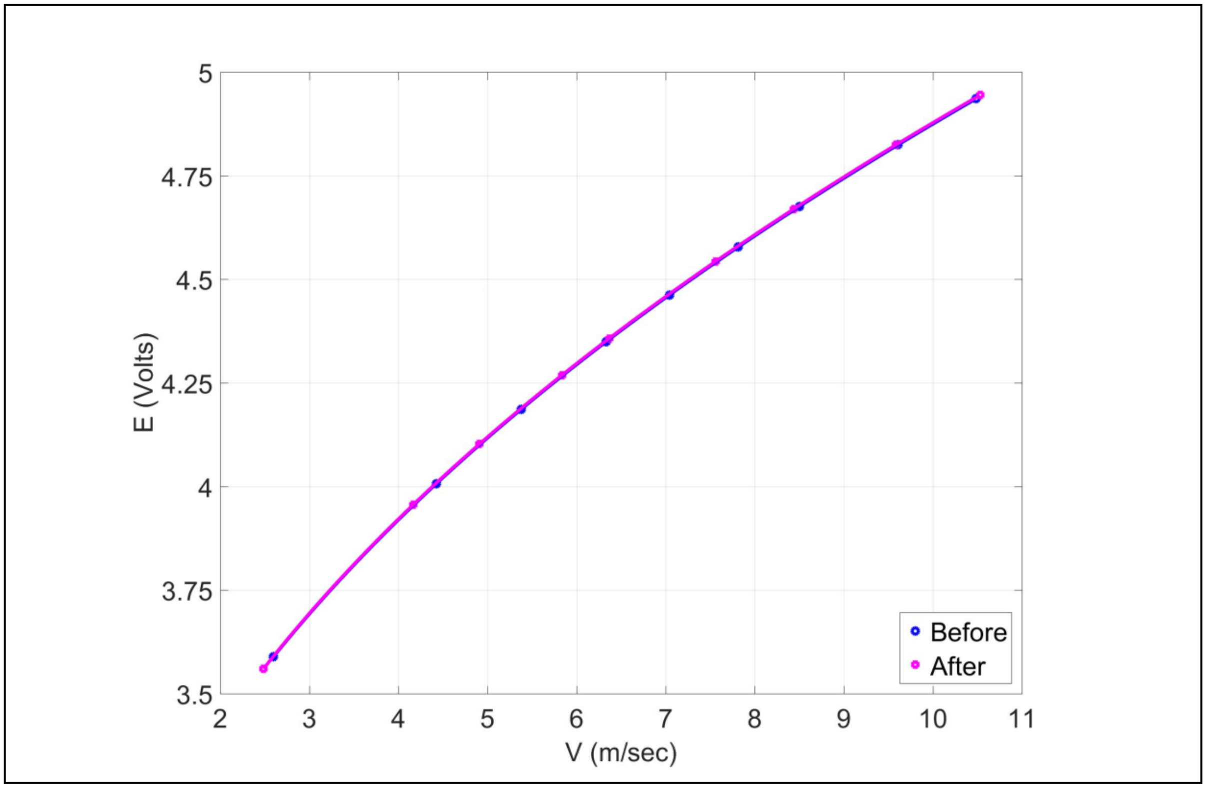

Figure 4.9 Sample of hot-wire calibrations before and after an experiment

4.4 Microphone Setup and Calibration

The fluctuating pressure was measured using eight electret Panasonic WM-61A microphones embedded in the impingement plate, as shown in figure 4.10. The microphones' sensing hole and package diameter are 2 mm (0.08*D*) and 6 mm (0.24*D*) respectively. The microphones have a flat frequency response between 20-20,000 Hz and a typical manufacturer-provided sensitivity of $-35 \mp 4dB$ @ 1kHz (corresponding to 11.22 to 28.18 mV/Pa,) with *DC* supply voltage in the range 2V and 10V. The eight-microphone array was arranged starting from the center of the disc (*r/D*=0) along the radial direction with a spacing of 0.33*D* between the centers of each successive microphones. Figure 4.10 depicts the configuration of the microphones on the impingement plate. The microphones were connected to a homemade 16-channel microphone circuit powered by 9 *DC* volts to provide power to the microphone and connect the microphone to the NI-6024E board.

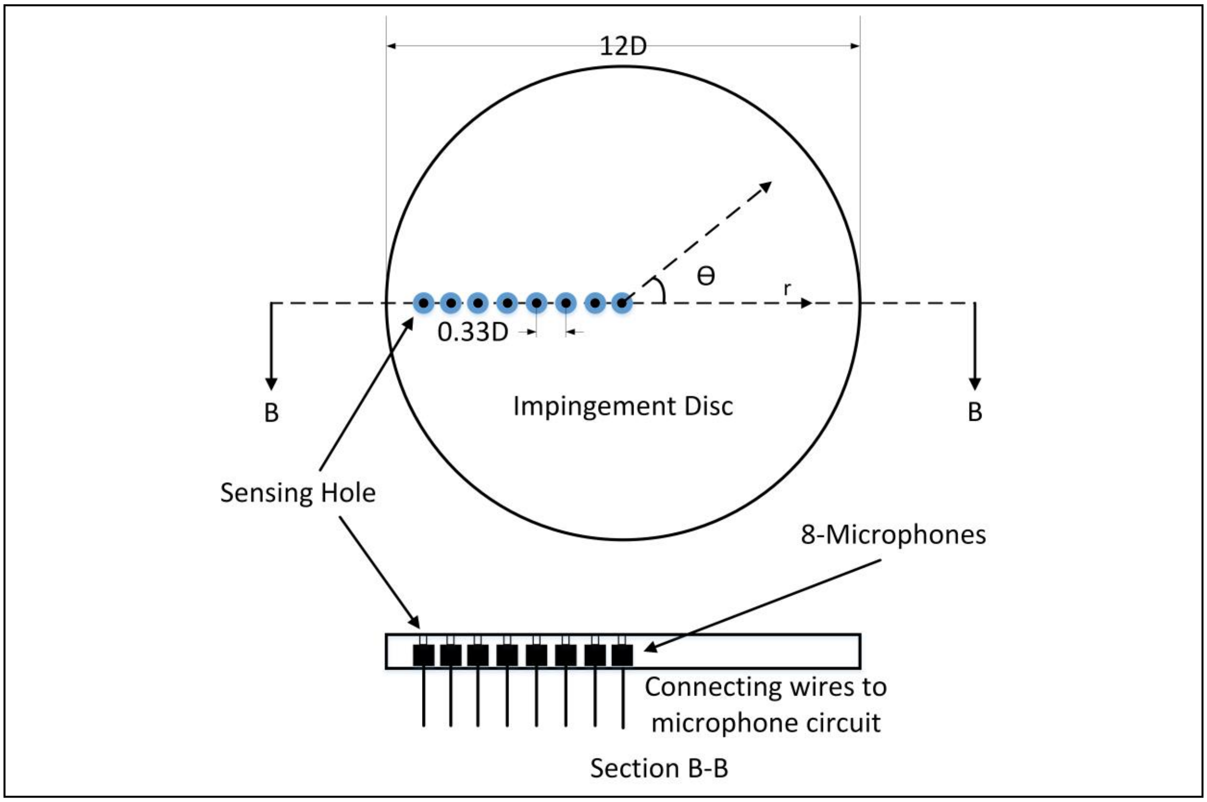

Figure 4.10 Front and cross section (B-B) view (top and bottom respectively) of the microphone array configuration used in the present work

Since the sensitivity of the microphones provided by the manufacturer is nominal, the individual microphones had to be calibrated before each experiment. This also accounts for possible change in sensitivity due to variation in temperature, humidity, dirt, and installation. The eight microphones were calibrated, one at a time by using a plane wave tube (*PWT*) and a reference microphone that has known sensitivity. The reference microphone used for the calibration was

Brüel and Kjær (*B&K*) ${}^{1}/_{4}{}''$ model 4923-A-001 with sensitivity of 1.424 mV/Pa at a polarization voltage of $200V$. The microphone has a bandwidth of $4 - 70000$ Hz.

The *PWT* was built by Al-Aweni [7] using a $12.7mm \times 12.7mm$ *PVC* square tube, which fastens to the impingement plate, by using two clamps, as shown in figures 4.11 and 4.12. The tube has eight holes for mounting the *B&K* microphone at the same radial locations of the Panasonic microphones. On the other hand, the wall of the tube that is in contact with the impingement plate was removed allowing the Panasonic micrphone array to be embedded in the *PWT*. Acoustic waves were generated in the tube using Agilent model HP-33120A function generator coupled to a Hafler-P1000 amplifier, which drives a Dayton model RS150S-8 audio speaker. The speaker was placed at one end of the plane wave tube, generating white noise acoustic waves in order to excite all frequencies of interest simultaneously inside the *PWT*.

According to [24], for example, if an acoustic wave with a wavelength $\lambda > 2l$ (corresponding to a frequency $f < {}^{c}/_{2l}$; where $l, f, and\ c$ represent the tube cross-section side length, the sound frequency, and the speed of sound respectively) propagates in a square solid duct, then the wave will remain planar at any given cross section. This means, the phase and the magnitude of pressure will remain constant over the cross section at the given plane. So, the reference microphone (*B&K*) and the microphone to be calibrated (Panasonic) will be exposed to the same pressure magnitude and phase because they are located at the same cross section.

During calibration, each microphone was calibrated individually by inserting the reference microphone into the *PWT* at the same cross section of the Panasonic microphone. One hundred records, each having 4096 point data points sampled at 50 kHz, were acquired from two *A/D* channels, to which the microphones were connected. Applying the analysis shown in Al-Aweni

[7], the acquired data produced the magnitude and phase response of the Panasonic microphones; as exemplified in figure 4.13.

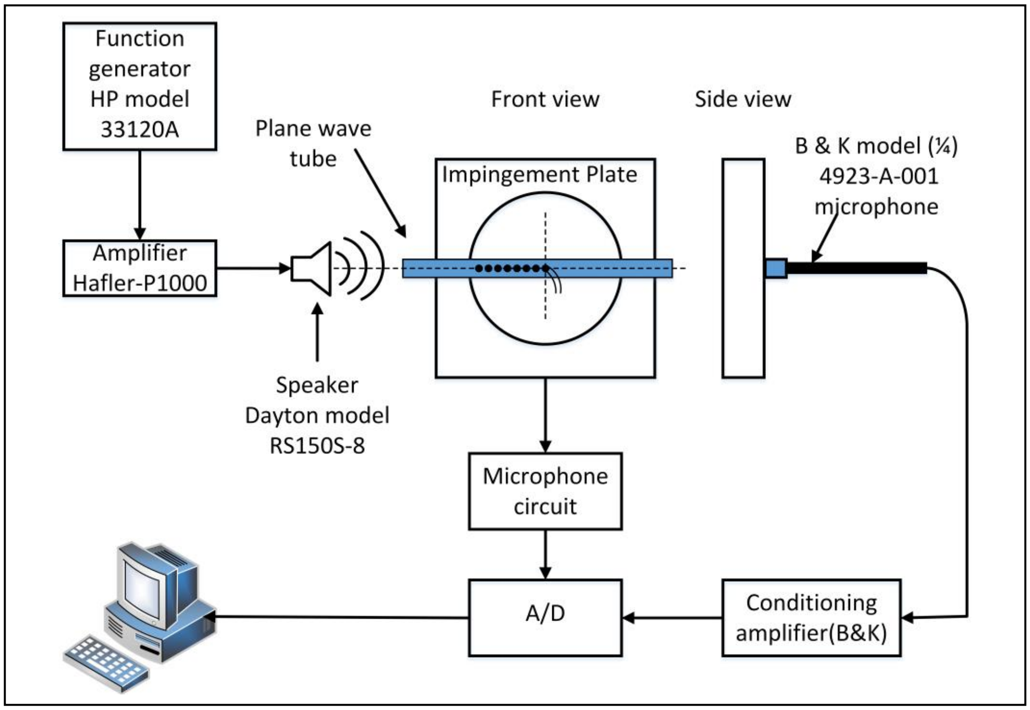

Figure 4.11 Block diagram of the calibration setup for the microphone array

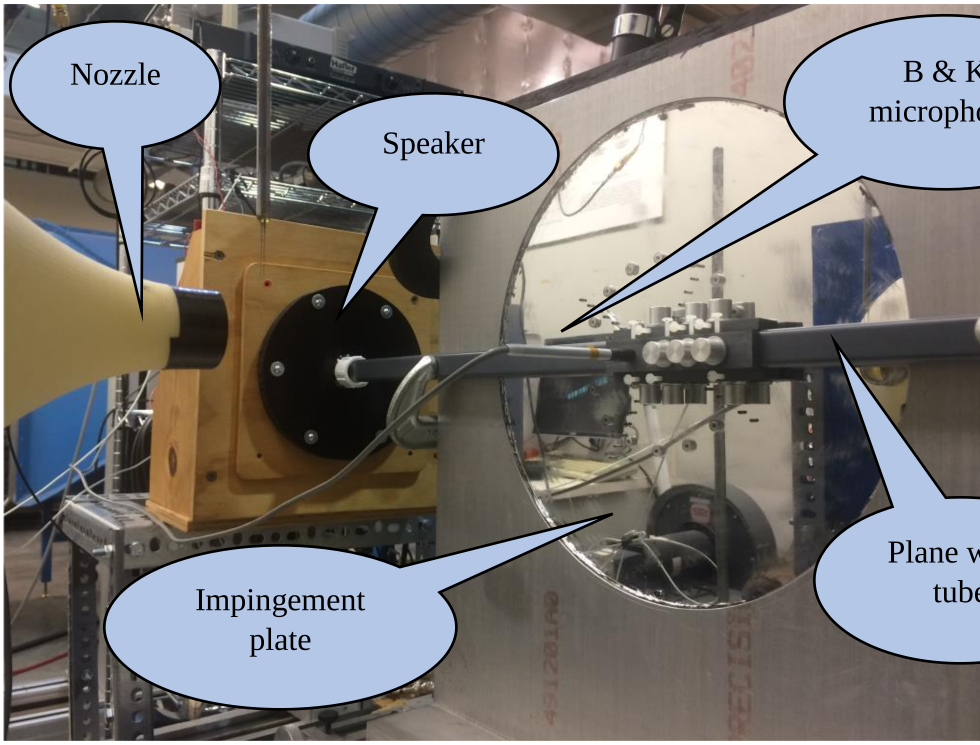

Figure 4.12 An image of the calibration setup for the microphone array

Table 4.1 shows a sample of the eight microphones' sensitivities, where microphone 1 is located at the stagnation point and microphone 8 is placed at the end of the measurement domain.

The values given, which fall within the manufacturer-reported nominal range, are found by averaging the magnitude response over the frequency range 100-5000 Hz.

Microphone	1	2	3	4	5	6	7	8
Sensitivity mV/Pa	18.625	18.447	23.789	19.623	18.837	22.652	25.666	25.624

Table 4.1 Sample of the microphones' sensitivity obtained from calibration.

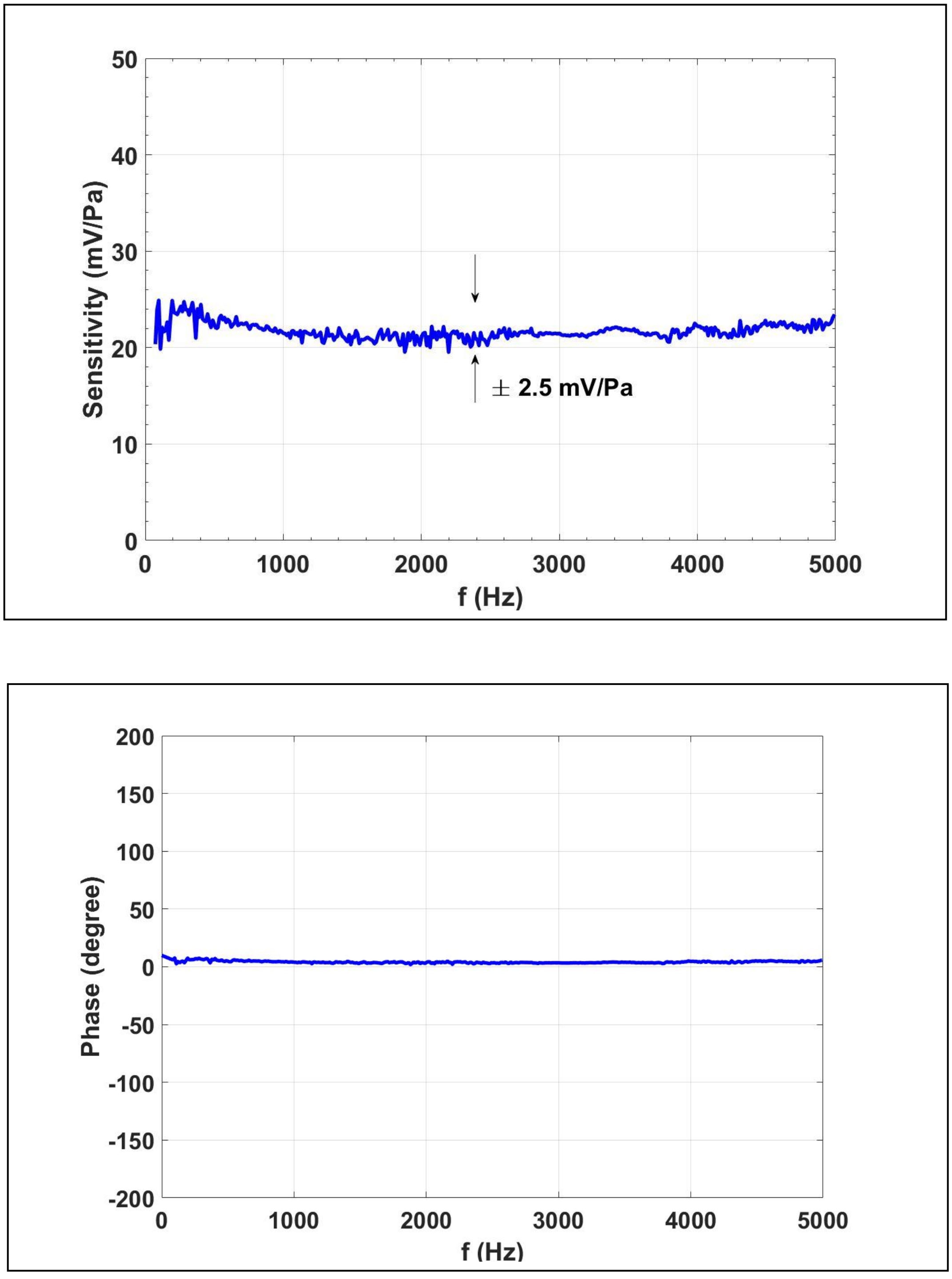

Figure 4.13 A sample of the microphone calibration results: sensitivity (top) and phase (bottom)

4.5 Procedure to Acquire Velocity Profile

After calibration, the hot-wire was placed near to the edge of the shear layer. The latter was found approximately by monitoring the hot-wire signal on an oscilloscope as the wire was traversed across the shear layer. Once the edge of the shear layer was found, the wire was traversed to 50 to 100 different positions (with a resolution of 5μm), depending on the *X* location, such that measurements were conducted across the entire shear layer. The movement and the data acquisition were automated using a LabView program. At each location, time series containing 409600 data points of jet velocity, jet temperature, and hot-wire signal were acquired at 5000 samples/second. The duration of the acquisition T_{acq} is such that almost 5000 vortices travel across the measurement point at the lowest frequency of vortex passage (*St* = 0.3 and the lowest velocity of $U_j = 5$ m/s). The sampling rate is also selected to be much larger than any frequency of interest ($St_{acq} = 6.35$, based on the highest velocity).

4.6 Procedure to Acquire the Microphone Signals

After calibration of the microphones, the PWT was removed and the impingement plate was fixed at a desired distance (*H/D*). Before acquiring the microphone signals, the mean jet velocity was fixed to provide the desired Reynolds number. Once the jet reached steady state, 800 data records containing 512-point per record were acquired at a rate of 5000 samples/s from all microphones in the array using a LabVIEW program.

CHAPTER 5: Jet Characteristics and Wall-Pressure Measurements

Before investigating the pressure measurements, it is important to demonstrate the jet characteristics as it emerges from the nozzle; i.e. the initial condition. This chapter will explore the characteristics of the jet and the wall-pressure measurements. The jet characteristics were found by measuring the streamwise flow velocity component using a single hot wire, traversed across the shear layer at a few streamwise locations. The data were used to demonstrate the self-similarity of the jet's initial shear layer; in agreement with the literature. The pressure measurements from this study were compared with previous studies using different statistical quantities, including power spectra, root mean square of the pressure fluctuation, probability density functions (*pdf*), skewness, and kurtosis.

5.1 Initial Shear Layer Self-Similarity

It is important to examine the characteristics of the shear layer and the initial flow conditions. To achieve this goal, the mean and fluctuating streamwise velocity were measured, and the data were used to obtain the corresponding cross-stream velocity profiles across the shear layer. For these measurements, the hot-wire was initially moved using relatively large steps, with a resolution of 0.5 mm/step, in the transverse direction and the wire output signal was monitored on the oscilloscope to approximately locate the edges of the shear layer. Subsequently, the movement resolution was refined gradually to verify the location of the edges of the shear layer. Once the edges were found, the probe was controlled to traverse across the whole shear layer with even higher resolution (0.01 mm/step) to properly resolve the high-shear zone within the shear layer. The data were recorded at Reynolds numbers of 8272, 165454, and 33090 which represented velocities of 5 m/s, 10 m/s, and 20 m/s, respectively. Profiles were obtained at three different streamwise locations (*X/D*= 0.2, 0.4, and 0.8). The self-similarity of the profiles obtained at different Reynolds numbers was verified using normalized mean and fluctuating velocity plots, as shown in figures 5.1 and 5.2 respectively. For these plots, the origin of the cross-stream coordinate is taken at the shear layer centerline; defined as the *y* location where the mean velocity is half of the jet exit velocity. The y coordinate is normalized by the momentum thickness (θ), which is found using

$$\theta = \int_{y_{U=0.1U_j}}^{y_{U=U_j}} \frac{U(y)}{U_j} \left(1 - \frac{U(y)}{U_j}\right) dy \qquad (5.1)$$

Where $U(y)$ is the mean streamwise velocity profile, and U_j is the jet exit velocity. To minimize the error resulting from hot-wire data near the shear layer outer edge, where reverse velocity may occur due to the energetic shear-layer vortices, the momentum thickness was calculated by truncating the integration limit to the location where $U(y)$ is 10% of the jet velocity; i.e. the lower integral limit in equation 5.1 $(y_{U=0.1U_j})$. As seen from figures 5.1 and 5.2, the velocity profiles for the various Reynolds numbers at the same streamwise location (*X/D*=0.2) collapse well. The collapse of the velocity profiles demonstrates the initial self-similarity of the jet.

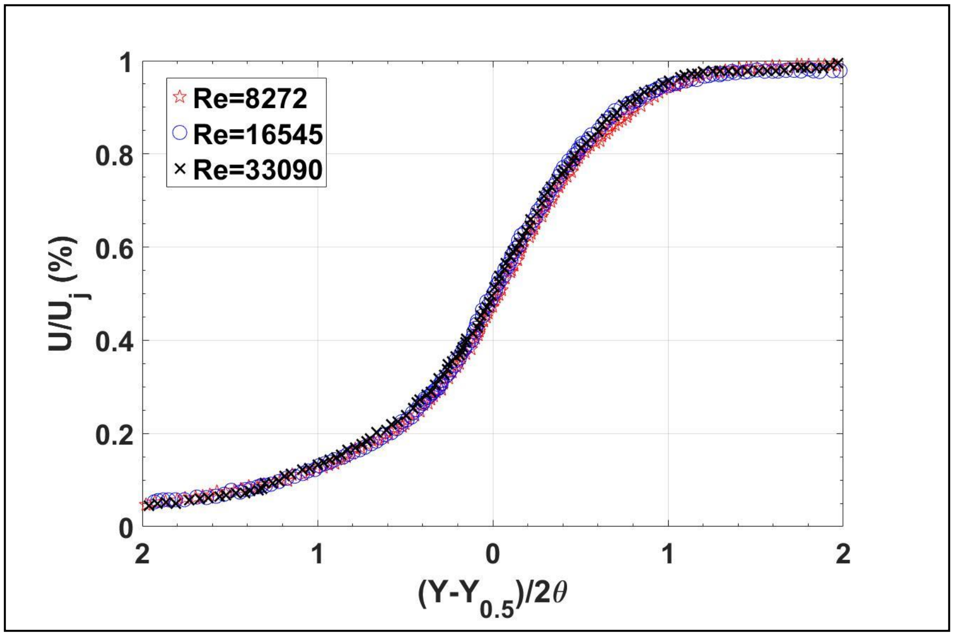

Figure 5.1 Shear-layer mean velocity profile at *X/D*=0.2 for various Reynolds numbers

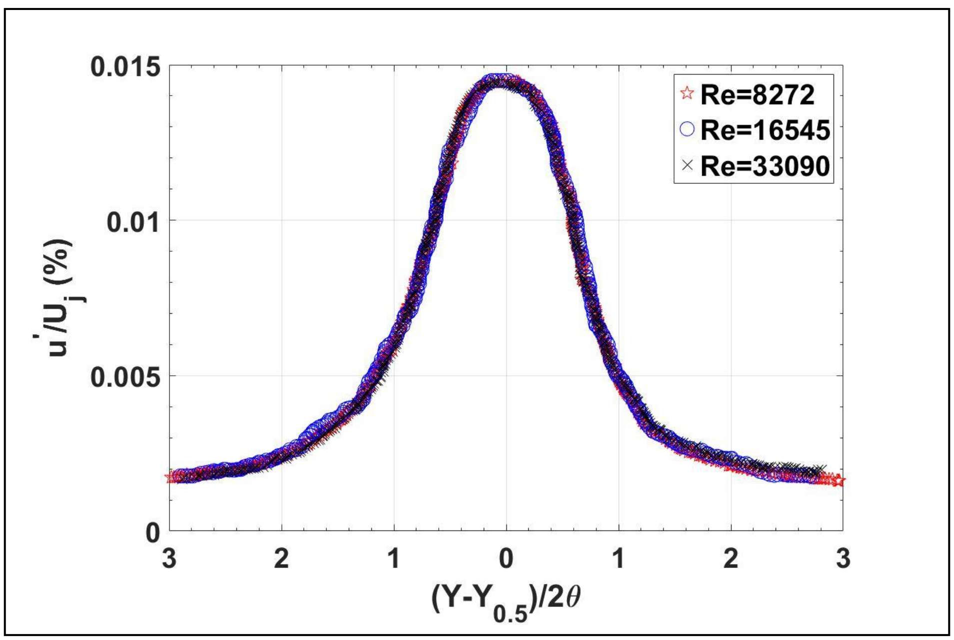

Figure 5.2 Shear-layer fluctuating-velocity root-mean-square profile at *X/D*=0.2 for various Reynolds numbers

To check the self-similarity at different *X/D* locations, mean and fluctuating-velocity profiles of the shear layer were measured at three streamwise locations (*X/D*= 0.2, 0.4, and 0.8) for Reynolds number of 8272. The results are depicted in figures 5.3 and 5.4 respectively, which demonstrate that the velocity profiles collapse for the distance *X/D*=0.2-0.8, further confirming self-similarity.

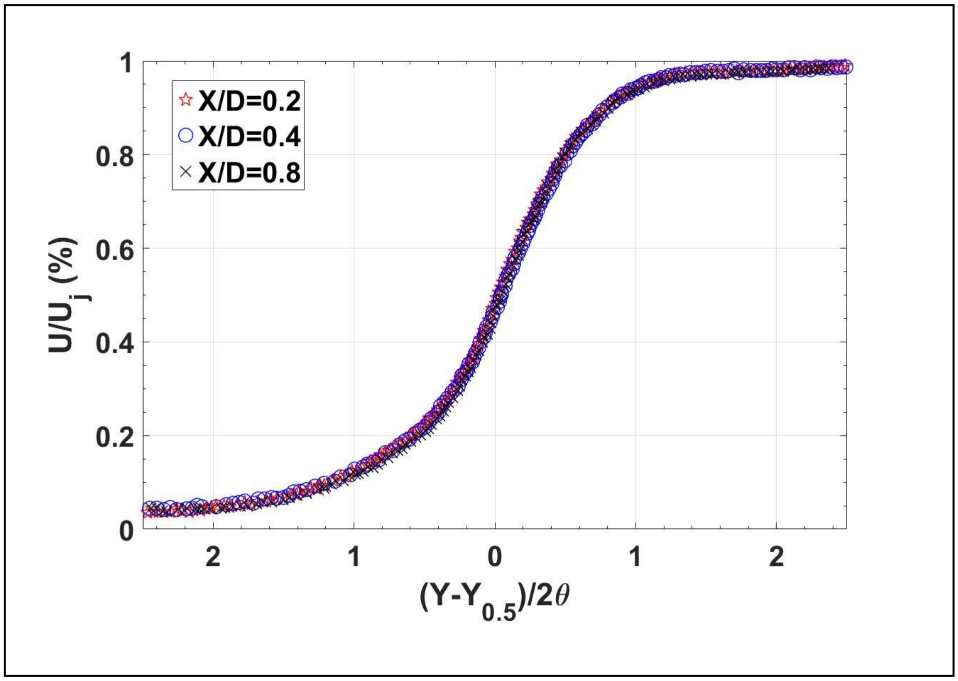

Figure 5.3 Shear-layer mean velocity profile at various *X/D* locations and $Re_D = 8272$

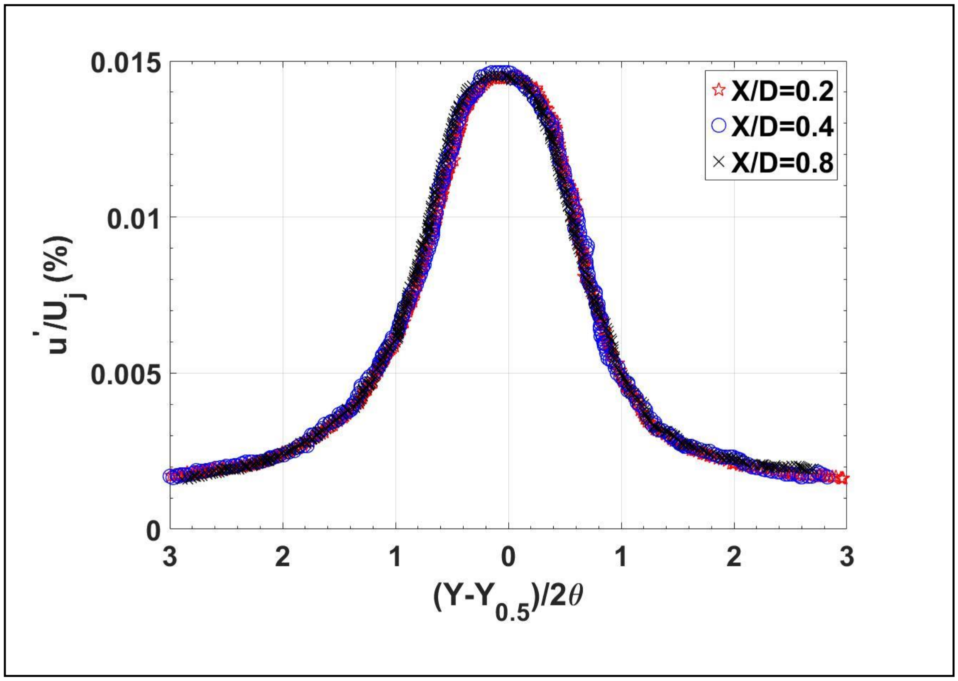

Figure 5.4 Shear-layer fluctuating-velocity root-mean-square profile at various *X/D* locations and

$Re_D = 8272$

5.2 The Root Mean Square of the Fluctuating Pressure

The root mean square pressure is calculated from the pressure time series using

$$p_{rms} = \sqrt{\frac{\sum_{i=1}^{n}(p_{\mathrm{i}} - P)^2}{n}} \tag{5.2}$$

Where, p_i is the instantaneous pressure, P is the mean pressure, *i* indicates the time index, or sample number in the digitized pressure time series, and *n* is the total number of samples in the time series. The number of samples is 409600 samples with a sampling frequency of 5000 *samples/sec*. Note that since microphones are used for measuring the pressure, they are incapable of capturing P. However, the measured time series typically have a small offset voltage error, necessitating removal of the mean “pressure”, as given by equation 5.2.

Figure 5.5.a depicts the radial distribution of the root mean square results for the pressure fluctuation (p_{rms}) for Reynolds number 8272. The fluctuating-pressure *RMS* value is normalized by the dynamic pressure ($P_d = {}^1\!/_2\, \rho U_j^2$) and the radial location (*r*) is normalized by the jet dimeter (*D*). Results are shown for different *H/D* values, represented by different colors. The results show that, though the overall shape of the root mean square pressure distribution is similar for all *H/D* values, the p_{rms} magnitude depends on *H/D*. A peak is noticed for all three *H/D* = 2, 3 and 4 cases at *r/D* ≈ 1.33. The magnitude of this peak, and p_{rms} in the *wall-jet zone* in general, decreases with increase in *H/D*. Also, the location of the maximum p_{rms} seems to shift towards smaller *r/D* with increase in *H/D*, as implied from the "flattening" of the peak. The precise location of the maximum cannot be determined with the present measurement resolution.

On the other hand, within the *stagnation zone*, the trend with *H/D* is reversed, where the magnitude of the root mean square pressure increases, rather than decreases, with increasing *H/D*. For example, the magnitude of p_{rms} at the stagnation point (*r/D* = 0) increases to 54% of the maximum for *H/D*=4, in contrast to 14% at *H/D*=2. Also noteworthy, for all *H/D* values, the normalized p_{rms} drops rapidly for the range $r/D > 1.33$ to a magnitude of around 5% by the end of the measurement domain.

Figure 5.5.b depicts $p_{rms}(r)$ for the higher Reynolds number of 24818. The distribution has the same behavior as for Re_D = 8272, except for *H/D*=4, where a second peak emerges within the stagnation zone, at *r/D*=0.67. Significantly, unlike all other cases, at the higher Reynolds number and *H/D* = 4, the maximum p_{rms} is found in the stagnation, instead of the wall-jet zone. The magnitude of p_{rms} at the stagnation point increases to 42% of the maximum for *H/D*=4, in contrast to 12% at *H/D*=2.

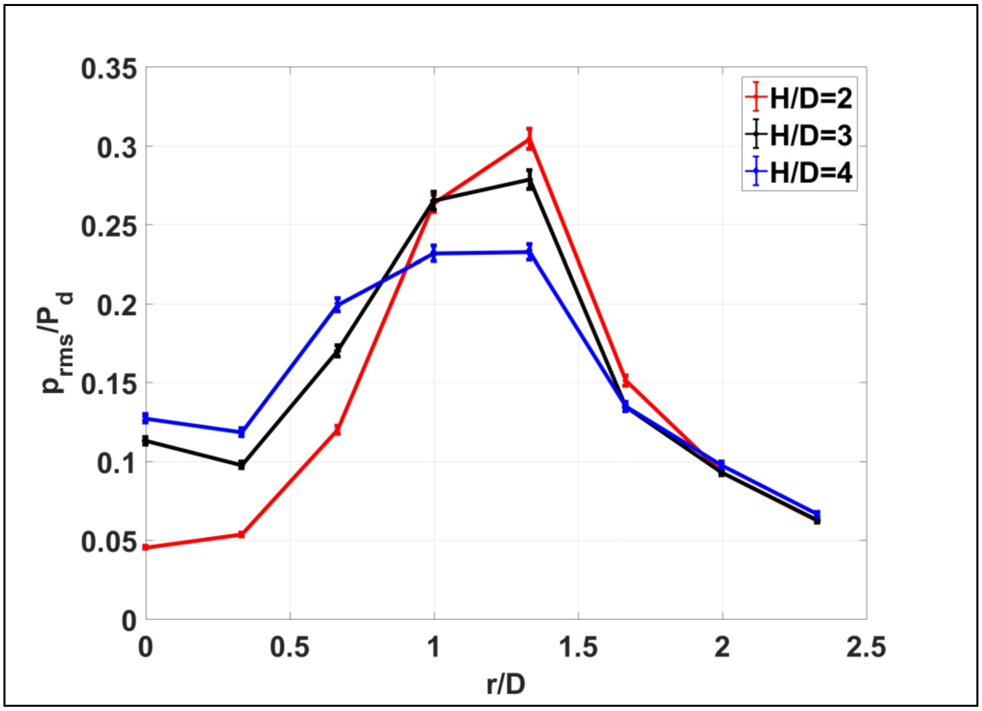

(a)

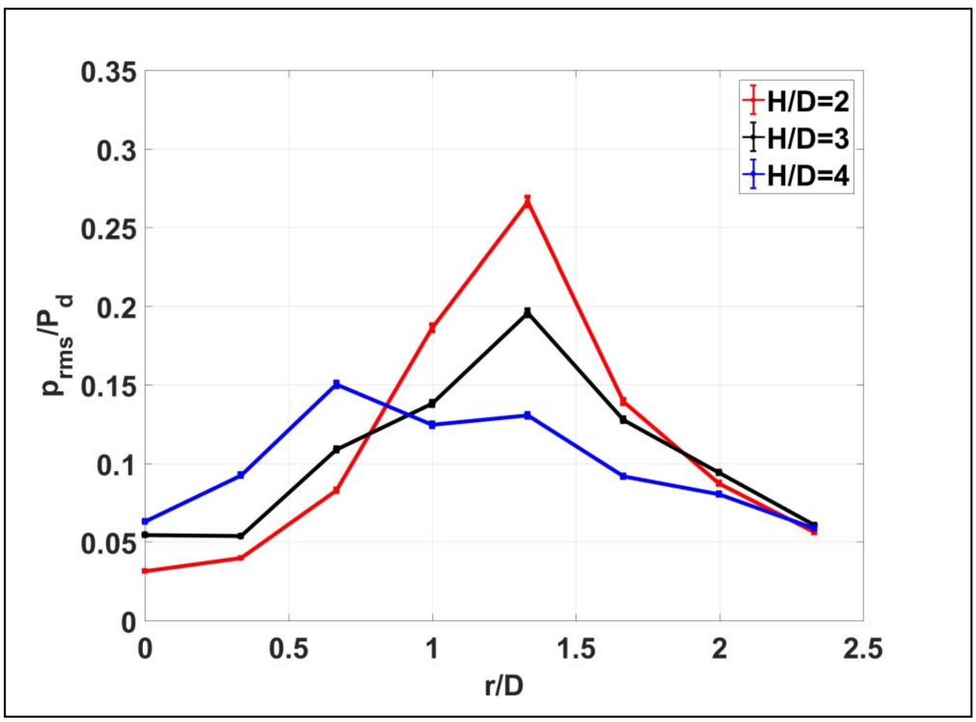

(b)

Figure 5.5 Normalized Root Mean Square Pressure (p_{rms}/P_d) versus r/D for different H/D and two Reynolds numbers: (a) Re_D = 8272, and (b) Re_D = 24818

To better examine the effect of Reynolds number, Figure 5.6.a depicts a comparison between the p_{rms} radial distributions for Re_D = 8272 and 24818 when *H/D*=2. The figure shows that as Reynolds number increases, the p_{rms} profile does not change, for all practical purposes. For both cases, the minimum pressure is at the stagnation point, where *r/D* = 0, and the maximum pressure is measured at *r/D*=1.33. Figures 5.6.b and 5.6.c depict a similar comparison for *H/D*=3 and 4, respectively. For both cases, increasing the Reynolds number, results in decreasing the level of pressure fluctuations within both the stagnation and wall-jet zones. In addition, as noted previously, a second local p_{rms} peak emerges at *r/D* = 0.67 for the higher Reynolds number and $H/D = 4$. It is unclear if this peak reflects a change in the physics of wall-pressure generation within the stagnation zone at the higher Re_D, or simply that the peak becomes observable due to reduction on the level of pressure fluctuations in the wall-jet zone.

Overall, the characteristics of the *RMS* profiles and how they change with H/D and Re_D is very consistent with those reported in the literature, and summarized in section 1.2.2.

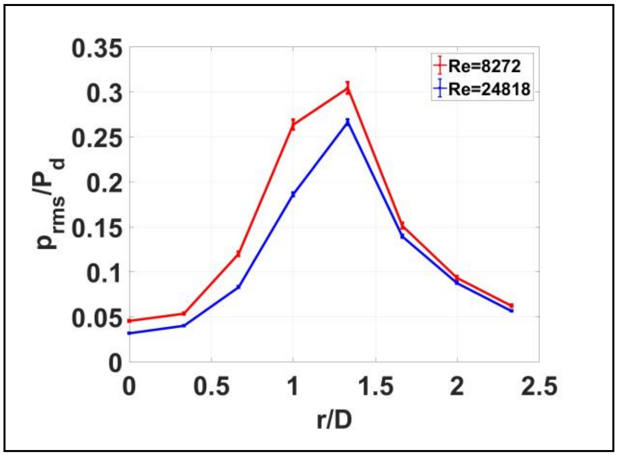

(a)

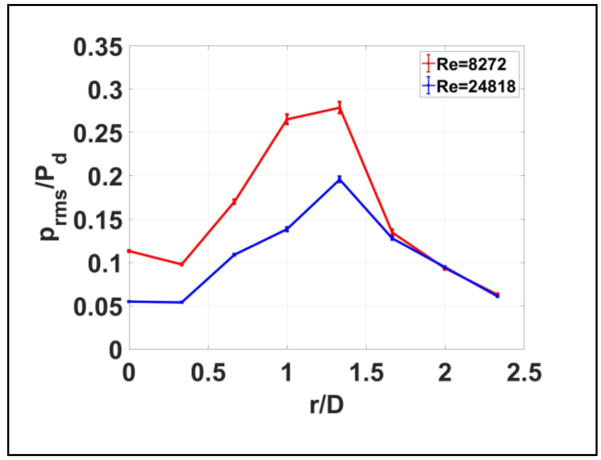

(b)

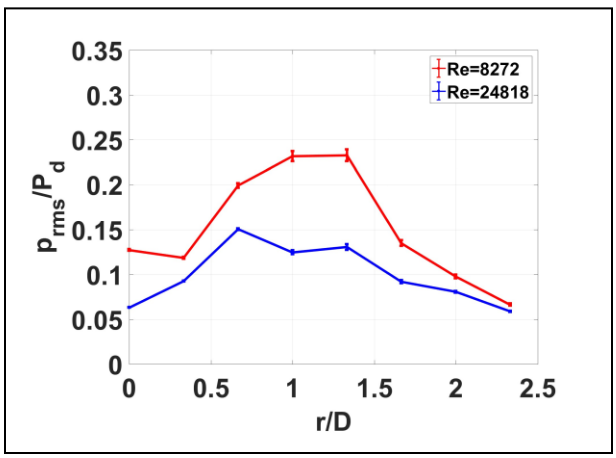

(c)

Figure 5.6 Normalized Root Mean Square Pressure (p_{rms}/P_d) versus r/D at Re_D = 8272 and 24818, for: $(a) H/D = 2$, $(b)\ H/D = 3$, and $(c)\ H/D = 4$

5.3 Time Series Analysis

5.3.1 Time Series

Figure 5.7.a depicts sample normalized-pressure signals at Re_D = 8272 at the stagnation point ($r/D = 0$) and the location of maximum p_{rms} ($r/D = 1.33$) for $H/D = 2$. As expected from the p_{rms} distribution (figure 5.5.a), the pressure signal at *r/D*=0 is low compared to that at *r/D*=1.33. Aside from this, inspecting the time series enables extraction of additional interesting information. Specifically, Figure 5.7.a demonstrates that the signal shape is completely different between the stagnation point and *r/D* = 1.33. At the former location, the signal is relatively symmetric around zero level and looks like a distorted sinusoid. In contrast, at *r/D* = 1.33, the signal is highly skewed and exhibits prominent negative spikes that reach beyond half of the jet's dynamic pressure! In his study in the same jet facility at a similar Reynolds number and *H/D*, Al-Aweni [7] used simultaneous time-resolved flow visualization and wall-pressure measurements and numerical simulations to demonstrate that these very strong pressure spikes are a result of the interaction of the jet vortices with the wall and the formation of secondary vortices (see section 1.2.2).

Similar strong negative spikes can also be seen at the same *r/D* = 1.33 location but the larger *H/D* values of 3 and 4 (figures 5.7.b and 5.7.c respectively). However, a significant difference between the signals observed at the three *H/D* values is that the average time period between spikes increases with increasing *H/D*. Based on the flow visualization of Al-Aweni [7], it is known that this increase is due to two successive pairings of the jet vortices before reaching the impingement wall: one pairing taking place between *H/D* = 2 and 3, and the other between *H/D* = 3 and 4. Interestingly, the magnitude of the spikes in figure 5.7 is almost unaffected by the *H/D* values, suggesting that the strength of the pressure produced from the vortex-wall interactions is maintained with increasing *H/D*. These observations lead to the following explanation for the decrease in the maximum p_{rms} (and likely p_{rms} in general for the whole wall-jet region as well) with increasing *H/D* (see figure 5.5): with the strength of the spikes remaining invariant with *H/D* but becoming less frequent, the p_{rms} value must decrease.

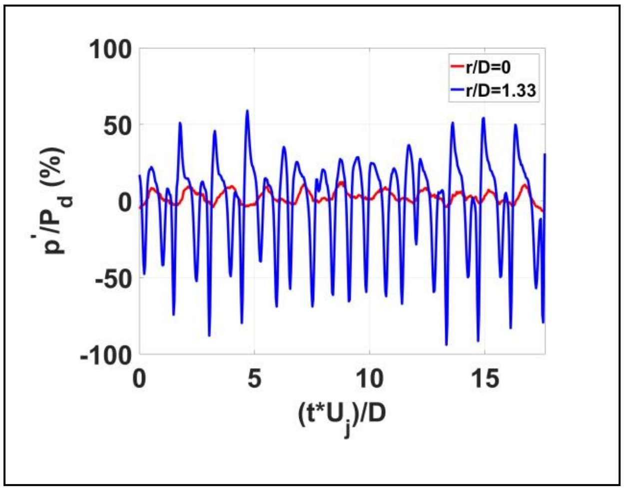

(a)

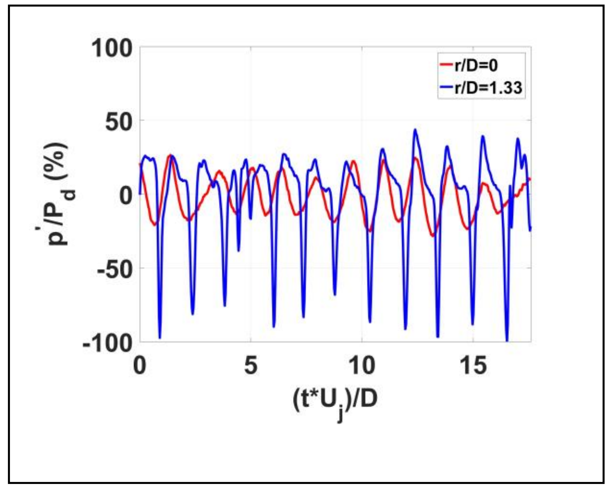

(b)

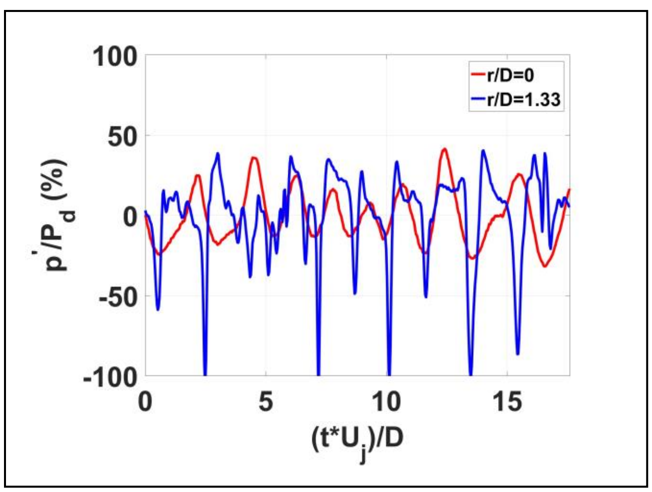

(c)

Figure 5.7 Sample normalized Pressure signals (p'/P_d %) at *Re_D* = 8272, for $r/D = 0$ and 1.33 for: $(a)\, H/D = 2$, $(\,b\,)\; H/D = 3$, and $(c)\, H/D = 4$

Figure 5.8 displays plots similar to those in figure 5.7 for the higher Reynolds number. Generally speaking, observations similar to those made in relation to figure 5.7 can be made from figure 5.8. However, there are also some notable differences. One of these relate to the strength of the negative pressure spikes. Unlike the time series for Re_D=8272, the strength of the negative pressure spikes at r/D = 1.33 decreases noticeably with increasing H/D for Re_D=24818. This decrease is associated with the signal becoming more irregular and the appearance of high-frequency fluctuation. This is consistent with the decrease in the p_{rms} level with increasing Re_D observed in figures 5.6.b and 5.6.c at H/D = 3 and 4 respectively. The signal forms in figure 5.8.b and figure 5.8.c suggest that this decrease is associated with weakening of the pressure spikes at the higher Reynolds number and larger H/D, which might be related to the jet vortices breaking up and becoming irregular/turbulent with increasing Reynolds number (as implied from the irregularity of the signal and appearance of high frequency fluctuations).

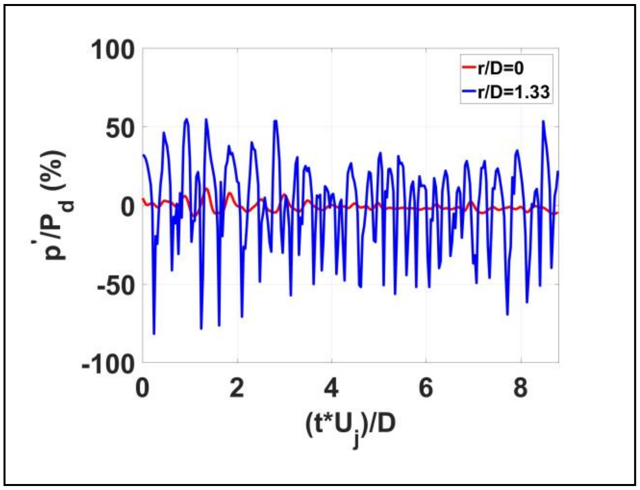

(a)

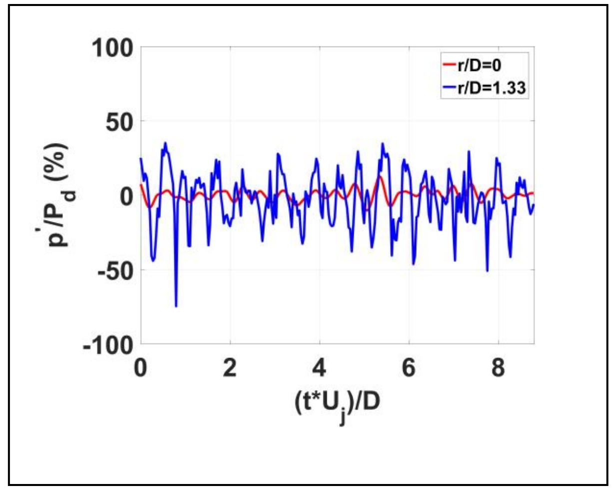

(b)

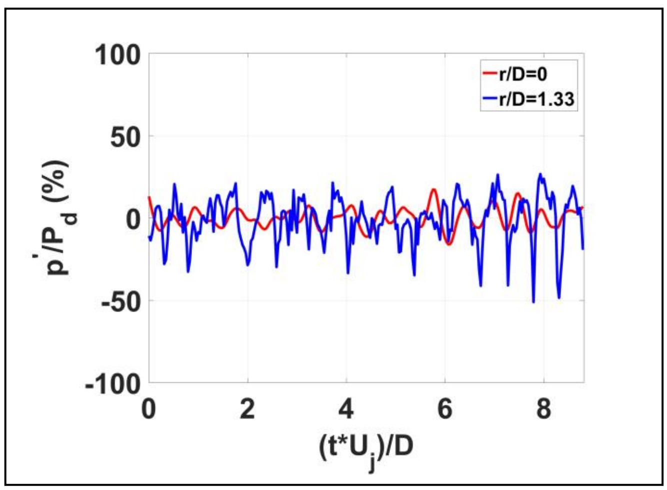

(c)

Figure 5.8 Sample normalized Pressure signals (p'/P_d %) at Re_D = 24818, for $r/D = 0$ and 1.33 for: (a) $H/D = 2$, (b) $H/D = 3$, and (c) $H/D = 4$

5.3.2 Probability Density Function (pdf)

The time series analysis in the previous section sheds light on the general characteristics of the pressure signal at the stagnation point, as well as where p_{rms} is highest in the wall-jet zone. However, these observations are based on short, randomly selected time series samples. Therefore, to ensure that the observations made in section 5.3.1 are statistically relevant, Probability Density Function (*pdf*) results are examined. The *pdf* was estimated by finding the maximum and minimum fluctuating-pressure values in a given time series. The range bound by these values was then divided into 30 equal-width bins. Finally, the number of data points falling in each bin was divided by the total number of points in the time series and the bin width to obtain the probability of the pressure value occurring within a given bin per bin width, or the *pdf*.

Figure 5.9 depicts the *pdf* for the pressure time series at Re_D = 8272 and $r/D = 0\ and\ 1.33$ for all three H/D values. By examining the plots, we can see that at $r/D = 0$, the *pdf* is approximately symmetric and narrow, which is consistent with the symmetric, low-level character of the corresponding signals observed in figure 5.7. On, the other hand, at $r/D = 1.33$, the signal has a pronounced negative skewness, as reflected in the long negative tail and consistent with the strong negative pressure spikes noted earlier in figure 5.7. In addition, the *pdf* is substantially wider than that at $r/D = 0$, consistent with the smaller p_{rms}/P_d at $r/D = 0$ (figure 5.5.a).

Another interesting observation at *H/D* = 2, is the presents of a plateau with a hint of a peak at $p_{rms}/P_d \approx -0.5$. This suggest the presence of a bi-model phenomenon. Interestingly, Al-Aweni[7] found the vortex structures to either merge as they convect past $r/D = 1.33$ or to pass without merging. This may explain the subtle bi-modal feature of the pdf at $r/D = 1.33$ in figure 5.9.a

At $r/D = 0$, the width of the *pdf* increases with increasing *H/D*, demonstrating the increasing level of p_{rms}/P_d at the stagnation point with larger *H/D* (see figure 5.5.a). At $r/D = 1.33$, the pdf remains negatively skewed with increasing *H/D*, approximately reaching negative pressure values as high as $-P_d$ for all *H/D* values. However, the pdf appears to become overall narrower with increasing *H/D*, consistent with the corresponding reduction in p_{rms}/P_d (see figure 5.5.a). The narrowing of the pdf primarily manifests itself in the reduction in the *pdf* value for the large negative pressure spikes (p approximately less than $-0.5\, p_{rms}$), which reinforces the idea discussed in section 5.3.1 of these spikes becoming less frequent at larger H/D due to vortex pairing.

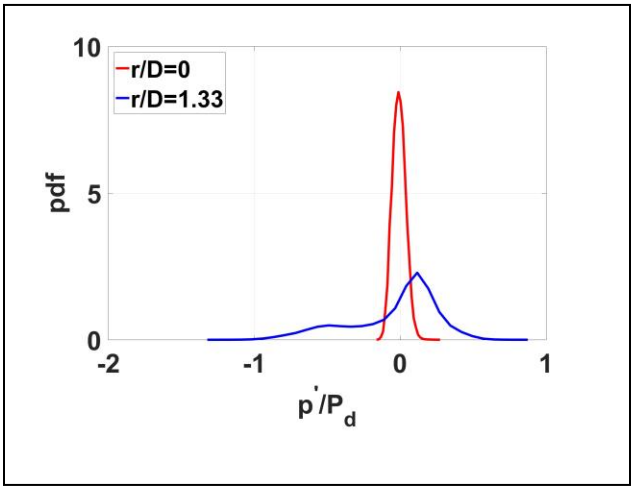

(a)

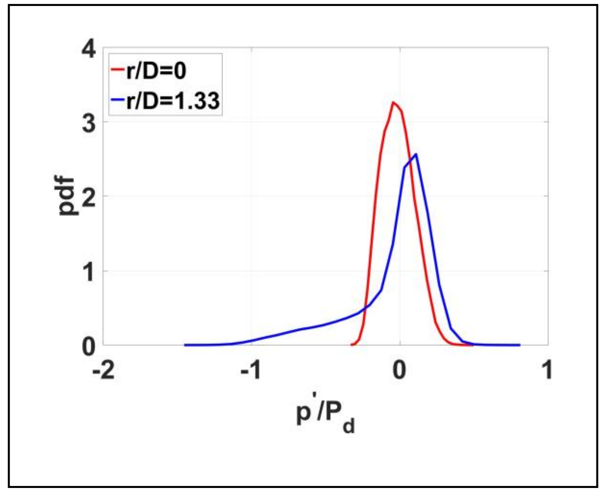

(b)

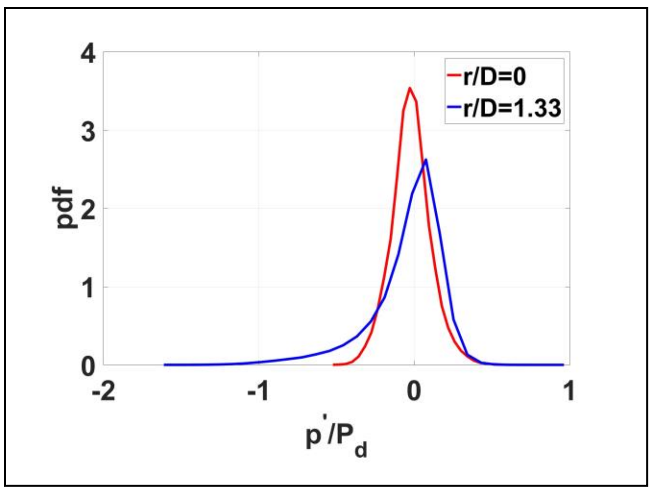

(c)

Figure 5.9 Probability Density Function (pdf) for the pressure signal at Re_D = 8272, for $r/D = 0$ and 1.33, and: $(a)\, H/D = 2, (b)\, H/D = 3,$ and $(c)\, H/D = 4$

Figure 5.10 depicts the pdf results for Re_D = 24818 at $r/D = 0$ and 1.33, and all H/D values. By examining these plots, we can see the same general behavior as seen for Re_D = 8272. However, there are some notable differences. Overall, the *pdf* at *r/D* = 1.33 is not as strongly skewed as for the lower Reynolds number case. Additionally, the long negative tail of the *pdf* extends to smaller negative-pressure magnitudes with increasing *H/D*; in contrast to reaching approximately the same value for Re_D = 8272. The reduction in the magnitude of the negative spikes with increasing *H/D* was also noted earlier from the time series plots in figure 5.8.

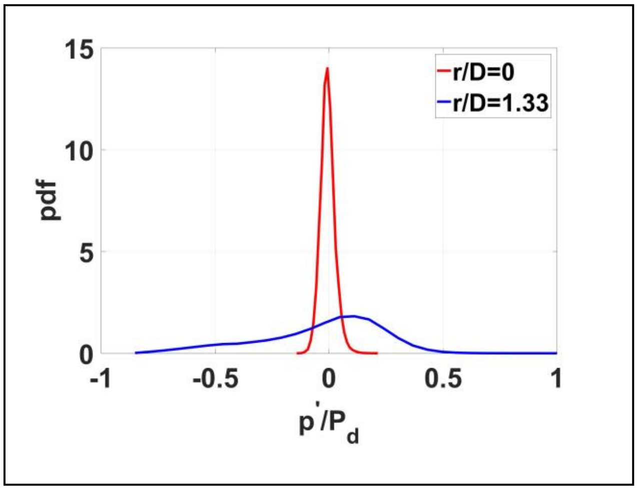

(a)

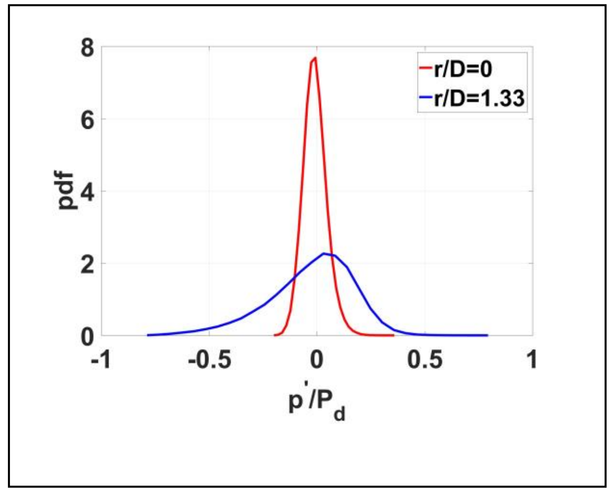

(b)

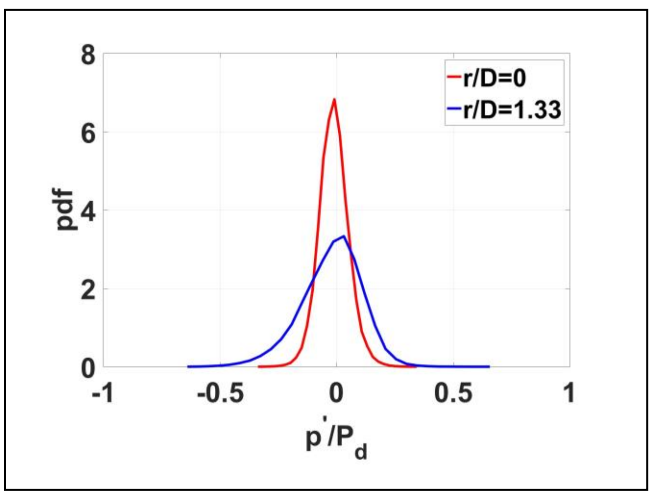

(c)

Figure 5.10 Probability Density Function (pdf) for the pressure signal at Re_D = 24818, for $r/D = 0\ and$ 1.33, and: $(a)\ H/D = 2, (b)\ H/D = 3,$ and $(c)\ H/D = 4\ \ H/D = 4$

5.3.3 Skewness and Kurtosis

The overall features of the *pdfs* presented in section 5.3.2 may be expressed in terms of their skewness and kurtosis. The skewness provides a measure of the symmetry of the *pdf*. A skewed *pdf* exhibits a long negative tail (if negatively skewed) or a positive one (if positively skewed). On the other hand, the kurtosis indicates how flat (as opposed to having a prominent peak) a *pdf* distribution is. A *pdf* with large kurtosis tends to have long tails. For reference, a Gaussian *pdf* has a skewness of zero (due to its symmetry) and a kurtosis of 3. In the present work, the skewness and kurtosis were calculated as follows

$$Skewness = \sum_{i=1}^{n} \frac{(p_i - P)^3/n}{\sigma^3} \tag{5.3}$$

$$kurtosis = \sum_{i=1}^{n} \frac{(p_i - P)^4/n}{\sigma^4} \tag{5.4}$$

where, p_i is the instantaneous pressure, *P* is the mean pressure, *i* indicates the time index, or sample number in the digitized pressure time series, σ is the standard deviation of the pressure time series points, and *n* is the total number of samples in the time series

Figure 5.11.a depicts the variation of skewness over the measurement domain (*r/D* range 0 to 2.33) for a Reynolds number of 8272 at *H/D* = 2, 3, and 4. The plots show that at *H/D*=2, the pressure signal has positive skewness in the stagnation zone ($r/D \leq 1$), but it switches sign and becomes negative in the wall-jet zone. For *H/D*=3 and 4, the switch from positive to negative skewness happens near the end of the stagnation zone. The negative skewness is particularly strong at *r/D* = 1.33 and 1.67. This is consistent with the long negative tail of the *pdfs* and the strong negative pressure spikes in the time series discussed earlier for *r/D* = 1.33. However, as *r/D* increases further, the skewness magnitude decreases monotonically; though it remains negative.

Figure 5.11.b depicts the skewness results for the higher Reynolds number of 24818. With the exception of one apparently errant data point (at $r/D = 0.33$ and $H/D = 4$), the general qualitative behavior of the skewness distribution is similar to the lower Reynolds number. However, at $Re_D = 24818$, the largest negative skewness is not as large in magnitude as for $Re_D = 8272$. Also, the skewness becomes zero (or low valued) by $r/D = 2.0$; implying the *pdfs* reach symmetry by the end of the measurement domain.

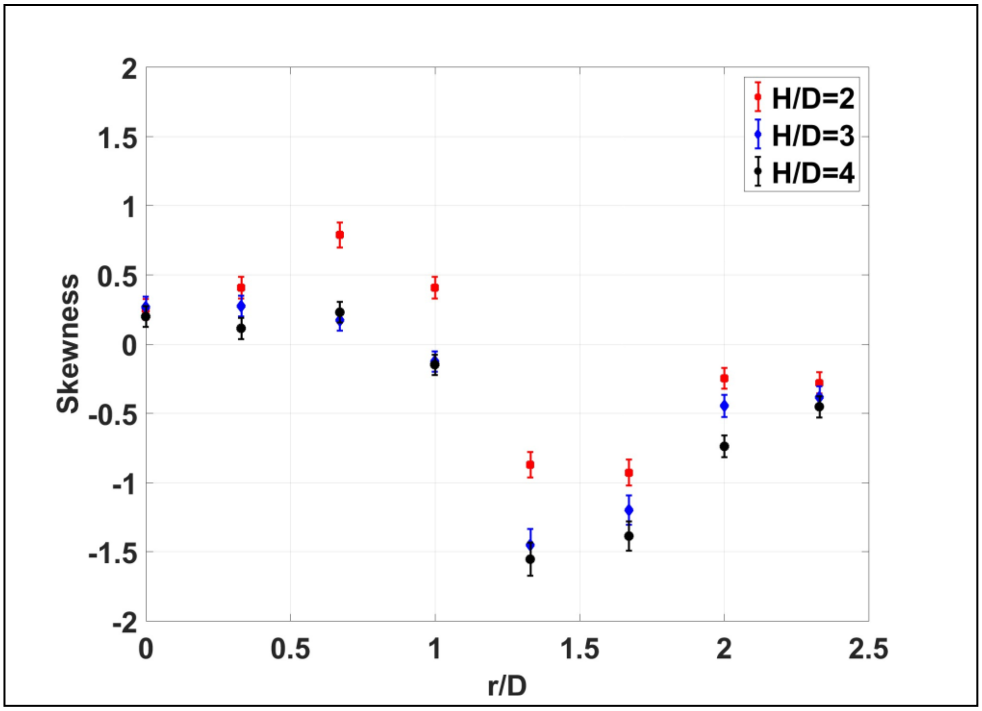

(a)

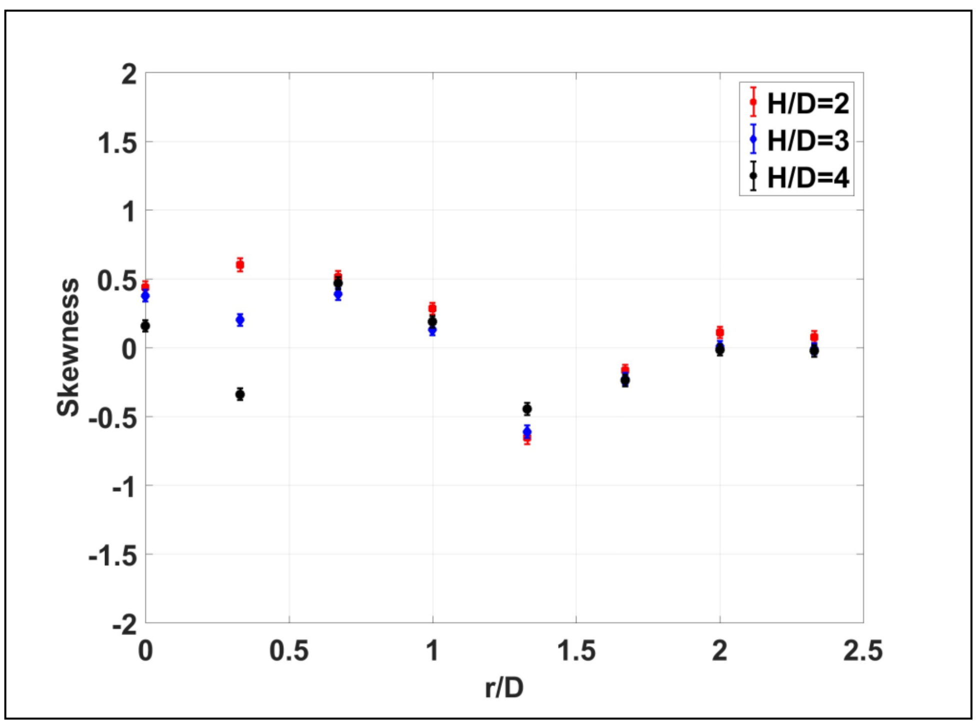

(b)

Figure 5.11 Radial distribution of skewness for $H/D = 2, 3$ and 4, and: $(a) Re_D = 8272$, and $(b) Re_D = 24818$

Figure 5.12.a depicts the kurtosis results for Reynolds number of 8272. Within the stagnation zone ($r/D \leq 1$), the kurtosis is similar to that of a normal (Gaussian) distribution with a magnitude near 3. In the wall-jet zone, the kurtosis initially increases substantially (up to the radial location *r/D* = 1.67) then it decays monotonically. For the higher Reynolds number, the kurtosis behavior (figure 5.12.b) is surprisingly different. In this case, the kurtosis is highest at the stagnation point and decays monotonically with increasing *r/D*. The reason for the fundamental change in kurtosis behavior with Reynolds number is not clear. Measurements at intermediate Reynolds numbers would be recommended in order to observe if this change is gradual or abrupt, and attempt to understand the reasons behind it.

The large magnitude of negative skewness and kurtosis near the location of maximum p_{rms} in the wall jet zone indicates the presents of strong pressure spikes. This is consistent with the strong negative peaks found in the work of Didden and Ho [5], Hall and Ewing [9,10] and Al-Aweni [7]. The latter study connected the formation of the spikes to the secondary vortex formation (as also Didden and Ho [5] and Hall and Ewing [9,10]), and the formation of high strain zone in the boundary layer beneath the jet vortex.

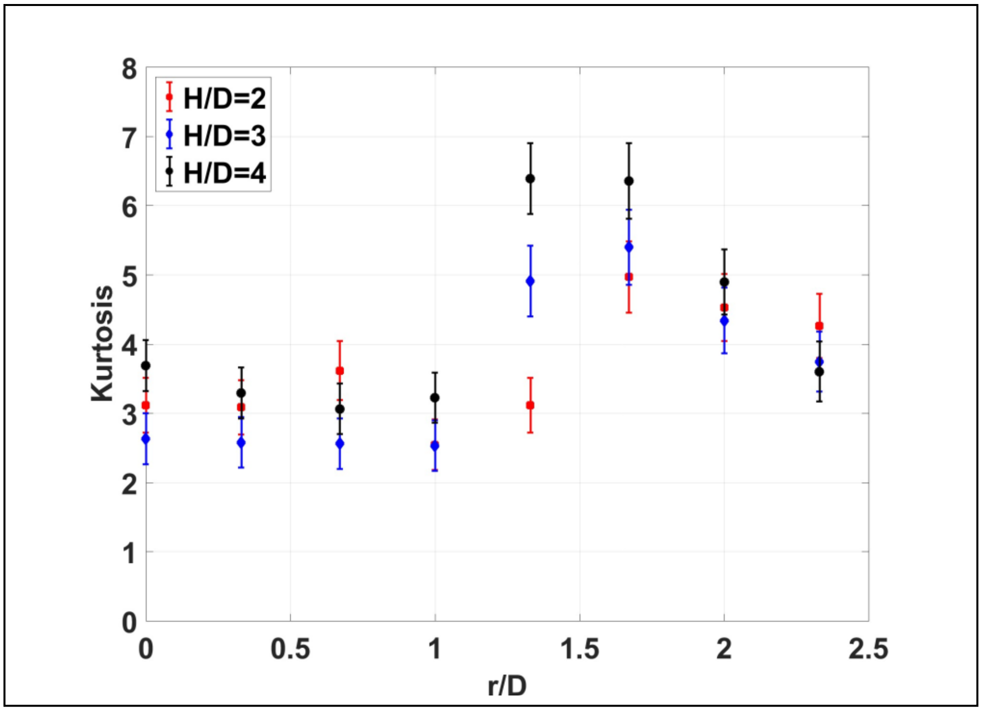

(a)

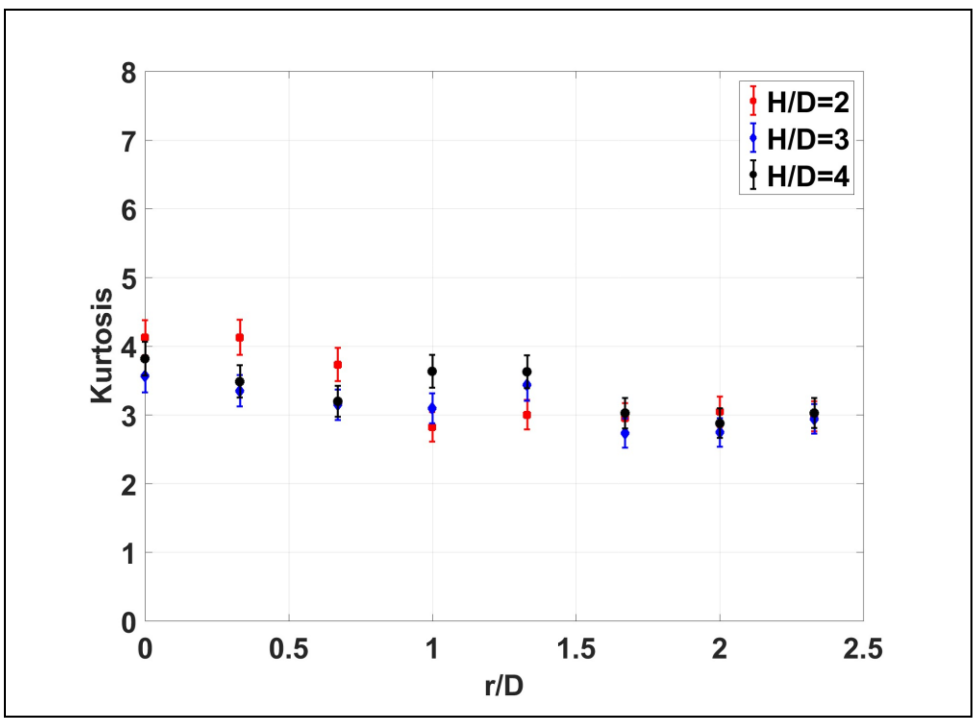

(b)

Figure 5.12 Radial distribution of Kurtosis for $H/D = 2, 3$ and 4, and: $(a) Re_D = 8272$, and

$(b) Re_D = 24818$

5.4 Spectra Analysis

Analyzing spectra of the pressure fluctuations is considered one of the useful tools to get information about the frequency content of the pressure signal. In this work, spectral information is presented as power spectral density (*PSD*). The *PSD* is calculated as an average of the *PSDs* obtained from m different pressure data records, as follows:

$$PSD(k) = \frac{1}{m * n * f_s} \sum_{i=0}^{m-1} \left| P_f^i(k) \right|^2 \tag{5.5}$$

Where, P_f^i is the Fourier transform of the i^{th} pressure data record, n is the number of points in the data record, k is an index indicating frequency and f_s is the sampling frequency. The physical frequency corresponding to each k value is given by $kF_S/n = k\Delta f$ (where Δf is the frequency resolution of the *PSD*).

To compute the *PSD*, 409600 samples of a given pressure signal were acquired at a sampling frequency of 5000 Hz. The resulting data were divided into 800 *records*, each containing 512 points. The *PSD* was obtained for each record by taking its Fast Fourier Transform (*FFT*), multiplying the transform by its conjugate, and dividing the result by the square of the number of points (512 points) and the spectrum frequency resolution (Δf = 5000/512 = 9.77 Hz). The resulting spectrum random uncertainty is 3.5%.

Figure 5.13 shows the normalized *PSD* in the form of contour plots versus *r/D* and Strouhal number ($St_D = fD/U_j$) at $Re_D = 8272$and all H/D values. This way of presenting the spectra provides a global perspective of the entire measurement domain, but it does not allow clear observation of some of the less dominant spectral features. To see these, the spectra are presented using line plots at *r/D* = 0 and 1.33 in figure 5.15. The contour plots in Figure 5.13 show a dominant spectral peak at $St_D \approx 0.6$ (the actual value varies between 0.64 for *H/D* = 2 and 3, and 0.58 for *H/D* = 4, which is approximately within the spectrum St_D resolution of 0.05). From the work of Al-Aweni [7], it is known that the $St_D \approx 0.6$ corresponds to that of the jet vortices after the first pairing.

As discussed in section 5.3.1, Al-Aweni also found that for approximately the same Reynolds number, the first vortex pairing took place as the vortices traveled parallel to the wall, within the wall-jet zone, at *H/D* = 2, and ahead of reaching the impingement plate, at *H/D* = 3. A second pairing was observed before the vortices reached the plate at *H/D* = 4. These conclusions suggest that the spectrum should be dominated by fluctuations at $St_D \approx 0.6$ at *H/D* = 2 and 3, and $St_D \approx 0.3$ at *H/D* = 4. The former expectation is consistent with the results in figure 5.13.a and 5.13.b. However, the dominance of $St_D \approx 0.6$, instead of $St_D \approx 0.3$ at *H/D* = 4 (figure 5.13.c) seems inconsistent with Al-Aweni's conclusions. The apparent discrepancy is partly due to the fact that the dominant spectrum peak in figure 5.13.c is seen within the wall-jet zone (*r/D*> 1). Inspecting a sample of the corresponding time series (figure 5.7.c), it is evident that the time series is highly irregular and dominated by strong negative spikes with varying strength (i.e. modulation) from one spike to another. The spectrum of such a signal is not expected to yield a clean peak at the dominant frequency, but rather a broader spectrum of multiple peaks. Indeed, although $St_D \approx 0.6$ is dominant in figure 5.13.c, another, barely visible peak is seen at $St_D \approx 0.3$ (pointed to by a white arrow in figure 5.13.c). This peak can also be observed more clearly in the line plots of figure 5.15.b. Although the observed peak is weaker than that at $St_D \approx 0.6$, this could be caused by the vortices being less coherent after the second merging (which was observed in the flow visualization videos of Al-Aweni). However, this reasoning cannot be ascertained at this stage.

A better indication of the presence of pressure fluctuation at the second-pairing frequency ($St_D \approx 0.3$) at *H/D* = 4 may be seen in the stagnation zone, particularly at *r/D* = 0, in figure 5.13.c. Due to the simplicity of the signal at the stagnation point (figure 5.7.c), the corresponding spectrum has a more straight forward interpretation. The contour plot in figure 5.13.c and the line plots in figure 5.15.a show that indeed when *H/D* = 4, the dominant spectral peak shifts to $St_D \approx 0.3$ at *r/D* = 0.

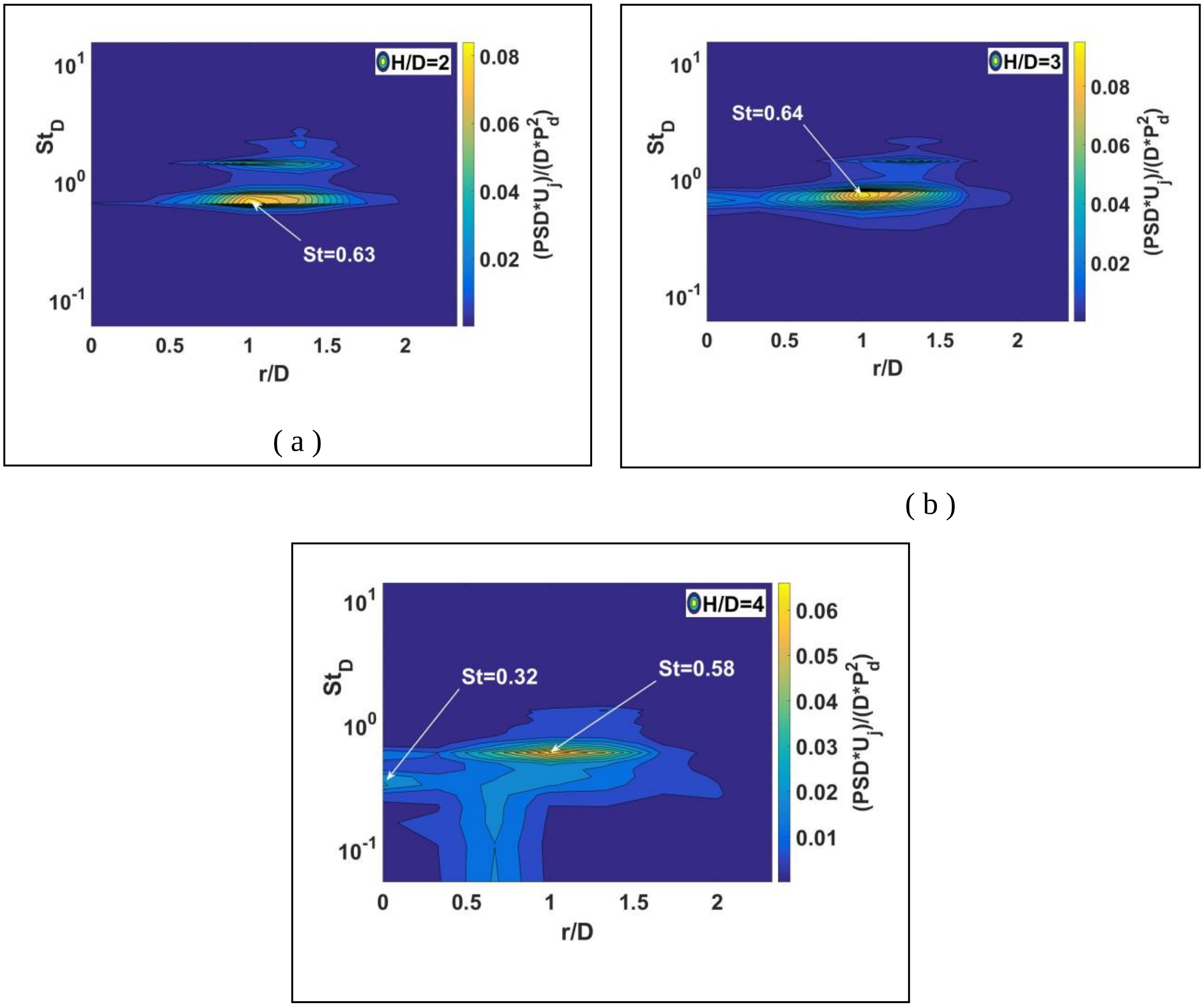

(b)

(c)

Figure 5.13 Normalized *PSD* contour plots at $Re_D = 8272$, for: $(a)\, H/D = 2$, $(b)\, H/D = 3$, and $(c)\, H/D = 4$

Figure 5.14 shows normalized *PSD* contour plots similar to those in figure 5.13 but for $Re_D = 24818$. Consistent with the lower Reynolds number, the spectrum peak at $St_D \approx 0.6$ is dominant within the wall-jet zone at *H/D* = 2 and 3. At *H/D* = 4, the dominant peak clearly shifts to $St_D \approx 0.3$ within the stagnation zone at $r/D = 0.67$. Recall that this is also the radial location where the maximum p_{rms} is found for the larger Reynolds number and *H/D* = 4 (figure 5.5.b), which is different from all other cases. These results reinforce earlier observations regarding the overall weakening of the pressure fluctuation in the wall-jet zone with increasing *H/D* and Reynolds number. Since it is known from the work of Al-Aweni that the vortex-wall interactions dominate the pressure fluctuations in the wall-jet zone at low Reynolds number, the present results suggest that the ability of these interactions to generate unsteady pressure weakens with increasing Reynolds number, leading to the observed dominance within the stagnation zone.

Another notable characteristic of the spectra at the higher Reynolds number is the rise of low-frequency fluctuations. These are seen clearly in both the contour plot in figure 5.14.c and the line plots in figure 5.16. The latter plots also show the general shift of the dominant frequency towards low values with increasing *H/D* (figure 5.16.a).

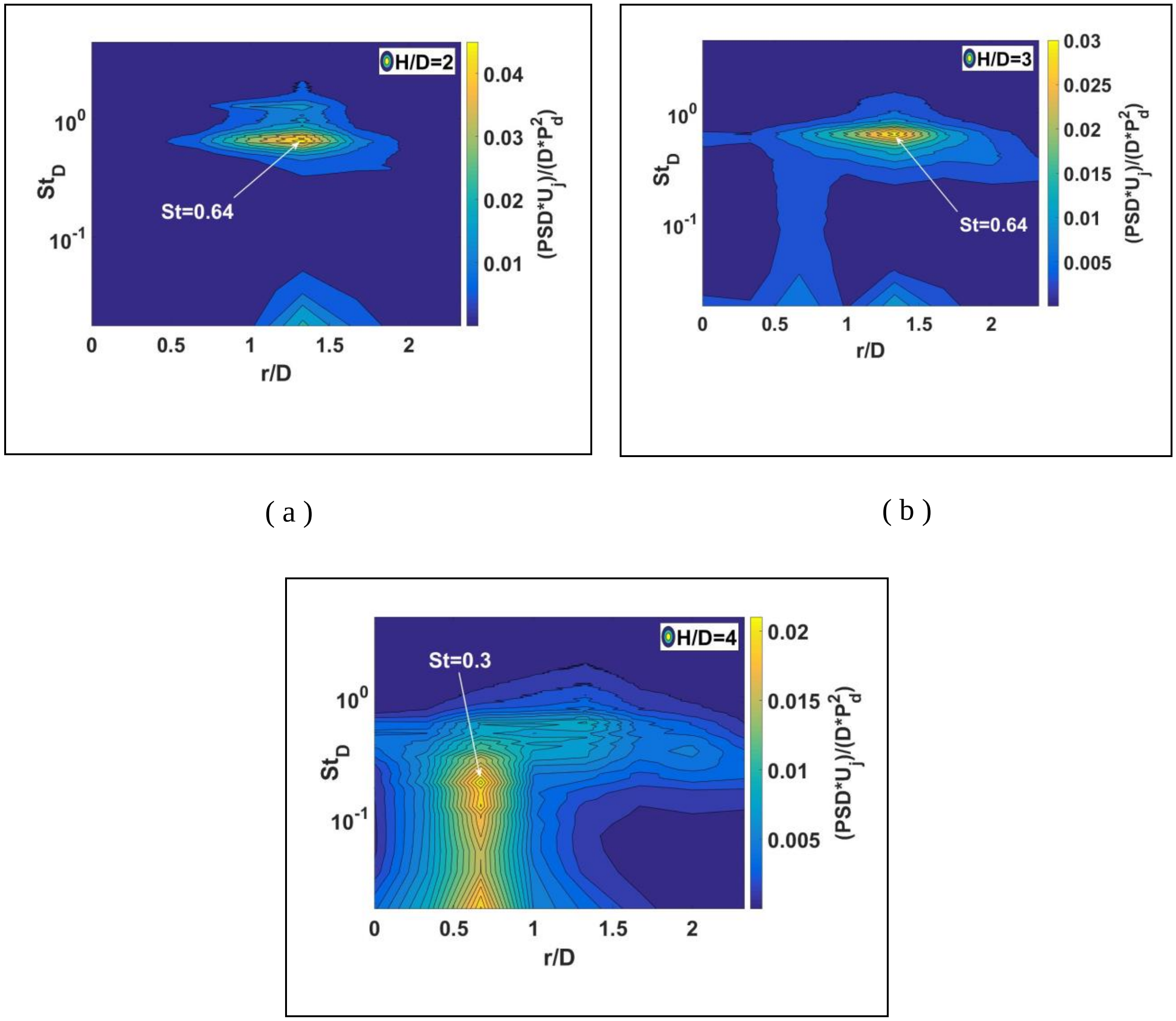

(a) (b)

(c)

Figure 5.14 Normalized PSD contour plots at $Re_D = 24818$, for: $(a)\, H/D = 2$, $(b)\, H/D = 3$, and $(c)\, H/D = 4$

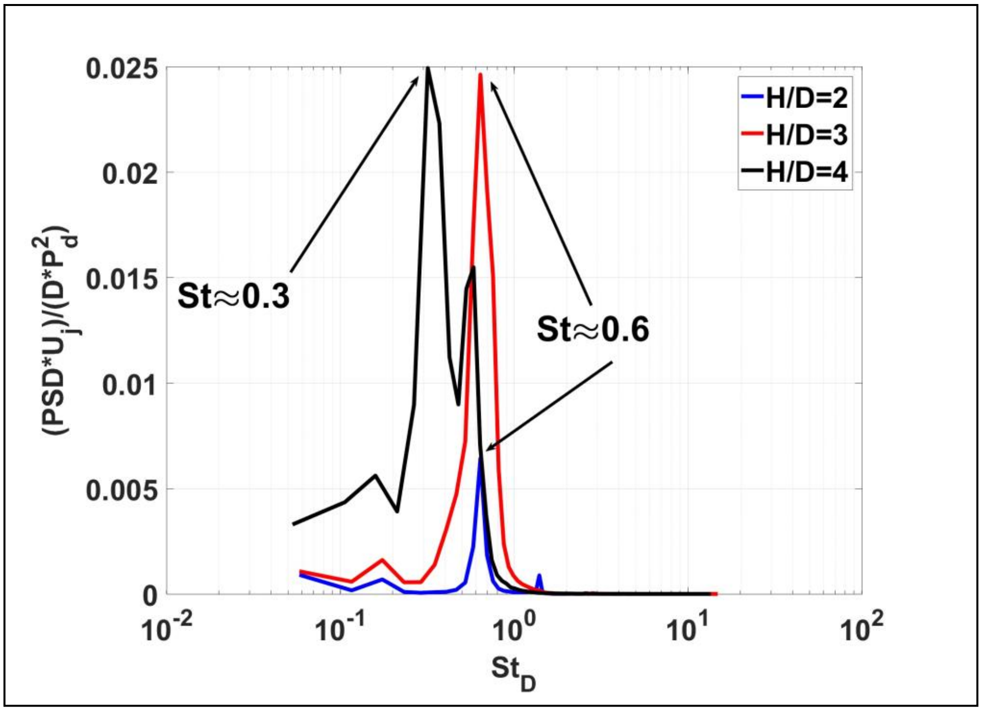

(a)

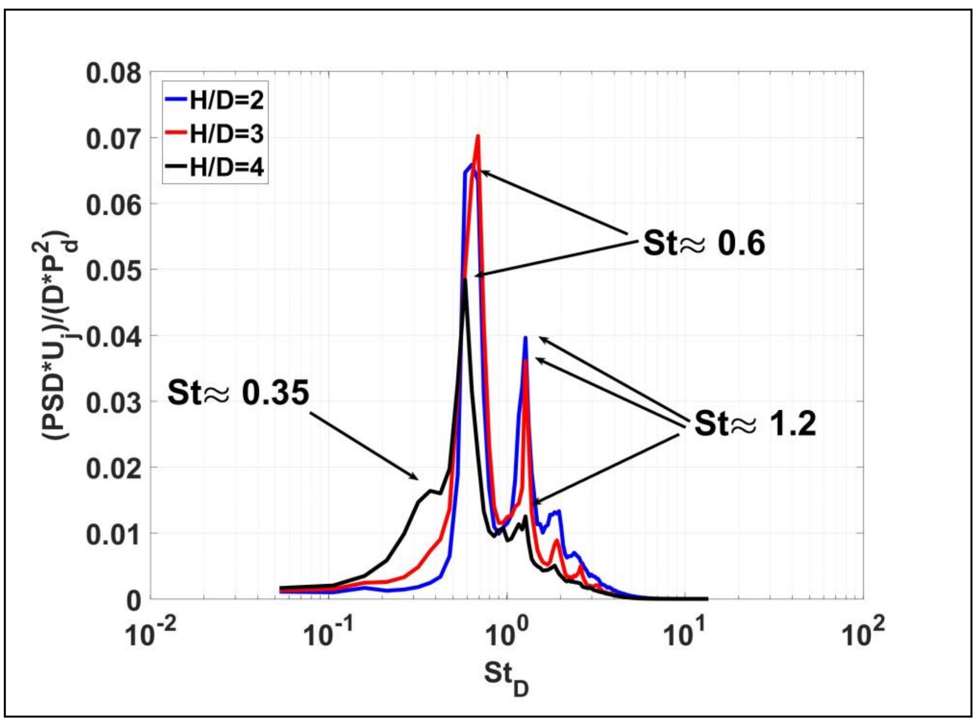

(b)

Figure 5.15 Normalized PSD at $Re_D = 8272$ for, $H/D = 2{,}3$ and 4, at:

$(a)\, r/D = 0$ and $(b)\, r/D = 1.33$

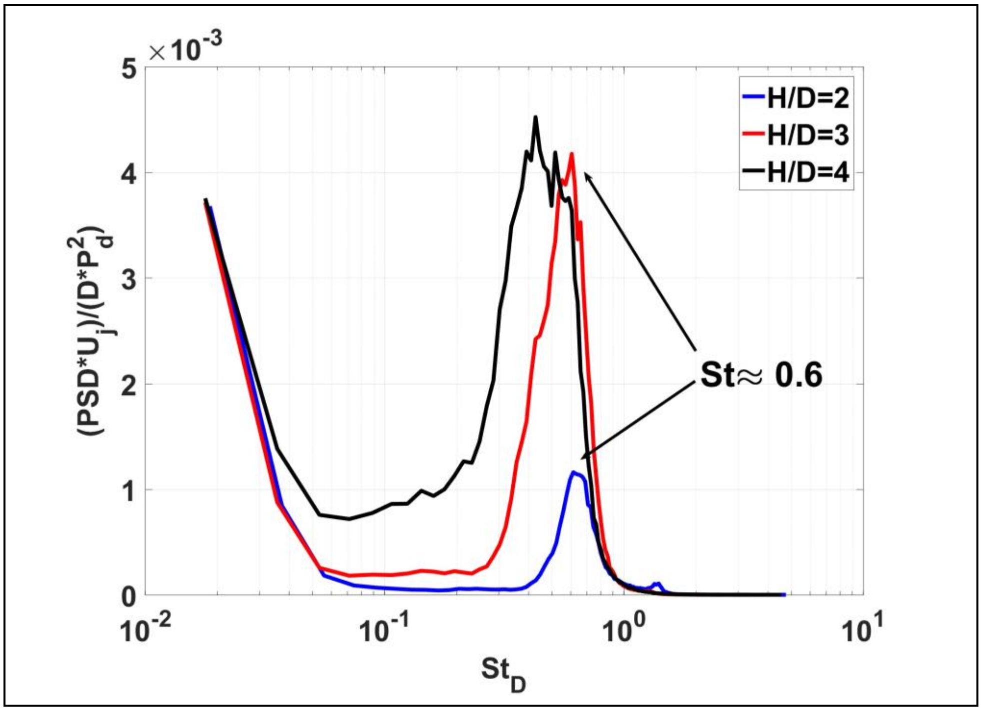

(a)

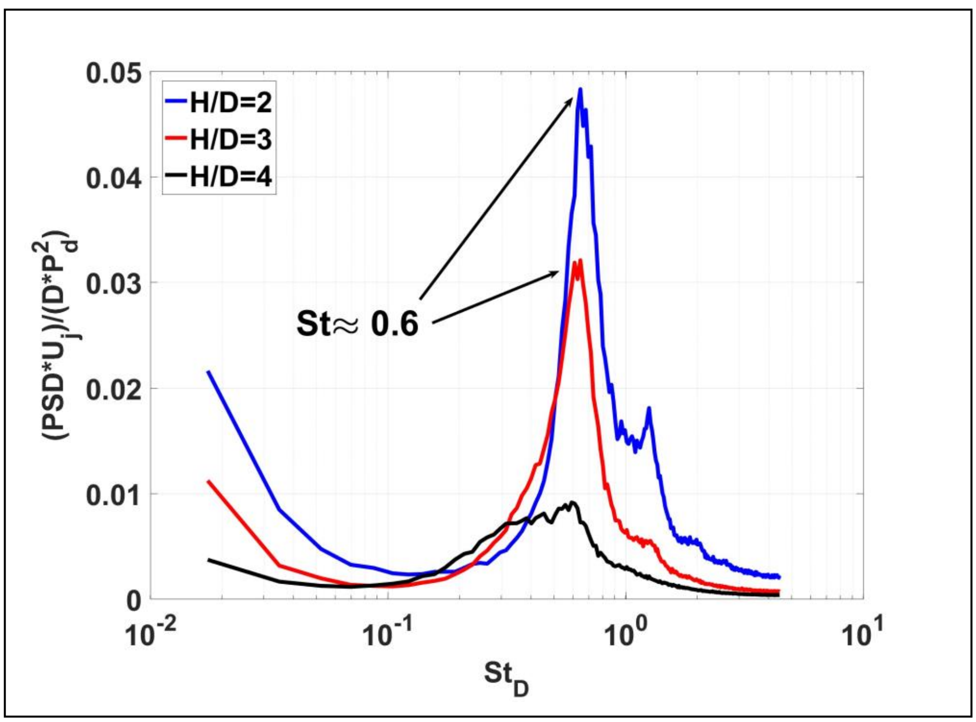

(b)

Figure 5.16 Normalized PSD at $Re_D = 24818$, for $H/D = 2,3$ and 4, at:

$(a)\, r/D = 0\ and\ (b)\, r/D = 1.33$

Figures 5.17 and 5.18 depict a direct comparison of the normalized *PSD* at the two different Reynolds number ($Re_D = 8272\ and\ 24818$). These plots are provided to facilitate understanding of the Reynolds number effect on the spectra. Overall, both figures show that the Strouhal number band of the pressure fluctuations is consistent for both Reynolds number. However, the *PSD* has higher level and sharp peaks at the lower Reynolds number; in comparison to being broader and having lower level with increasing Reynolds number. This suggests that the basic wall-pressure generating mechanisms remain the same with increasing Reynolds number, but they become weaker and more stochastic in nature. In addition, at the largest *H/D* of 4, and the high Reynolds number, the vortex-wall interaction effectiveness in generating pressure in the wall jet zone weakens substantially.

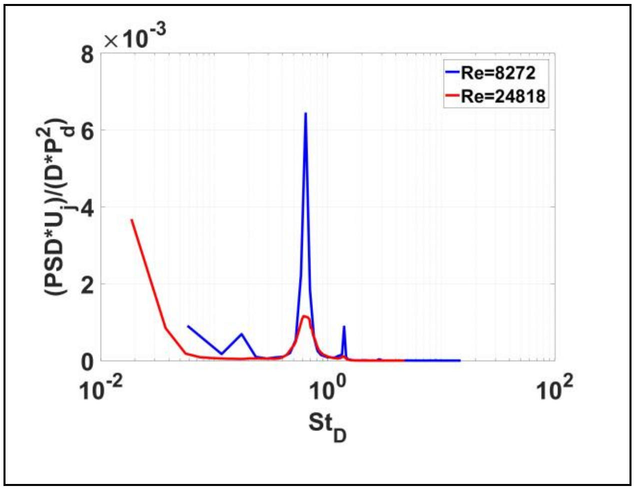

(a)

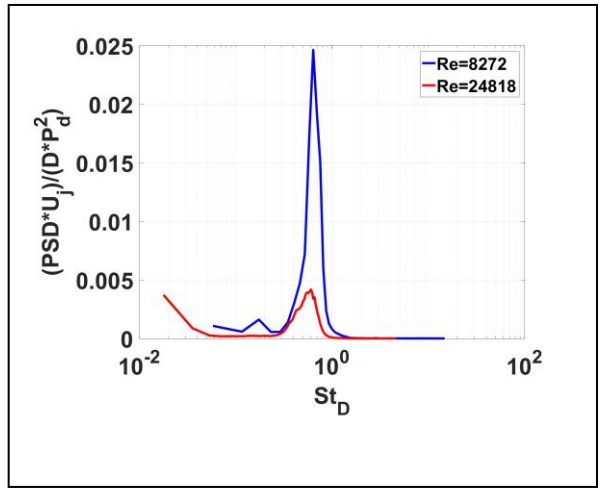

(b)

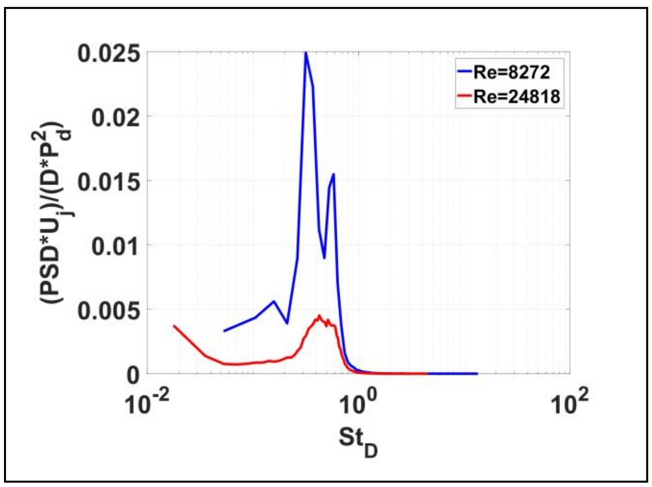

(c)

Figure 5.17 Normalized PSD at $Re_D = 8272\ and\ 24818\ and\ r/D = 0$, for: $(a)\ H/D = 2$, $(b)\ H/D$ and $(c)\ H/D = 4$

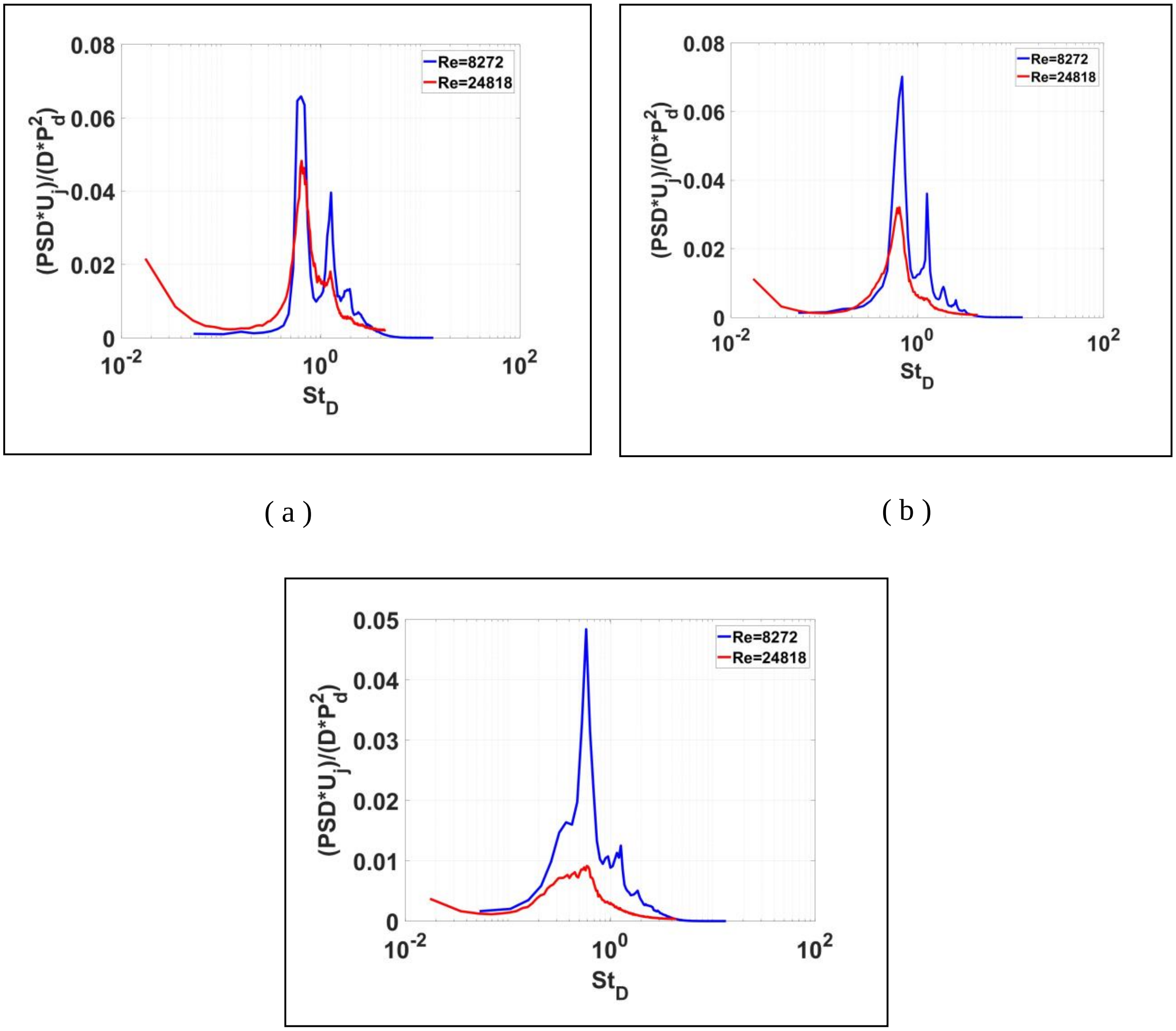

(a) (b)

(c)

Figure 5.18 Normalized PSD at $Re_D = 8272\ and\ 24818\ and\ r/D = 1.33$, for: $(a)\ H/D = 2$, $(b)\ H/D$ and $(c)\ H/D = 4$

5.5 Comparison between Experiment and Mathematical Model

In the present section, a comparison is conducted between the results of the experiments and the model. The purpose of this comparison is to assess the degree by which the model is successful in capturing the underlying physics of wall-pressure generation in impinging jets. It is emphasized here that, given the fairly crude nature of the model, the comparison is focused on qualitative features and trends and is constrained to the stagnation zone of the impinging jet.

The discussion in section 3.1 demonstrated that the character of the modeled wall-pressure time series is different depending on whether the radial location is near the stagnation point ($r/D < 0.5$) or the end of the stagnation zone ($r/D > 0.5$). Near the stagnation point, the pressure signal was weaker and characterized with sinusoidal like variation, and the end of the stagnation zone, the signal featured a prominent negative pressure peak and a strong, but less prominent positive peak. The pressure variation (which are replicated at the bottom of figure 5.19) were connected to "remote" (at $r/D = 0$), and "local" (at $r/D = 1$) effects of vortex passage. Comparing similar signals obtained experimentally at the lower Reynolds number and $H/D = 4$ (top of figure 5.19), we see very similar qualitative features, suggesting that he basic physics of wall-pressure generation in the stagnation zone are captured by the present model, notwithstanding its high level of simplicity.

Some of the differences between the experimental and model results in figure 5.19 include the broadness of the positive and negative peaks at $r/D = 1$. The experimental time series clearly exhibit much broader peaks, which is not surprising given that the real jet vortices have a finite core size, in comparison to the point vortices employed in the present model. Thus, one of the important future improvements of the model is to utilize finite-core vortices; for example, Oseen type, having Gaussian vorticity distribution. This point is also important from the perspective that whether a point on the wall is influenced by “remote” versus “local” vortex effects is expected to depend on how far is the point from the vortex center, relative to the vortex core size.

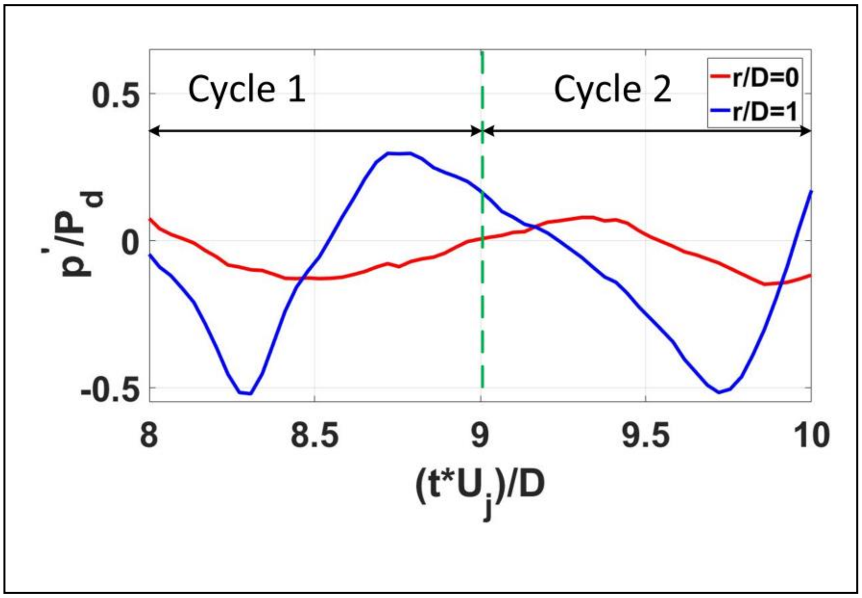

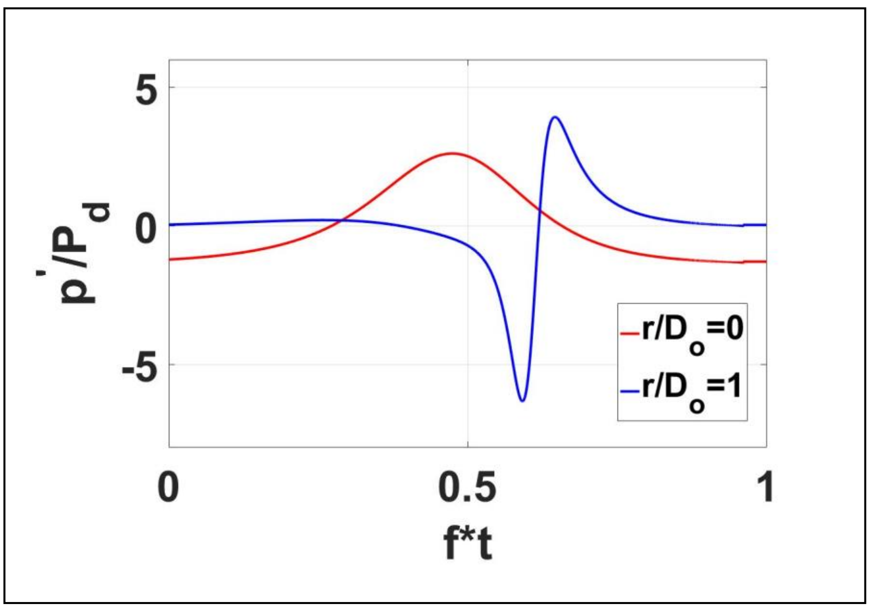

Figure 5.19 Sample time series from microphone measurements (top) and the vortex-array model (bottom) at the stagnation point ($r/D = 0$) and end of the stagnation zone ($r/D = 1$). Experimental data are shown for the $Re_D = 8272$ and $H/D = 4$, and model results for the reference case (emulating the conditions at the end of the potential core).

Though shown over a short time period, the experimental time series in figure 5.19 is characteristic of the remainder of the time series, with the shown signature repeating quasi-periodically. However, at $r/D = 1$, there are moments in time were the signature character is different. This is exemplified in figure 5.20 for the same time-window size as the top of figure 5.19. The signal shape during such periods is very similar to that associated with the vortex-induced separation of the boundary layer. This conclusion can be made based on the work of Al-Aweni [7]. Such vortex-boundary-layer interactions cannot be captured by the present model, which is both inviscid and does not include any modeling of boundary layer effects.

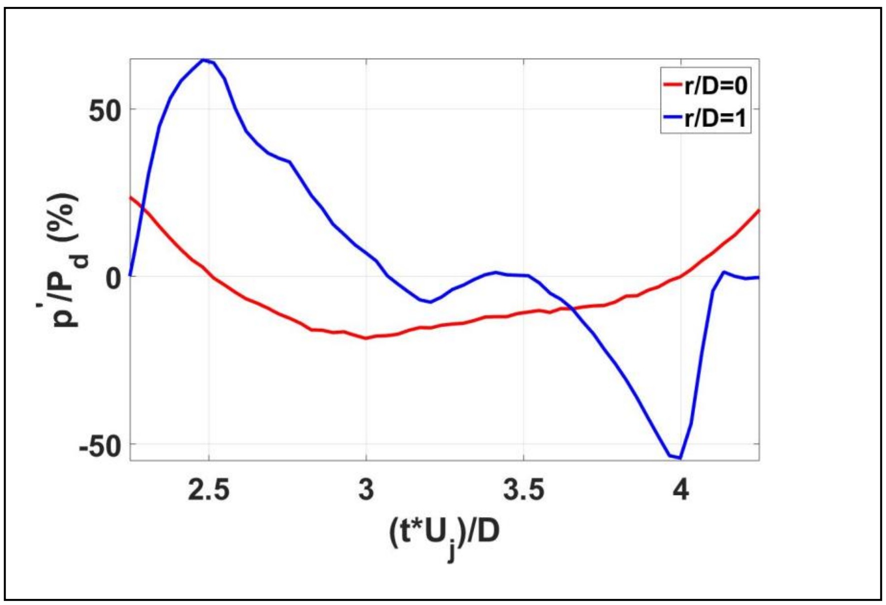

Figure 5.20 Sample wall-pressure signature characteristic of that produced by vortex-induced separation from microphone measurements at $r/D = 1$, $Re_D = 8272$ and $H/D = 4$

Another point concerning the comparison in figure 5.19 is that it is done using the experimental data at the lower Reynolds number. At the higher Reynolds number, as discussed previously, small-scale pressure fluctuations start to appear, implying the formation of small-scale turbulence. Such turbulence, which obviously cannot be reproduced by the present model, makes it more difficult at times to identify the vortex-passing signature in the time series.

Another interesting qualitative feature of wall-pressure fluctuation in the stagnation zone that is captured by the vortex-array model relates to the effect of H/D on p_{rms}. The reader is reminded that the effect of increasing H/D in the model is simulated by decreasing the vortex passing frequency; i.e. emulating the reduction in frequency via vortex pairing. This frequency effect, which was presented in figure 3.4 and is reproduced in the bottom of figure 5.21, is qualitatively similar to that seen in the experimental results (figure 5.21 top). At high frequency (small H/D), both model and experimental results show the pressure fluctuations to be lowest at the stagnation point and rise to be highest at the end of the stagnation zone. As the frequency decreases (H/D increases), the level of pressure fluctuations increases at the stagnation point. Also both the model and the experimental results show that within the zone $r/D < 0.5$, the pressure fluctuations increase with r/D at highest-frequency (smallest H/D), while they decrease with r/D for the middle and lowest frequency ($H/D = 3\ and\ 4$). For all cases, the *RMS* pressure level increases with r/D when $r/D > 0.5$ (within the stagnation zone) for both the model and the measurement results.

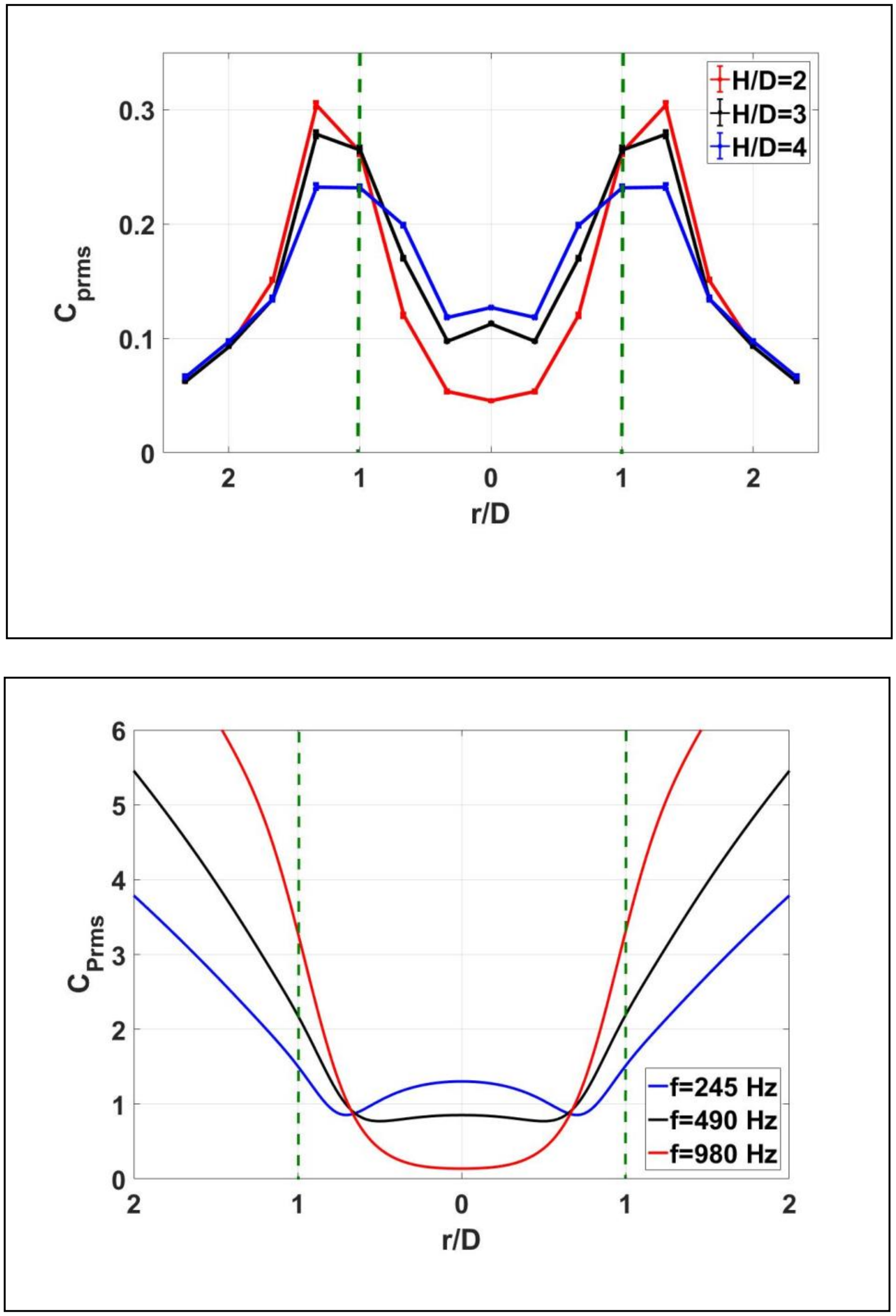

Figure 5.21 Comparison of the effect of varying H/D on RMS wall-pressure fluctuation between the experimental (top) and the model (bottom) results at $Re_D = 8272$. In the model, increasing frequency corresponds to decreasing H/D. The broken green lines outline the end of the stagnation zone

Figure 5.21 also show consistency between the calculation and the measurement in that the trend of increasing *RMS* level with increasing H/D (decreasing frequency) at the stagnation point, reverses by the end of the stagnation zone. The switching point, which happens at a specific r/D location in the model results, happens at different r/D locations in the measurements, depending on which two H/D cases are considered. This difference in the location of switching might be due to the increasing vortex core size with increasing H/D (due to vortex pairing); an effect that is not captured in the present model but need to be included in future development of the model.

Finally, figure 5.22 demonstrates the general consistency between the experimental (top plot) and the model (bottom plot) results regarding Reynolds number effect. In both cases, as Reynolds number increases, the fluctuating pressure level decreases. Based on the discussion of the model results in section 3.2, the overall decrease in the normalized *RMS* pressure fluctuation with Reynolds number is predominantly due to the increase of the normalization scale (the jet dynamic pressure) while the level of pressure fluctuation remaining invariant. Of course in the real jet it is not expected that the jet's dynamic pressure would increase with Re_D without affecting the strength of the vortices, and hence the wall-pressure fluctuation. However, a more realistic interpretation of the clue from the model results is that perhaps the strength of the jet vortices increases with Re_D at a slower rate than the jet's dynamic pressure. This idea leads to the following hypothesis: the vortex strength (vorticity/circulation) is expected to increase in proportion to the shear in the separating shear layer, which is expected to scale as the viscous shear stress in the separating boundary layer. The latter is expected to be proportional to $Re_D^{0.5}$, based on laminar boundary layer theory (Al-Aweni [7] showed that the boundary layer at the jet exit is laminar over the Reynolds number investigated). In contrast, the dynamic pressure should increase as Re_D^2. Thus, if the wall pressure increases in proportion to the square of vorticity/circulation (based on the pressure source term in equation 1.7) of the jet vortices, the *normalized* pressure would decay as Re_D^{-1}. This could explain the decay of the normalized pressure fluctuation with Reynolds number.

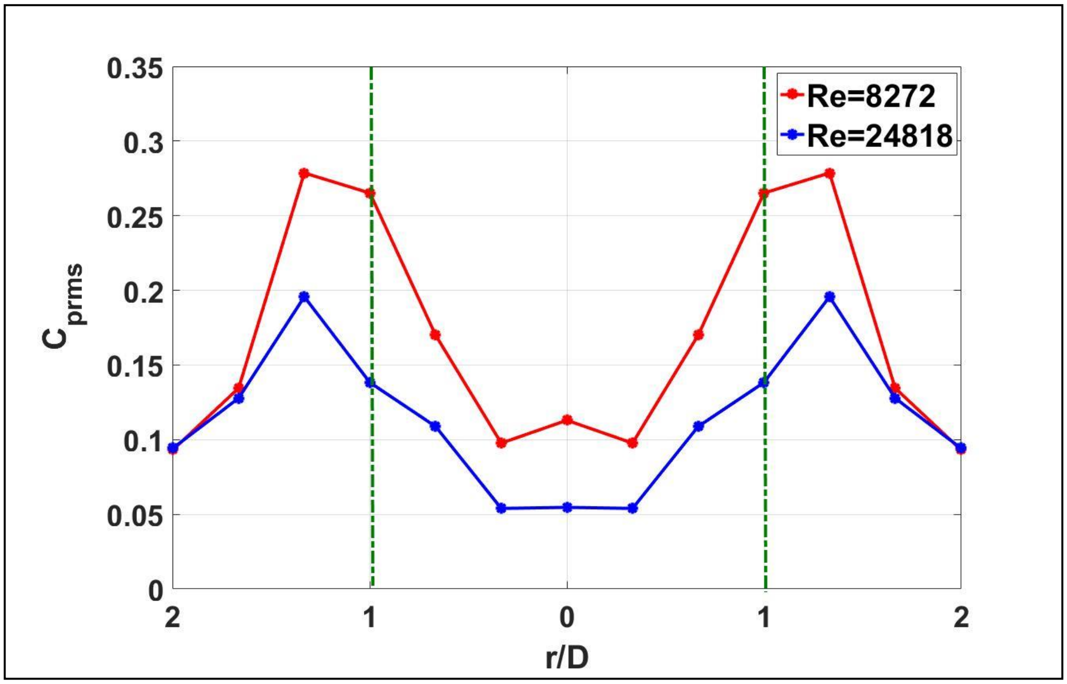

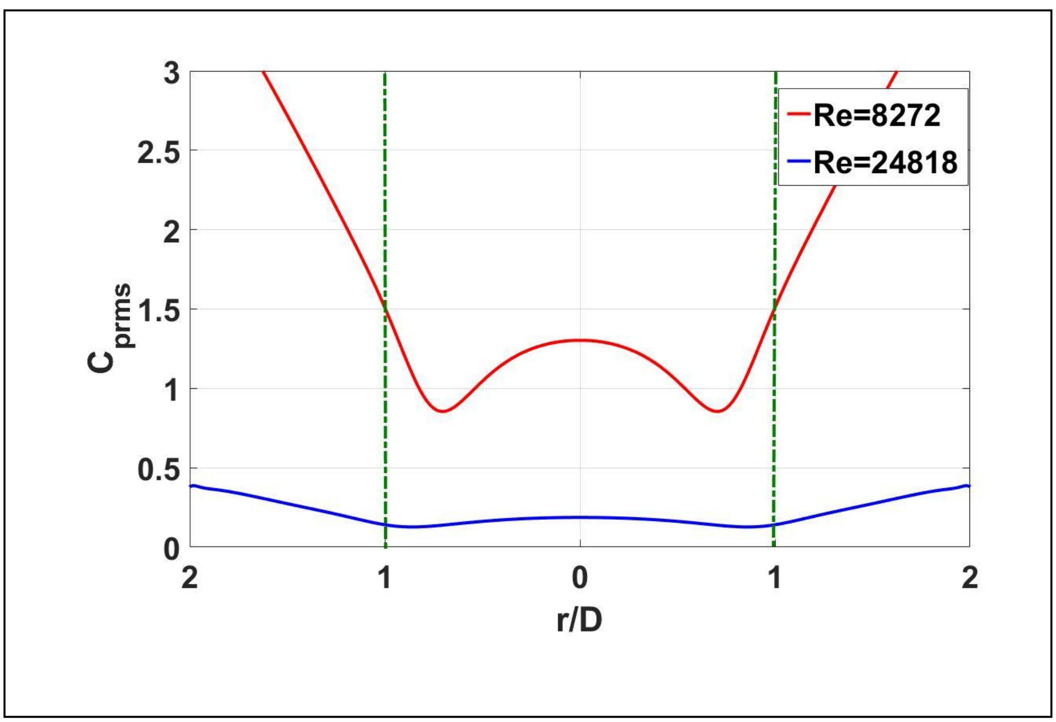

Figure 5.22 Comparison of the effect of varying Re_D on *RMS* wall-pressure fluctuation between the experimental (top) and the model (bottom) results at $H/D = 3$ (experiment) and $f \approx 245$ Hz (model). The broken green lines outline the end of the stagnation zone

CHAPTER 6: Conclusions and Recommendations

The present investigation is focused on studying the unsteady surface pressure fluctuation in jets impinging normally on a flat wall. The study is divided into two parts: the first part is concerned with developing a simple physics-based mathematical model of the impinging-jet wall pressure, and the second part involves measurements of the unsteady wall pressure in an existing impinging jet facility. The intent of developing the mathematical model is twofold:

(I) as a first step in a multi-step process of developing a high-fidelity, efficient model that may be used as a design tool for predicting wall-pressure fluctuation for problems involving flow-induced noise and vibration by impinging jets;

(II) to utilize the model for understanding the connection between the characteristics of the jet vortex structures and the surface pressure by varying the main jet and vortex parameters one at a time, and investigating the influence of this variation on the wall-pressure characteristics.

As the *first-step* in the development process, the present model is very simple, consisting of an array of potential, point-vortex rings that are advected under their own influence and that of their image vortices (due to the presence of the impingement wall), in addition to a steady advection field (emulating the mean-jet flow) consisting of potential stagnation point flow. This model flow field is coupled with the unsteady Bernoulli's equation to compute the wall pressure at each time instant as the vortex rings advect periodically towards the wall then radially outwards.

In comparison to the real jet, the present model does not account for several significant phenomena. These include the viscous core of real vortices, vortex pairing, vortex-boundary layer interaction, and the specific mean advection field of the jet flow. As such, the model is not expected to be useful, in quantitative or qualitative sense, in characterizing the pressure fluctuations outside the stagnation zone of the impinging jet, where vortex-wall interaction is known from literature to play a significant role in wall-pressure generation. However, the model results are expected to be qualitatively consistent with the characteristics of the wall-pressure fluctuation within the stagnation zone. Establishing this point, which is done here using experimental data from the second part of the investigation, would provide the necessary initial confidence to continue the development of the model in the future.

The model was utilized to examine the effects of changing the vortex-passing frequency, jet Reynolds number, and the vortex circulation on the fluctuating wall-pressure in the stagnation zone. The effect of varying the frequency effectively corresponded to varying the spacing between the jet exit and the impingement plate (H/D). Overall, the model results revealed that the stagnation zone pressure fluctuation are either low-level, sinusoidal-like and rather symmetric for $r/D < 0.5$, or energetic, featuring strong positive and negative peaks, with the negative peak being more prominent, for $r/D > 0.5$. The former fluctuations were attributed to "remote" vortex influences, and the latter to "local" effects. While the pressure fluctuation associated with remote influences remained fairly invariant with r/D, local effects increased with increasing r/D because of the increased proximity of the vortices to the wall as they convect radially outwards.

For $r/D < 0.5$, as the frequency increased (H/D decreased), p_{rms} was found to decrease due to the increasing "packing density" of vortices near the wall within the stagnation zone. The corresponding decrease in the inter-vortex spacing caused the induced flow along the stagnation streamline (which is parallel to the vortex array) by the individual vortices to overlap, reducing the vortex-to-vortex velocity and pressure fluctuation. An opposing frequency (H/D) trend was found on locally produced fluctuation ($r/D > 0.5$), where increased vortex packing/passage frequency resulted in increasing p_{rms}. This opposite effect was connected to the broadening of the induced velocity peaks on the wall underneath (which is normal, rather than parallel to the array) with the packing density of vortices.

When changing the vortex circulation (Γ) and the Reynolds number (Re_D), the overall radial distribution of p_{rms} remained qualitatively the same. The main influence of increasing these two parameters was to either increase (Γ) or decrease (Re_D) the strength of the pressure fluctuation relative to the dynamic pressure of the jet.

In the second (experimental) part of the investigation, the unsteady wall pressure was measured at two Reynolds numbers ($Re_D = 8272\ and\ 24818$; based on exit jet velocity (U_j) and the jet diameter (D)) for a jet at normal impingement incidence. The pressure was measured using an array of eight microphones over a radial domain range $r/D = 0\ to\ 2.33$ for three separation distances between the jet exit and the impingement wall: $H/D = 2{,}3, and\ 4$.

The results yielded radial distributions of p_{rms} that were consistent, both in their shape as well as their trends with H/D and Re_D, with the literature. Within the stagnation zone, several observations showed good qualitative agreement with the mathematical model results. These include, the wall-pressure time series features at $r/D < 0.5$ versus $r/D > 0.5$, and the trends in the p_{rms} distribution with both H/D and Re_D. On the other hand, it appeared that discrepancy in finer qualitative details between the experimental and the model results may be accounted for by including a vortex viscous-core in the model.

Analysis of the experimental data alone, using time series and power spectra, suggested that the basic wall-pressure generating mechanisms remain the same with increasing Reynolds number. However, the overall weakening of the level of pressure fluctuation with Reynolds number was *inferred* to be due to two reasons. First, the slower increase of the pressure source strength (square of vorticity/vortex circulation) with Re_D relative to that of the jet's dynamics pressure ($Re_D\ vs.\ Re_D^2$ respectively). Second, the weakening of the vortex-wall interaction effectiveness in generating pressure in the wall jet zone. This was hypothesized to be related to the jet vortices breaking up and becoming irregular/turbulent with increasing Reynolds number. This was implied from the appearance of small-scale random fluctuations in the pressure time series, and the irregularity of the negative pressure spikes at the higher Reynolds number (particularly at $H/D = 4$) .

Another interesting observation from the experimental data was the fact that the strong negative pressure spikes in the wall-jet zone did not weaken with increased H/D, notwithstanding that the overall pressure *RMS* level decreased with H/D. This was observed in both time series as well as in the wall-pressure probability density functions and skewness results. Since it is well understood in the literature that these spikes are produced during vortex-wall interaction, and given that the passage frequency of vortices decreases with H/D due to vortex pairing, it was concluded here that the decrease in *RMS* is due to the reduction in frequency of the spikes.

Overall, the results of the present investigation, in addition to providing some new insights into the connection between the unsteady wall pressure and the jet vortical structures, establishes an encouraging first step towards developing a physics-based model of impinging jets wall-pressure fluctuation. However, as a first step, the present model is very simple and it does not include phenomena that are known to be important for wall-pressure generation: vortex-vortex interaction, impingement-plate boundary layer, vortex-boundary layer interaction, viscous-core vortex model, and using Poisson's equation to calculate the wall pressure. These elements should be added in future development of the model. The present study suggests that, as far as the stagnation zone is concerned, the next two highest priority elements would be the inclusion of viscous-core vortices and the use of a more realistic advection field. Both of these items are expected to not only enhance the qualitative agreement with physical observations in the stagnation zone, but to possibly also lead to reasonable quantitative comparisons.

APPENDIX

Appendix: Uncertainty Calculation

1- Finding the uncertainty for the root mean square pressure (p_{rms})[(see 28)]

$$Variance = var(p_{rms}) * n = \frac{\overline{p^2}}{2}$$

$$var(p_{rms}) = \frac{\overline{p^2}}{2n}$$

$$standard\ deviation = \sigma = \sqrt{var(p_{rms})}$$

$$\sigma = \sqrt{\frac{\overline{p^2}}{2n}} = \frac{p_{rms}}{\sqrt{2n}}$$

Where σ represents the uncertainty and n represents the number of independent samples and was found assuming n to be equal to the number of vortices passing during the measurement period. Thus,

$$St_D = \frac{f * D}{U_j} = \frac{D}{T * U_j} \rightarrow T = \frac{D}{St_D * U_j}$$

Where T represents the time period between the passage of successive vortices, and

$$n = \frac{total\ data\ acquisition\ time}{time\ per\ cycle}$$

2- Finding the uncertainty for the third order moment (skewness), assuming Gaussian variation [(see 28)]

$$S = \frac{\overline{(p-P)^3}}{\sigma^3} = \frac{(\acute{p})^3/n}{\left(\sqrt{\frac{\sum(p-P)^2}{n}}\right)^3} = \frac{(\acute{p})^3/n}{\left(\sqrt{\frac{\sum(\acute{p})^2}{n}}\right)^3} = \frac{\overline{(\acute{p})^3}}{p_{rms}^3}$$

$$\frac{\partial S}{\partial \overline{(\acute{p})^3}} = \frac{1}{p_{rms}^3}$$

$$\frac{\partial S}{\partial p_{rms}^3} = -\frac{\overline{(\acute{p})^3}}{p_{rms}^6}$$

$$\Delta S = \left|\frac{\partial S}{\partial \overline{(\acute{p})^3}}\right| * \Delta\overline{(\acute{p})^3} + \left|\frac{\partial S}{\partial p_{rms}^3}\right| * \Delta p_{rms}^3$$

$$\Delta S = \frac{1}{p_{rms}^3} * \Delta\overline{(\acute{p})^3} + \frac{\overline{(\acute{p})^3}}{p_{rms}^6} * \Delta p_{rms}^3$$

$$\frac{\Delta S}{S} = \frac{\Delta\overline{(\acute{p})^3}}{p_{rms}^3} * \frac{p_{rms}^3}{\overline{(\acute{p})^3}} + \frac{\overline{(\acute{p})^3}}{p_{rms}^6} * \Delta p_{rms}^3 * \frac{p_{rms}^3}{\overline{(\acute{p})^3}}$$

$$\frac{\Delta S}{S} = \frac{\Delta\overline{(\acute{p})^3}}{(\acute{p})^3} + \frac{\Delta p_{rms}^3}{p_{rms}^3}$$

$$\Delta S = \left[\frac{\Delta\overline{(\acute{p})^3}}{(\acute{p})^3} + \frac{\Delta p_{rms}^3}{p_{rms}^3}\right] * S$$

More generally

$$\Delta S = \left[\left(\frac{\Delta\overline{(\acute{p})^3}}{(\acute{p})^3}\right)^2 + \left(\frac{\Delta p_{rms}^3}{p_{rms}^3}\right)^2\right]^{1/2} * S$$

Finding $\left(\frac{\Delta p_{rms}^3}{p_{rms}^3}\right)$ by assuming

$$F = p_{rms}^3 \rightarrow \Delta F = 3p_{rms}^2 * \Delta p_{rms}$$

$$\frac{\Delta F}{F} = \left(\frac{\Delta p_{rms}^3}{p_{rms}^3}\right) = \frac{3p_{rms}^2 * \Delta p_{rms}}{p_{rms}^3} = \frac{3\Delta p_{rms}}{p_{rms}}$$

$$\left(\frac{\Delta p_{rms}^3}{p_{rms}^3}\right) = \frac{3\Delta p_{rms}}{p_{rms}}$$

Where

$$\Delta p_{rms} = \sigma = \sqrt{\frac{\overline{p^2}}{2n}} = \frac{p_{rms}}{\sqrt{2n}} \rightarrow \left(\frac{\Delta p_{rms}^3}{p_{rms}^3}\right) = \left(\frac{p_{rms}}{\sqrt{2n}}\right) \Big/ p_{rms}$$

Finding $\left(\frac{\Delta\overline{(\acute{p})^3}}{(\acute{p})^3}\right)$ and assuming Gaussian variation

$$Variance = var\left(\overline{p^3}\right) * n = 6\left(\overline{p^2}\right)^3$$

$$p_{rms} = \sqrt{\overline{p^2}} \rightarrow p_{rms}^2 = \overline{p^2}$$

$$standard\ deviation = \sigma = \Delta\overline{(\acute{p})^3} = \sqrt{var(p_{rms})} = \sqrt{\frac{6(p_{rms}^2)^3}{n}} = \sqrt{\frac{6p_{rms}^6}{n}} = \sqrt{\frac{6}{n}}p_{rms}^3$$

$$\left(\frac{\Delta\overline{(\acute{p})^3}}{(\acute{p})^3}\right) = \left(\sqrt{\frac{6}{n}}p_{rms}^3\right) \Big/ (\acute{p})^3$$

$$\Delta S = \left[\left(\left(\sqrt{\frac{6}{n}}p_{rms}^3\right) \Big/ (\acute{p})^3\right)^2 + \left(\left(\frac{p_{rms}}{\sqrt{2n}}\right) \Big/ p_{rms}\right)^2\right]^{1/2} * \frac{\overline{(\acute{p})^3}}{p_{rms}^3}$$

3- Finding uncertainty for the fourth order moment (kurtosis), assuming Gaussian variation and following the same procedure for calculating the uncertainty of skewness [(see 28)]

$$K = \frac{(p-P)^4}{\sigma^4} = \frac{(\acute{p})^4/n}{\left(\sqrt{\frac{\sum(p-P)^2}{n}}\right)^4} = \frac{(\acute{p})^4/n}{\left(\sqrt{\frac{\sum(\acute{p})^2}{n}}\right)^4} = \frac{\overline{(\acute{p})^4}}{p_{rms}^4}$$

$$Variance = var\left(\overline{p^4}\right) * n = 96\left(\overline{p^2}\right)^4$$

$$\Delta\mathrm{K} = \left[\left(\left(\sqrt{\frac{96}{n}}\, p_{rms}^4\right)\Big/(\acute{p})^4\right)^2 + \left(\left(\frac{p_{rms}}{\sqrt{2n}}\right)\Big/p_{rms}\right)^2\right]^{1/2} * \frac{\overline{(\acute{p})^4}}{p_{rms}^4}$$

BIBLIOGRAPHY

BIBLIOGRAPHY

[1] Pai, S. I. (1954). Fluid dynamics of jets.

[2] Grant, A. J. (1974). A numerical model of instability in axisymmetric jets. *Journal of Fluid Mechanics*, *66*, 707-724.

[3] Popiel, C. O., & Trass, O. (1991). Visualization of a free and impinging round jet. *Experimental Thermal and Fluid Science*, *4*(3), 253-264.

[4] Zaman, K. B. M. Q., & Hussain, A. K. M. F. (1984). Natural large-scale structures in the axisymmetric mixing layer. *Journal of Fluid Mechanics, 138*, 325-351.

[5] Didden, N., & Ho, C. M. (1985). Unsteady separation in a boundary layer produced by an impinging jet. *Journal of Fluid Mechanics, 160*, 235-256.

[6] Landreth, C. C., & Adrian, R. J. (1990). Impingement of a low Reynolds number turbulent circular jet onto a flat plate at normal incidence. *Experiments in Fluids*, *9*(1-2), 74-84.

[7] AL-Aweni, M. O. (2013). simultaneous flow visualization and unsteady surface-pressure measurements in normally and obliquely impinging jets (Doctoral dissertation, MSU).

[8] Krishna, S. (2012). *Characterization of the flow-field in circular subsonic impinging jets Investigation of surface pressure fluctuations and far-field noise emissions through pressure sensor measurements* (Unpublished master's thesis). Delft University of Technology.

[9] Hall, J. W., & Ewing, D. (2005). The development of the large-scale structures in round impinging jets exiting long pipes at two Reynolds numbers. *Experiments in fluids*, *38*(1), 50-58.

[10] Hall, J. W., & Ewing, D. (2006). On the dynamics of the large-scale structures in round impinging jets. *Journal of Fluid Mechanics*, *555*, 439-458.

[11] El-Anwar, M., K. Zhang, A. Naguib, and A. Abouel-Fotouh. "Pressure fluctuation produced by a jet impacting on a wall at normal and oblique incidence." *ExHFT-7 7th World Conference on Experimental Heat Transfer, Fluid Mechanics, and Thermodynamics, 28 June - 03 July 2009, Krakow, Poland: proceedings*. Krakow: AGH U of Science and Technology Press, 2009. N. page. Print.

[12] Harvey, J. K., & Perry, F. J. (1971). Flow field produced by trailing vortices in the vicinity of the ground. AIAA journal, 9(8), 1659-1660.

[13] Naguib, A. M., & Koochesfahani, M. M. (2004). On wall-pressure sources associated with the unsteady separation in a vortex-ring/wall interaction. *Physics of Fluids*, *16*(7), 2613-2622.

[14] Bradshaw, P., & Koh, Y. M. (1981). A note on Poisson's equation for pressure in a turbulent flow. *The Physics of Fluids*, *24*(4), 777-777.

[15] Blake, W. K. (1986). Mechanics of flow-induced sound and vibration. Volume 1 General concepts and elementary source. Volume 2-Complex flow-structure interactions. Aplikace Matematiky, Applied Mathematics, 17.

[16] Monnier, B., Naguib, A. M., & Koochesfahani, M. M. (2015). Influence of structural flexibility on the wake vortex pattern of airfoils undergoing harmonic pitch oscillation. *Experiments in Fluids*, *56*(4), 80.

[17] Saffman, P. G. (1970). The velocity of viscous vortex rings. *Studies in Applied Mathematics*, *49*(4), 371-380.

[18] Walker, J. D. A., Smith, C. R., Cerra, A. W., & Doligalski, T. L. (1987). The impact of a vortex ring on a wall. *Journal of Fluid Mechanics*, *181*, 99-140.

[19] White, F. M. (2017). *Fluid mechanics*. New Delhi, India: McGraw-Hill Education.

[20] Naguib, A. M., Jiang, W., & Zhang, K. (2012). Source advection effects on unsteady-surface-pressure asymmetry in oblique impinging jets. *AIAA journal*, *50*(7), 1634-1638.

[21] Milne-Thomson, L. M. (1996). *Theoretical hydrodynamics*. Courier Corporation.

[22] Koochesfahani, M., & Dimotakis, P. E. (1985). Laser-induced fluorescence measurements of mixed fluid concentrationin a liquid plane shear layer. *AIAA journal*, *23*(11), 1700-1707.

[23] Crow, S. C., & Champagne, F. H. (1971). Orderly structure in jet turbulence. *Journal of Fluid Mechanics*, *48*(3), 547-591.

[24] Kinsler, L. E., Frey, A. R., Coppens, A. B., & Sanders, J. V. (1999). Fundamentals of acoustics. *Fundamentals of Acoustics, 4th Edition, by Lawrence E. Kinsler, Austin R. Frey, Alan B. Coppens, James V. Sanders, pp. 560. ISBN 0-471-84789-5. Wiley-VCH, December 1999.*, 560.

[25] Liepmann, D., & Gharib, M. (1992). The role of streamwise vorticity in the near-field entrainment of round jets. *Journal of Fluid Mechanics*, *245*, 643-668.

[26] Jung, D., Gamard, S., & George, W. K. (2004). Downstream evolution of the most energetic modes in a turbulent axisymmetric jet at high Reynolds number. Part 1. The near-field region. *Journal of Fluid Mechanics*, *514*, 173-204.

[27] Cooper, D., Jackson, D. C., Launder, B. E., & Liao, G. X. (1993). Impinging jet studies for turbulence model assessment—I. Flow-field experiments. *International Journal of Heat and Mass Transfer*, *36*(10), 2675-2684.

[28] Benedict, L. H., & Gould, R. D. (1996). Towards better uncertainty estimates for turbulence statistics. Experiments in fluids, 22(2), 129-136.